Model-Based Probabilistic Inversion Using Magnetic Data: A Case Study on the Kevitsa Deposit

Master of Science in Applied Geophysics

Nilgün Güdük

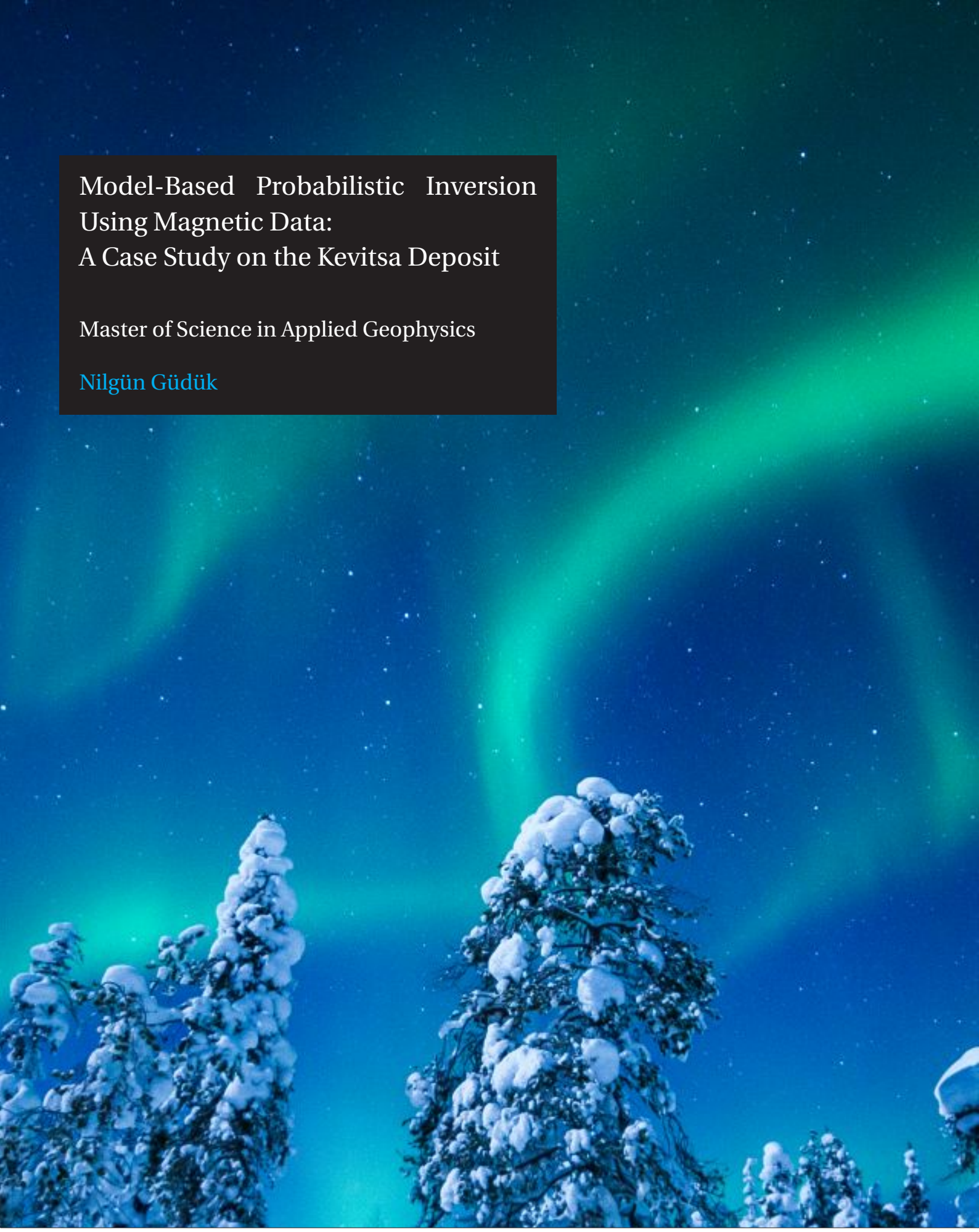

IDEA League

BOLIDEN

Model-Based Probabilistic Inversion Using Magnetic Data: A Case Study on the Kevitsa Deposit

Master of Science in Applied Geophysics

by

Nilgün Güdük

IDEA LEAGUE
JOINT MASTER'S IN APPLIED GEOPHYSICS

Delft University of Technology, The Netherlands
ETH Zürich, Switzerland
RWTH Aachen, Germany

To be defended publicly on March 2, 2020 at 10:00

Student:	Nilgün Güdük	
Thesis committee:	Prof.dr. Florian Wellmann	RWTH Aachen, committee chairman
	Dr.ir. Deyan Draganov	Delft University of Technology, committee member
	Miguel De La Varga, M.Sc	RWTH Aachen, daily supervisor
	Janne Kaukolinna	Boliden, daily supervisor

IDEA League

ABSTRACT

Considering the inherent uncertainty of structural geological models, the non-uniqueness of geophysical inverse problems, and the growing availability of data, there is a need for methods that combine different types of data and allow for updating knowledge in a consistent way. By making use of the development of efficient, gradient-based MCMC algorithms, probabilistic inversion provides a tool for this. To test to what extent we can reduce the uncertainty of an initial geological model, we integrate geological modelling into a Bayesian inverse framework. Additional information can then be included in this inverse framework through likelihood functions.

The proposed methodology is tested on a geological model of the structurally complex Kevitsa deposit in Finnish Lapland. By starting with an initial interpretation-based 3D geological model, we define the uncertainties in our geological model by means of probability density functions. Magnetic data and geological interpretations of borehole data are used to define geophysical and geological likelihoods respectively. To use the magnetic data in the inference, the mathematical description of the magnetic forward calculation is implemented for a 3D voxelised space, linking the geophysical data through magnetic rock properties to the uncertain structural parameters. The result of the inverse problem is presented in the form of probability distributions and ensembles of the realised models through visual analysis. The former is a statistical consideration of the results, whereas the latter is a visual representation for direct interpretation in a geological sense. The uncertainties in these visual representations are best presented by means of information entropy, which allows for a quantitative analysis. The results show that well-defined likelihood functions can reduce uncertainties in geological models and build on the complementary strength of different types of data. Where probabilistic inversion inherently provides uncertainty analysis, finding a single representative solution is less trivial. Therefore we conclude that the strength of the used methodology mainly lies in data integration and uncertainty quantification.

ACKNOWLEDGEMENTS

Hereby I would like to thank everyone that contributed to this project. My gratitude goes out to Florian Wellmann, who responded with immediate enthusiasm toward setting up this project and has supervised me throughout my thesis. I would also like to thank Tobias Hermansson, who agreed to the joint project and made me feel welcome in Boliden.

I thank all those in the CGRE department that helped me with a variety of aspects throughout the past months, with a special thanks to Miguel De La Varga for tirelessly explaining the almost philosophical concepts of probabilistic inversion, Rhea von Bülow for her tips, reviews, and overall guidance, and Elisa Heim, for her permanent support

Thank you to everyone in Boliden that helped me develop on a broad scale of fronts, from surviving subarctic winters to learning about hard rock geological settings and exploration geophysics. Of course, a special thanks goes out to Janne Kaukolinna for sharing his expert knowledge and always finding an answer to my questions.

Nilgün Güdük

Aachen, February 2020

Contents

List of Figures

1

INTRODUCTION

Two scientific breakthroughs resulted in a useful tool that formed the foundation of the methods used in this thesis. The first was Isaac Newton's Universal Law of Gravitation (Newton, 1687), followed by Marquis de Laplace's finding that gravitational attraction obeys a differential equation that we now know by his name. These two events have formed the basis of potential theory. Potential theory describes a large group of phenomena, among which magnetic fields and Bayesian interpretation of probability, both of which will be addressed in this project.

In geophysical applications, the aim is to understand processes and find properties within media that cannot be accessed through direct observation. Therefore, indirect methods are used to infer these unknown properties. Inverse theory provides the mathematical background and the practical methods needed to solve such problems. The solution to the inverse problem exists by linking the unknown properties to data through physical or mathematical relations. However, solely data-driven inversions are likely to result in geologically unrealistic results. In such an approach, the subsurface is divided into grid cells with assigned physical properties. These cell boundaries bear no relation to geological contacts or structures, but rather are artifacts of the grid. To avoid geologically unrealistic outcomes, geophysical inversion can be naturally constrained by surface-based modelling, where a rock property is assigned to a surface. This results in an inversion that integrates rock property as well as subsurface geometry. Going a step further, the model can be improved by integrating different types of data into the inference. Data integration is often not straightforward, yet becomes increasingly relevant as the acquisition of geophysical data is getting cheaper and faster, and often large amounts of different types of data are available for interpretation. This urges for the development of methods that objectively integrate geophysical data sets and geologic knowledge in one single framework in a consistent manner.

A Bayesian framework provides a solution for this. A Bayesian approach is a probabilistic construction that allows new information to be combined with existing information, hence updating our knowledge. All information is expressed in probabilities, representing a state of information. New information on any type of data can be incorporated into the inversion through the use of likelihood functions. Likelihood functions provide a quantification of the likelihood that the observed data would be observed given the current model. Bayesian inference inherently provides an uncertainty quantification as the solution of the inverse problem is an ensemble of models

that all fit the data to a certain degree.

This probabilistic approach to geophysical inversion is fundamentally different from commonly used deterministic approaches. Deterministic inversion provides a "best fit" of the data, i.e. the optimised solution. Yet, finding a global optimum for a complex problem is not so trivial and a model that minimises the data misfit does not necessarily reflect the true subsurface conditions. Geophysical data is often noisy and incomplete, putting an unwanted constraint on obtaining the quantities of interest. Additional constraints on the solution are due to the inability of deterministic methods to solve non-linear problems and hence, regularisation is required. Probabilistic inversion can be applied to both linear and non-linear problems and relies on Markov chain Monte Carlo (MCMC) algorithms to approximate the solution numerically. In complex problems, this process can become computationally costly. Fortunately, it is an active field of research and recent developments of gradient-based algorithms (Betancourt et al., 2014; Homan and Gelman, 2014) provide solutions for efficient computation.

Hence, within the current development, probabilistic inversion in a Bayesian framework is deemed to provide a consistent and objective way of data integration, while providing a quantitative analysis of the result. Though Bayesian methods are embraced in different scientific communities, it remains relatively unexplored in Earth sciences. Previous studies by de la Varga and Wellmann (2016) and Wellmann et al. (2018) have tested its application in structural geological modelling, by considering it as an inference problem. Wellmann et al. (2018) applied the methodology to a mineral exploration setting and used geophysical likelihood based on gravity data as well as geological likelihoods. In this project, we perform a similar study by using magnetic data as geophysical likelihood. The difference is mainly in the initial geological model, which in this study is completely based on geological interpretations. The question remains to what extent uncertainties in such a conceptual model can be reduced by additional data through likelihood functions.

We will evaluate this research objective by a case study on the Kevitsa deposit in Finnish Lapland. This Ni-Cu-PGE deposit, located in a highly deformed geological setting in the Central Lapland greenstone belt, has a large economic significance with a proven 160 million tons of Nickel. This has led to the acquisition of extensive geophysical and geological data sets spanning several decennia. However, the geometry of the intrusive body is still not well recovered. This makes it an excellent showcase for our methodology. We start with a completely geology-based, interpretive initial model, unbiased by geophysical data. Such a model, of course, contains large uncertainties, and we will aim to reduce these through probabilistic inversion using magnetic and geological data. The reason for using magnetics is twofold. Firstly, magnetics is a commonly used method in mineral exploration, and testing the validity of the approach can provide relevant insights for practical implementations. Secondly, though useful due to the cost and time efficiency, the magnetic method suffers from non-uniqueness, meaning a wide distribution of equivalent sources can produce the same result (Hinze et al., 2013; Telford et al., 1990). Hence, the results of the magnetic method have inherent ambiguities of interpretation and should be considered with a probabilistic approach.

The objective of this study is to investigate to what extent we can reduce the uncertainty in a preliminary geological model in a Bayesian inverse framework using magnetic data combined with geological knowledge.

In the following chapters, we will try to answer this question. We start with the geological setting of our case study, the Kevitsa intrusion, in Chapter 2. Chapter 3 covers the underlying theory of the magnetic method and inverse theory. Chapter 4 explains the methodology of the research and covers the processing of the data, the geological model building, the implementation of the forward magnetic simulations and the probabilistic model building. Additionally, it includes a synthetic test to validate the proposed methodology in a simple case. Having presented all the required data and tools, the results are presented in Chapter 5. These findings are discussed in Chapter 6, and lastly, the conclusions and recommendations are presented in Chapter 7.

2

GEOLOGICAL SETTING

The Kevitsa deposit is a Nickel (Ni), Copper (Cu) and Platinum-group elements (PGE) mineralisation containing deposit located approximately 140 kilometers North of the Arctic circle in the Municipality of Sodankylä, Finnish Lapland. After being discovered in 1987 by the Geological Survey of Finland, extensive exploration campaigns followed. The first comprehensive study of the Kevitsa intrusion was published by Mutanen (1997). Since then, numerous studies have been focussing on different aspects of Kevitsa, ranging from mineralisation, chemistry and origin of the ore, to geometry assessment of the deposit. Used methods were geochemical modelling (Le Vaillant et al., 2017), geometry assessment of the intrusion using seismics (Koivisto et al., 2015), and remanent magnetisation assessment (Montonen, 2012). In this chapter, the findings that are particularly interesting for this project will be summarised.

2.1. REGIONAL GEOLOGY

The Kevitsa igneous complex is located within the Central Lapland greenstone belt (CLGB). The Paleoproterozoic CLGB in Northern Finland is one of the largest greenstone belts in the Precambrian Fennoscandian Shield, covering roughly 400 kilometers from the Russian border in the East to Sweden and Norway in the North-West (Luolavirta et al., 2018). The CLGB consists of several volcano-sedimentary stratigraphic groups with ultramafic intrusives (Gregory and Lappalainen, 2016). These stratigraphic groups in the CLGB have undergone multiple episodes of folding and thrusting, resulting in structural repetition of the stratigraphic sequences (Gregory and Lappalainen, 2016). In general, the evolutionary history of the CLGB started approximately 2.5 Gya by rifting of the Archean basement, followed by eruption of komatiitic and rhyolitic volcanic rocks and the development of large mafic layered intrusions. After this magmatism, a period of sedimentation followed, after which felsic to ultramafic volcanism occurred with emplacement of intrusive bodies dating from 2.2 to 2.05 Gya. This extensional stage ended with compressional tectonics like collisions and over-thrusting. The supracrustal evolution of the CLGB was then completed with deposition of clastic sediments into basins (Hanski et al., 2001). A more detailed description of the regional geology is provided by Hölttä et al. (2007).

2.2. KEVITSA INTRUSION

The Kevitsa Ni-Cu-PGE deposit is the centre of the layered intrusive body comprising ultramafic to mafic igneous rocks dated to 2058 ± 4 Mya (Mutanen, 1997). The known economic mineralisation predominantly occurs as disseminated Cu and Ni sulphides (Gregory and Lappalainen, 2016).The ore body consists of several irregular zones cut by faults and shear zones locally offsetting the mineralisation (Gregory and Lappalainen, 2016). The ore body is hosted in the centre of the main ultramafic unit of the Kevitsa layered intrusion. This unit consists of olivine pyroxenite and its derivatives (olivine websterite, olivine wehrlite and metaperidotite) grouped as ultramafic pyroxenite (UPX), and has an arcuate shape at the surface with a Southwest dip. Figure 2.1 shows the geological map of the intrusion. At the Southwest surface boundary, the lower part of the UPX unit is overlain by gabbroic rocks (IGB), thinning towards the flanks of the body at the current erosional level. The thickest drill core intersection of the gabbroic rocks gives a thickness of circa 800 meters. The grouped IGB unit includes magnetite gabbro, which may contain fairly abundant equant magnetite Mutanen (1997). The distribution of the different gabbroic rock types and hence the internal structure of the gabbroic zone is not well understood. A dunite body (UDU), in literature referred to as "central dunite", crops out in the central part of the intrusion. However, it is expected that the central dunite is not to be spatially associated with the ore deposit.

Koivisto et al. (2015) analysed the 2D and 3D seismic data that had been acquired over the intrusion. The study concluded that the base of the Kevitsa intrusion is clear in the Northern and Western parts of the intrusion, with continuous reflections originating from the contact to the intrusion. Towards the East, in the vicinity of the Satovaara Fault Zone, interpretation becomes more ambiguous. The NNE-SSW trending Satovaara fault has deformed the Eastern margin of the Kevitsa intrusion and within the deposit there are smaller scale structures in similar trend (Kokko, 2018). The base of the intrusion is mostly defined by disruption of reflections internal to the intrusion. Towards the South, prominent reflections in seismic line E5 suggested a deeper continuation of the Kevitsa main intrusion toward the South–Southwest as shown in Figure 2.2. These findings have been confirmed by borehole data, suggesting the ultramafic UPX unit extends to over 1.5 kilometers in depth. At this depth the shape becomes increasingly complex. The complex geometry at depth reflects both regional tectonic deformation events as well as the original magmatic emplacement relationships (Luolavirta et al., 2018). The intrusion was emplaced into a volcano-sedimentary sequence belonging to the Savukoski Group, characterised by mica schists and black shales overlain by komatiitic (UKO) and picritic volcanic rocks (Luolavirta et al., 2018).

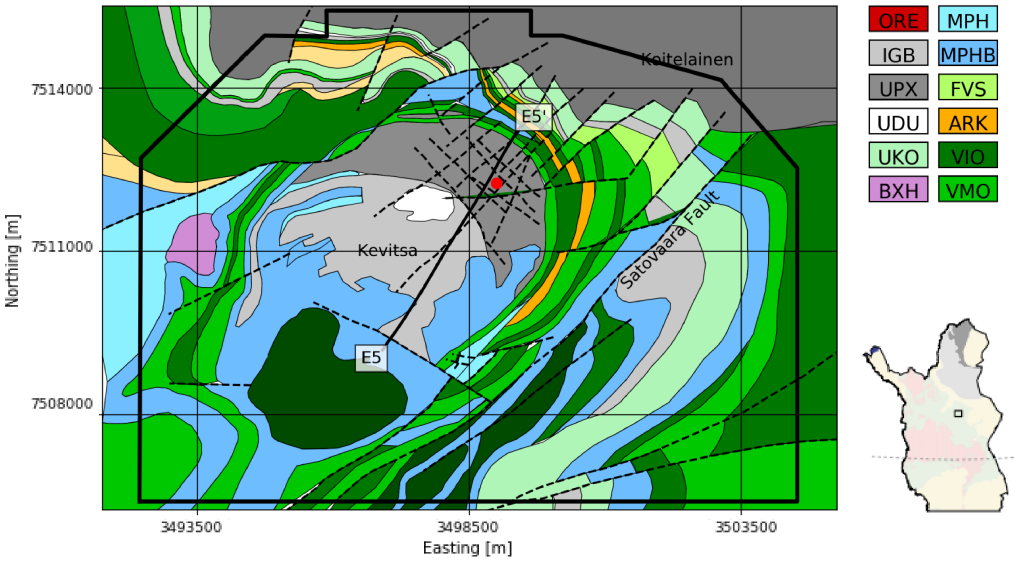

Figure 2.1: Geological surface map of the Kevitsa intrusive complex with the described intrusion units UPX, IGB, and UDU. The country rocks comprise a mostly layered sequence of intermediate and felsic volcanic rocks (VIO), mafic volcanic rocks (VMO), phyllites (MPH) and carboneceaous phyllites(MPHB), overlain by komatiite (UKO). Within this layered sequence, discontinuous layers of arkose (ARK) and felsic volcanics (FVS) are interbedded. In the West, there is a hydrothermal breccia (BXH). The black frame corresponds to the airborne magnetic survey shape. The right bottom map shows the location of Kevitsa in Finland, where the light green colour represents the CLGB. (After Fournier (2019))

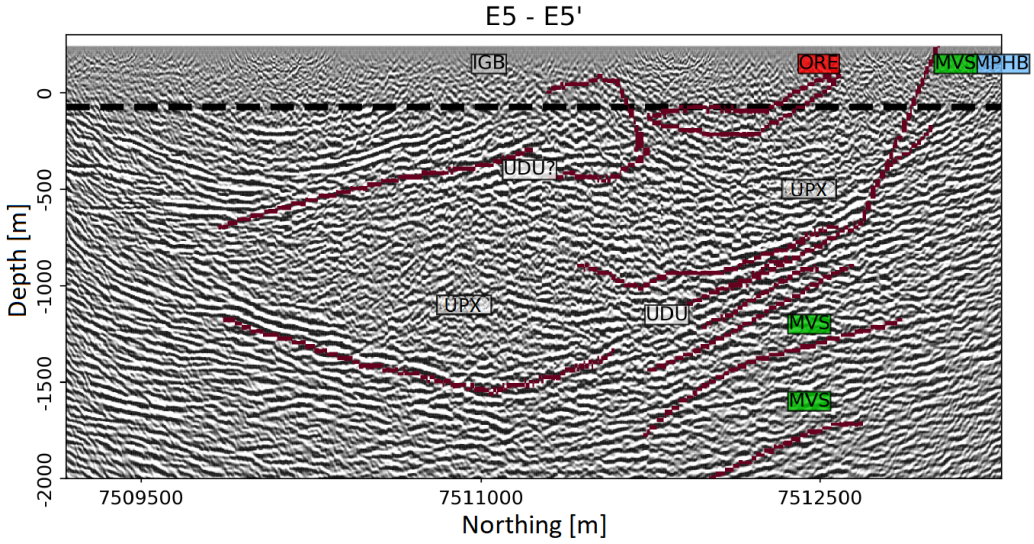

Figure 2.2: Seismic section from line E5 (location is shown on Figure 2.1), with interpretations from Koivisto et al. (2015) included in the section by Fournier (2019). MVS is defined as mafic volcanics and comprises VMI and VIO. (After Fournier (2019))

Lithological and compositional variations in drill cores from different parts of the Kevitsa intrusion show differences, which possibly could reflect different magmatic histories for the ore domain and the surrounding intrusion. The ore-bearing domain is characterized by lithological variability with fluctuations in rock and mineral compositions and presence of numerous ultramafic inclusions. This is interpreted by Luolavirta et al. (2018) to reflect dynamic magma emplacement conditions. Drill core profiles around the ore domain, in contrast, show compositional homo-

geneity. Any observed evolutionary trends are smooth and predictable, suggesting a less vigorous emplacement history (Luolavirta et al., 2018). To explain these observations, Luolavirta et al. (2018) suggested the following multi-stage magmatic model for the origin of the Kevitsa intrusion:

Stage 1: Early intrusion of picritic magma forming the Central Dunite.
Stage 2: Emplacement of basaltic magma as a steady continuous flow into the Kevitsa magma chamber and crystallisation of compositionally uniform olivine-clinopyroxene cumulates followed by differentiation in at least nearly closed system.
Stage 3: Multiple vigorous magma emplacements into the hot interior of the Kevitsa intrusion forming the ore-bearing domain of the intrusion.

3

THEORETICAL FRAMEWORK

This Chapter covers the theory of the methods that are used in this study. The first part of the this Chapter is dedicated to the magnetic method. The underlying theory as well as its application in exploration geophysics will be discussed. The second part of this Chapter is dedicated to probabilistic programming, where inverse theory and methods for inference will be discussed.

3.1. MAGNETIC METHOD

The magnetic method is the oldest geophysical method. Additionally, it is also the most versatile one of the geophysical methods (Telford et al., 1990; Hinze et al., 2013). Magnetic surveys are relatively cheap and easy compared to other measurements and processing is practically not needed (Telford et al., 1990). Although the magnetic method has a lot in common with gravity methods, magnetics is generally more complex. Where the gravity field is monopolar and always in the vertical direction, the magnetic field is dipolar and has variable directions. The magnetic field is time-dependent and shows externally derived variations on different timescales ranging from fractions of seconds, caused by micropulsations, to several days, caused by magnetic storms. Magnitude generally increases with the period of the fluctuation (Hinze et al., 2013). These variations are called diurnal variations and for most exploration purposes their effect must be monitored and removed from the measured signal. Additionally, like all potential field methods, the magnetic method suffers from a lack of uniqueness in its interpretation (Telford et al., 1990; Hinze et al., 2013).

3.1.1. GOVERNING EQUATIONS

The Maxwell equations describe electromagnetic phenomena. The following two are the governing equations for magnetism:

$$\nabla \cdot \vec{B} = 0, \tag{3.1a}$$

$$\nabla \times \vec{B} = \mu \vec{j^e} + \mu\varepsilon \frac{\partial E}{\partial t}. \tag{3.1b}$$

Equation 3.1a states that the field lines of the magnetic induction $\vec{B}$ always form closed loops, implying that magnetic monopoles do not excist (Blakely, 1995; Lowrie, 2007). Since any diver-

genceless field can be expressed in terms of the curl of another field, the magnetic field always has a magnetic vector potential. Equation 3.1b describes that electric current, with electric current density $\vec{J}^e$, gives rise to a magnetic field and temporal variations in the electric field $\vec{E}$ contribute to this. Here, ε and μ are medium parameters, being the electric permittivity and magnetic permeability respectively. By assuming that currents are absent at the location of observation and the dielectric properties of the medium can be ignored, a valid approximation in most geophysical applications, Equation 3.1b reduces to

$$\nabla \times \vec{B} = 0, \tag{3.2}$$

meaning field $\vec{B}$ is irrotational. Irrotational fields can be expressed in terms of a scalar potential, hence the magnetic field can be described as the gradient of scalar potential φ

$$\vec{B} = -\nabla\varphi, \tag{3.3}$$

where the negative sign is due to convention as adapted from Kellogg (1953) meaning that particles of the same sign repel each other, and the potential equals the work done by the particle against the field (Blakely, 1995). In contrast to the magnetic field, the scalar potential is independent of direction. This allows for simplifications in mathematical operations, as will be seen in Section 4.2.3.

3.1.2. MAGNETIC QUANTITIES

Before discussing the magnetic quantities, it is worth noting that in magnetic prospecting two different unit systems, the CGS and SI systems, are commonly used and some confusion might arise around the conversions and the related quantities. For this study different literature has been used, where different unit systems are applied. Here the SI units will be applied.

A volume of a magnetic medium can be considered as a collection of magnetic dipole moments from elementary particles. In the absence of an external magnetic field the dipole moments may or may not be aligned in a certain direction, depending on the medium and its magnetic history. However, in the presence of an external field $\vec{B}_0$, like the geomagnetic field, it will exhibit to at least some extent alignment in the direction of the external field due to induction (Telford et al., 1990). This alignment creates magnetisation currents in the medium, and the medium is said to be magnetised. A secondary field $\vec{B}_s$, separate from $\vec{B}_0$, but caused by $\vec{B}_0$, is generated and the total field is given by

$$\vec{B} = \vec{B}_0 + \vec{B}_s. \tag{3.4}$$

If $\vec{B}_s$ is much smaller than $\vec{B}_0$, and in the absence of remanent magnetisation, $\vec{B}_s$ and $\vec{B}_0$ are approximated to be in the same direction within the body (Telford et al., 1990). The dipole moment of an elementary atom is represented by $\vec{m}$. The magnetic dipole moment per unit volume is given by the magnetisation vector $\vec{M}$, quantified in Amperes per meter [A/m]:

$$\vec{M} = \frac{1}{V}\sum_i \vec{m}_i. \tag{3.5}$$

In literature the magnetic field is generally expressed by either $\vec{H}$, the magnetic field intensity in [A/m], or by $\vec{B}$, the magnetic induction in [nT]. Where $\vec{M}$ is related to the magnetic field intensity $\vec{H}$, there is a magnetic polarisation vector $\vec{J}$ in [nT] that, in a similar way, is related to the magnetic

induction $\vec{B}$ (Hinze et al., 2013). The magnetic polarisation vector $\vec{J}$, often called magnetisation too, is linearly related to $\vec{M}$ by the magnetic permeability in vacuum $\mu_0 = 4\pi 10^{-7}$:

$$\vec{J} = \mu_0 \vec{M}. \tag{3.6}$$

The quantity measured with magnetic surveys is the magnetic induction $\vec{B}$, hence it is more convenient to continue with representations in $\vec{J}$, from now on called magnetisation, and $\vec{B}$ where possible. $\vec{J}$ is a sum of two vectors:

$$\vec{J} = \vec{J}_i + \vec{J}_r. \tag{3.7}$$

$\vec{J}_i$ is the magnetisation that is caused by induction due to an external field. This magnetisation is due to the reorientation of internal dipoles in order to align their spins along the current external field. $\vec{J}_r$ is the remanent (or residual) magnetisation vector. Although remanent magnetisation may have different causes (e.g. thermal, chemical, depositional) it is always related to the magnetic history of the material and the retainment of those effects after the magnetic field vanishes (Hinze et al., 2013). Remanent magnetisation can be absent, but if present can have a substantial effect on $\vec{J}$. Within the body, the field produced by $\vec{J}$ is added to the magnetic induction $\vec{B}$.
The magnetic induction $\vec{B}$ represents the total field, including the magnetisation effects. In the general case where $\vec{B}$ and $\vec{J}$ are in the same direction the relation between $\vec{B}$ and $\vec{H}$ is given by:

$$\vec{B} = \mu_0 \vec{H} + \vec{J}. \tag{3.8}$$

Field $\vec{H}$ can be understood as the quantity that describes how $\vec{B}$ is modified by the magnetisation of the material in magnetic materials (Lowrie, 2007). The fundamental difference between both fields is that, where field lines of $\vec{B}$ always form closed loops (Equation 3.1a), field lines of $\vec{H}$ are discontinuous at surfaces where the magnetisation changes (Lowrie, 2007). In the absence of remanent magnetisation, $\vec{J} = \vec{J}_i$ and Equation 3.8 reduces to:

$$\begin{aligned} \vec{B} &= \mu_0(1+k)\vec{H} \\ &= \mu \vec{H}, \end{aligned} \tag{3.9}$$

where the magnetic permeability of a medium $\mu = \mu_0(1+k)$ in [H/m] is a measure of the ease with which the magnetic field is passed through the material (Hinze et al., 2013). By empirical studies, the relation between the magnetisation vector and magnetic field has been found as a function depending on the magnetic field strength and the history of the magnetic material (Kaufman et al., 2008). For low magnetic fields, however, this can be approximated by a linear relationship (Telford et al., 1990):

$$\vec{J} \approx k\vec{B} + \vec{J}_r, \tag{3.10}$$

where k is the magnetic susceptibility, the fundamental rock property in magnetic prospecting. This dimensionless parameter indicates the ease with which a material can be magnetised in the current magnetic field (Hinze et al., 2013). It can be seen from Equation 3.7 and 3.10 that the inductive magnetisation is then approximated by (Hinze et al., 2013):

$$\vec{J}_i = k\vec{B}. \tag{3.11}$$

3.1.3. MAGNETIC MEDIA

There is a wide range of magnetic susceptibility values that result in different behavior in the presence of an external magnetic field. Based on this behavior, materials can be categorised in four main groups: diagmagnetic, paramagnetic, ferromagnetic and ferrimagnetic.
Diagmagnetic materials are characterised by a negative susceptibility value. Paramagnetic materials have a positive but small susceptibility value, with typically $0 < k < 10^{-6}$ (Hinze et al., 2013). The majority of the minerals that make up rocks are diamagnetic or paramagnetic, and show weak responses to a magnetic field (Hinze et al., 2013).
Ferromagnetic materials on the other hand are characterised by positive and large susceptibilities with $1 < k < 10^{6}$ (Hinze et al., 2013). Due to their strong magnetic interaction, these materials show internal alignment of the magnetic moments within large regions, called domains. Iron, cobalt and nickel are examples of ferromagnetic materials. Ferromagnetic materials are characterized by their Curie temperature. Above this critical temperature, the particles can no longer align due to their high energy state, resulting in loss of magnetic properties. Decreasing the temperature below the Curie point restores the ferromagnetic properties again. The dipoles then align according to the external magnetic field. In case of no movement of the magnetic material or the external geomagnetic field, the ferromagnetic minerals will be still aligned to the external field. But as they keep the orientation of passed geomagnetic fields, they can be used to date samples and deduce processes which happened at the subsurface (Hinze et al., 2013).
The domains in some materials are again divided in subdomains. These subdomains can align in opposite direction, without resulting in zero net moment. These materials are labelled as ferrimagnetic. Practically all magnetic minerals are ferrimagnetic and although paramagnetism and ferromagnetism contribute to magnetism in rocks, the susceptibility of rocks is predominantly defined by the presence of ferrimagnetic minerals like magnetite and pyrrhotite (Langel and Hinze, 1998; Hinze et al., 2013). Ferrimagnetic materials are also able to sustain magnetisation after the external magnetic field vanishes, and thus show remanent magnetisation (Hinze et al., 2013). Due to the positive temperature gradient with depth, below a certain depth threshold called the Curie isotherm depth (≈ 40 km) all materials reach their Curie temperature and the lithosphere becomes virtually nonmagnetic (Langel and Hinze, 1998; Telford et al., 1990). Hence, local anomalies are always caused by features in the upper crust.

3.1.4. EARTH'S MAGNETIC FIELD

Evidence regarding the origin of the geomagnetic field strongly support that the main field is caused by convective currents associated with conducting materials in the liquid outer core of the Earth (Telford et al., 1990; Hinze et al., 2013). This field resembles that of a dipole and is unstable causing it to reverse polarity in regular intervals. A small field associated with the ionised layers of the upper atmosphere contributes to the main field (Telford et al., 1990). Unlike the main field, this field shows rapid variations referred to as diurnal variations, with periods ranging from seconds to several days or more (Telford et al., 1990; Hinze et al., 2013). These effects have to be monitored during surveys and afterwards removed from the signal. There are also spatial variations to be taken into consideration. On average the geomagnetic field has a magnitude of approximately 50,000 nT, but it varies from roughly 25,000 nT at the magnetic equator to about 70,0000 nT at the magnetic poles. These latitude variation are ~ 4 nT/km and should be corrected for on high-latitude, large scale projects.

Since the magnetic field is a vector field, it is characterized by both direction and magnitude. The magnetic field represented in Cartesian coordinates is given by $\vec{B} = \vec{B_x} + \vec{B_y} + \vec{B_z}$. The magnetic elements as illustrated in Figure 3.1 show the components of field $\vec{B}$. Since the Earth's magnetic North does not coincide with the geographic North and the field is not on the horizontal plane, declination D (the angle of the magnetic North with the geographic North) and inclination I (the dip of the field from the horizontal) are needed to define field $\vec{B}$.

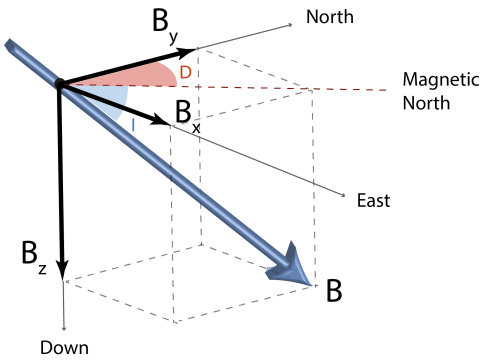

Figure 3.1: Earth's magnetic field and it's components in Cartesian coordinates. The x-component $\vec{B_x}$ is along the geographic North, which deviates an angle D (declination) from the magnetic North of the Earth. $\vec{B}$ dips an angle I (inclination) from the horizontal.

The magnetic method is a passive exploration method as it measures the natural magnetic field of the Earth and the anomalous changes in the field due to local subsurface conditions (Hinze et al., 2013). In exploration often an unoriented magnetometer is used to measure the scalar magnitude, or total field intensity of the total flux $\vec{B_T}$ (Hinze et al., 2013):

$$\vec{B_T} = \sqrt{\vec{B_0}^2 + \vec{B_s}^2}. \tag{3.12}$$

Generally it is assumed that $\vec{B_0}$ and $\vec{B_s}$ are co-linear, which is valid as long as the magnetic anomaly does not perturb the magnetic field in any other direction than the principle direction. This assumption breaks down for anomaly amplitudes of approximately 10,000 nT and larger, since at these high susceptibilities the magnetisation direction can become dependent on the shape of the body and have a significantly different direction than the inducting field (Lelièvre and Oldenburg, 2006). In this work it will be assumed that the assumption holds and the linear approach is valid.

3.2. INVERSE PROBLEM

Where direct observations of media properties and subsurface processes of interest are not possible, indirect methods have to be used to infer them. The mathematical background and methods to solve such inference problems are provided by inverse theory. This section will be dedicated to the mathematical background of inverse theory, followed by the used methods to solve the inverse problem.

3.2.1. INVERSE THEORY

Inversion is a tool to estimate certain parameters governing a physical process based on measurements of the outcome of this process. The procedure consists of three main steps (Tarantola, 2005):

1. *Parameterisation of the system*: Develop a set of model parameters that completely describe the system under study.
2. *Forward modelling*: Using physical laws that, given the model parameters, allow us to make prediction on the measurement results of the observable parameters.
3. *Inverse modelling*: Using measured values of the observable parameters to infer the actual values of the model parameters.

Where forward modelling gives an unique solution based on the specific choice of model parameters, inverse modelling will result in multiple solutions that describe the observed data equally well. There are two approaches to solve an inverse problem: a deterministic approach and a probabilistic one. Deterministic inversion provides one possible solution of the inverse problem, generally given by the maximum likelihood point as solution of the least-squares problem. Probabilistic inversion provides an ensemble of plausible models that describe the observed data. Unlike in deterministic inversion, computing the solution to the probabilistic inverse problem does not require any regularisation. Furthermore, in probabilistic inversion there are no constraints on the nature of the forward problem: it is allowed to be highly non-linear and non-differentiable.

Despite these fundamental differences, both inference approaches rely on observations, i.e. measurements of some observable parameters. Using the observed data, collected in a finite-dimensional vector that spans the data space, we want to infer unknown physical model parameters where the set of all model parameters spans the model space. The number of model parameters needed to describe a system can in reality be infinite, e.g. when we are interested in a property that depends on the position inside a volume (Tarantola, 2005). In practical cases a finite number of model parameters is considered in a discretised model space, though it is important to remember that discretision of a continuous model space always adds some subjectivity (Fichtner, 2018).

Linking the model space and data space is done through forward modelling based on a physical theory. Assuming some model parameters, like a geological model and known susceptibility values, and using some control parameters, the forward modelling operator can produce synthetic or predicted data. Often in geophysical problems, the governing physics cannot be given explicitly but is in the form of a differential equation that has to be solved numerically (Tarantola, 2005; Fichtner, 2018).

Inverse modelling is then described as estimating model parameters using observation. Often more than one model explains the data equally well, thus, the inverse problem is said to be non-

unique. Non-uniqueness can have several origins. For this project there is an inherent or physical non-uniqueness coming from potential-field measurements where different anomaly shapes at different depths give the exact same signal. Hence, assessing the whole set of plausible models should be preferred over inverting for a single model.

3.2.2. BAYESIAN INFERENCE FOR PARAMETER ESTIMATION

The fundamental idea of probabilistic inverse theory is to express all components of the inverse problem in terms of probability density functions (p.d.f.) (Fichtner, 2018). If $p(\theta \in M)$ is the probability that model parameter θ is inside subvolume M of model space $\mathbb{M}$, then the Radon-Nikodym theorem states that this probability can always be expressed in terms of a probability density p, expressing degrees of believe (Tarantola, 2005):

$$p(\theta \in M) = \int_{M \in \mathbb{M}} p(\theta) d\theta. \tag{3.13}$$

Bayesian inference, named after Bayes (1763), provides a method to update our prior knowledge represented by $p(\theta)$ about given parameters θ that describe a model by including observed data y. This parameter estimation is formulated by Bayes' theorem for probability densities:

$$p(\theta|y) = \frac{p(y|\theta)p(\theta)}{p(y)}. \tag{3.14}$$

The aim of Bayesian inference is to obtain the posterior probability distribution $p(\theta|y)$. This expresses how probable our model parameters θ are, given the observed data y. To quantify this, we use the prior $p(\theta)$, which is independent from any observations, and constrain this by means of a likelihood functions $p(y|\theta)$: the probability or likelihood to simulate the observations y through model $\mathscr{M}$, given parameters θ. $p(y)$ is the evidence or marginal likelihood and acts as a normalisation factor. It contains the probability of the observed data independently from any parameter value. The prior and the likelihood can be expressed easily as they are assumed to be part of the model. The evidence, however, needs to be computed by the following integral:

$$p(y) = \int_{\theta} p(y|\theta)p(\theta) d\theta. \tag{3.15}$$

Virtually all practical problems contain multiple unknown parameter and quickly become higher dimensional problems (Gelman et al., 2013). In these cases, the evaluation of Equation 3.15 becomes intractable. When we do not compute the evidence, Bayes' theorem can be written as a proportionality:

$$p(\theta|y) \propto p(y|\theta)p(\theta). \tag{3.16}$$

Approximation techniques can then be used to estimate the posterior distribution. The Markov chain Monte Carlo (MCMC), among other methods, provides a solution to this problem.

3.2.3. MARKOV CHAIN MONTE CARLO

When setting up a Bayesian inference problem with N unknowns, we implicitly create an N-dimensional model space $\mathbb{M}$ for the prior distribution to exist in (Davidson-Pilon, 2015). On top of this space sits a parameter space, represented by a surface or curve, that reflects the prior distribution on the unknown parameters (Davidson-Pilon, 2015). Adding observed data does not change the parameter space, but does affect the shape of the prior distribution surface in order to reflect

where the true parameters are likely located. In two dimensions these changes result in a landscape with "mountains and valleys". Essentially, the data push up the original surface to a peak that reflects the posterior probability where the true parameters likely live. The global maximum (hence highest peak) then represents the most likely model. This "pushing up" by the observed data is hampered by the prior probability distribution, where an area of lower prior probability is more resistant and forms valleys. Hence, the weights that are put on the values by the posterior are dependent on the weight that the prior put there. If the prior has assigned a probability of 0, no posterior probability will be assigned (Davidson-Pilon, 2015).

Monte Carlo methods use random sampling to estimate statistical properties of a given process. To find the posterior distribution of the model space, the sampling process should not affect the distribution. MCMC aims to search the model space, while preserving the target distribution (Betancourt, 2018). A Markov chain is a sequence of points in the model space generated by a proposal probability distribution, the Markov transition density. The acceptance or rejection of the proposal depends on the likelihoods of the current and proposed states. Sampling from the proposal distribution results in a new state in the Markov chain. The progression of the Markov chain is shown in Figure 3.2. Following this algorithm, it can be seen that the development of the Markov chain is at most determined by the current state, but never on the predecessor states (Sambridge and Mosegaard, 2002).

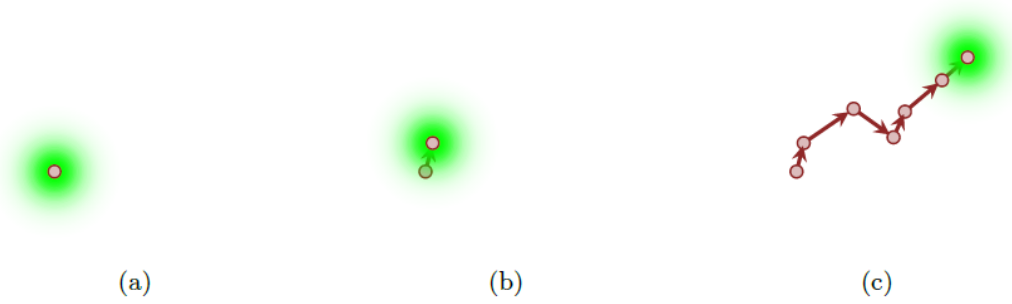

Figure 3.2: A graphic representation of the progression of a Markov chain. (a) A point in the model space with a Markov transition density (in green) that determines proposals to a new state. (b) Sampling results in a new state with a new Markov transition density. (c) Repeating these steps results in a sequence of points that meander through the model space. (Betancourt, 2018)

Monte Carlo methods were developed to numerically approximate integrals that are not tractable analytically but for which evaluation of the function being integrated is tractable (Metropolis and Ulam, 1949). MCMC can be used in Bayesian inference in order to generate samples from the unnormalised part of the posterior instead of dealing with intractable computation involved in normalising. Hence, MCMC returns samples from the posterior distribution defined up to its normalisation factor, not the posterior distribution itself. By going through a large number of samples, the hope is to reconstruct the posterior "mountain top" from our two-dimensional example. As the number of unknowns in the model grows and by searching in large-dimensional spaces, the problem becomes more complex. This phenomenon was introduced by Bellman (1957) as the curse of dimensionality. Large-dimensional spaces tend to be mostly empty and regions with relatively high probability occupy small volumes.

After a large number of iterations, all accepted positions are returned as samples or traces, the target distribution. The chain is considered to have reached steady state. The period before this

is called the burn-in period and during inference, the sampled points from this period should be discarded as they are unrelated to the final distribution. Mathematically, by performing a large number of iterations, the algorithm would give results independent of its initial position. In practice starting with poorly chosen starting values can slow down or prevent any convergence (Davidson-Pilon, 2015; Betancourt, 2018). Ideally we would like to start the chain at or close to the peak of our landscape, where the posterior distribution is thought to exist. This peak is the maximum a posterior (MAP), mathematically the most likely value for the unknowns.

3.2.4. SAMPLING METHOD

HAMILTONIAN MONTE CARLO

With increasing complexity of the models, simple random-walk sampling methods become inefficient due to their random exploration of the large, high-dimensional model space. In high-dimensional models the posterior distribution only comprises a thin, donut-shaped surface. In these cases, considering the geometry of probability distributions provides a solution. By considering both the density and the volume of the posterior distribution, expectation values can be found by accumulating the integrand over model space. The neighborhood immediately around the mode consists of models that fit the proposed conditions best, thus contains high densities. In high-dimensional problems, however, there is little volume in this high-density region since there is a little number of models that fit all conditions. Away from the mode, in the tails of the distribution, there are low densities that cover large volumes. Consequently, the large volume between these two extremes can have a strong contribution to the posterior distribution despite the lower densities here (Betancourt, 2018). With increasing dimensions of the model space, the tension between high-density low-volume and low-density high-volume regions grows and the only significant contribution to any expectation comes from a neighbourhood called the typical set (Betancourt, 2018). The typical set is a concept from information theory and refers to the region encapsulating most of the volume of the posterior model space. In order to make accurate estimates of our parameters, we have to be able to identify the location of the typical set within the model space. This allows to focus computational resources towards where they are most effective.

When model parameters are continuous, Hamiltonian Monte Carlo (HMC) provides a solution for this. HMC abolishes random walk behavior and sensitivity to correlated input parameters by applying analogies from Hamiltonian dynamics to the problem of sampling (Neal, 2012). It takes advantages of the geometry of the typical set, by taking a series of steps informed by first-order gradient information of the input parameters (Homan and Gelman, 2014). The Markov chain, as mentioned before, preserves the target distribution, and thus is directed and confined to the typical set no matter where in the model space it is applied (Betancourt, 2018). In analogy to Hamiltonian dynamics, a scalar Hamiltonian function $H(q,p)$ is introduced. The Hamiltonian is a measure of energy, with q being the position variable, corresponding to the unknown model parameter θ that is being sampled, and p the new auxiliary variable representing momentum. The momentum variable gives an additional degree of freedom to calculate the trajectories that explore the model space. Both q and p typically have independent Gaussian distributions, and together form the phase space. Thus, by adding a momentum variable to all initial model variables we double our space and go from a N-dimensional model space to a $2N$-dimensional phase space.

Positional vector q is distributed with a probability density function $p(q)$, which represents the target distribution. The distribution for the momentum p given parameter q is given by $p(p|q)$. The probabilistic system can then be expanded to find the joint probability distribution in phase

space:

$$p(q,p) = p(p|q)p(q). \tag{3.17}$$

This expanded system defines the Hamiltonian scalar function $H(q,p)$, which itself can be decomposed into kinetic and potential energy:

$$\begin{aligned} H(q,p) &= -\log p(p|q) - \log p(q) \\ &= K(p,q) + V(q). \end{aligned} \tag{3.18}$$

The potential energy $V(q)$ is completely determined by the posterior distribution whereas the kinetic energy $K(p,q)$ controls the momenta p and hence can be chosen freely. Because the Hamiltonian encapsulates geometry, any choice of K can generate a vector field oriented with the typical set. This can be done using the Hamilton's Equations (Betancourt, 2018):

$$\begin{aligned} \frac{dq}{dt} &= \frac{\partial H}{\partial p} = \frac{\partial K}{\partial p} \\ \frac{dp}{dt} &= -\frac{\partial H}{\partial q} = -\frac{\partial K}{\partial q} - \frac{\partial V}{\partial q}. \end{aligned} \tag{3.19}$$

It can be seen here that gradient $\frac{\partial V}{\partial q}$ affects the introduced momenta, but not directly the initial parameters themselves. Using this gradient information, HMC creates trajectories by updating for the momentum p. Each trajectory contains a pre-defined number of leapfrog steps, with a defined step size. The algorithm for these trajectories can be summarised in the following steps:

- Sampling from the conditional distribution $p(p|q)$ in order to lift the starting point in model space to phase space.
- Generating trajectories in the phase space by following the Hamiltonian vector field for a defined step size ϵ and number of leapfrog steps L (or updates). The integration time is then a function of the number of steps given by $L\epsilon$.
- Projecting the trajectories back down onto the model space, where the target distribution is.

At the end of each trajectory, the proposed state is accepted based on the probability:

$$min[1, exp(-H(q*,p*) + H(q,p))], \tag{3.20}$$

where the proposed state is $(q*,p*)$ and the current state is (q,p). HMC thus alternates trajectories generated using gradient information, with random walk updates. New states proposed in this way can be distant from the current state but nevertheless have a high probability of acceptance.

Figure 3.3: Graphical representation of how HMC and NUTS explore. (a) Random walks in parameter space (red) are combined with Hamiltonian trajectories in phase space (blue). Once the typical set (a thin surface with fuzzy boundaries) is reached, the Hamiltonian trajectory follows the gradient and stays close to the typical set. The trajectory ends when a new random state is proposed (not represented here). (b) Once the chain converges to the typical set, exploration is continued by taking samples (red) throughout the surface. (After Betancourt (2018))

NO-U-TURN SAMPLER

The Hamiltonian Monte Carlo algorithm has three parameters that must be set by the user: the step size ϵ, the desired number of leapfrog steps L and the mass matrix Σ (Homan and Gelman, 2014). The performance of the algorithm in terms of sampling efficiency is highly sensitive to these tuning parameters, since every choice results in a different Markov transition (Betancourt, 2018). A small ϵ allows to stay in the desired trajectory, but can waste computation time if the steps are too small. A too large ϵ will result in low acceptance rates as too many proposals will be rejected. If L is chosen too small, the algorithm will show inefficient random walk behavior while a too large L again wastes computation time as the algorithm will do too much work on each iteration. Lastly, if Σ is poorly suited to the covariance of the posterior, ϵ will have to be decreased to maintain precision while at the same time L is increased to maintain computation time in order to ensure statistical efficiency. To this purpose, the No-U-Turn Sampler (NUTS) is an extension to HMC that requires no hand-tuning (Homan and Gelman, 2014). NUTS selects an appropriate number of leapfrog steps by optimising ϵ to match the acceptance-rate target, estimates Σ during the tuning phase, where warm-up sample iterations are run and adapts L dynamically while sampling.

NUTS generates a proposal by starting at an initial position determined by the drawn parameters of the last iteration. It then creates an independent standard normal random momentum vector and evolves the initial system both forwards and backwards in time to form a balanced binary tree. At each iteration, the tree is then increased by one level, doubling the number of leapfrog steps. This process is terminated by either satisfying the NUTS criterion for a new subtree, or the depth of the tree hits the maximum depth. Then, rather than using a standard Metropolis step, the next parameter values are selected via multinomial sampling with a bias towards the latter half of the taken steps in the trajectory (Betancourt, 2018).

For a precise definition of the NUTS algorithm and a proof of detailed balance, see Homan and Gelman (2014). NUTS' value as sampling method is widely acknowledged, proven from its default use for continuous variables in different probabilistic programming tools like Stan and PyMC.

4

METHODS AND MATERIALS

In this chapter, we present the available materials and the proposed methodolody that led up to the results. First the used field data is presented, followed by the methodology to solve the forward and inverse problem.

4.1. FIELD DATA

Since the discovery of the Kevitsa deposit in 1987, extensive exploration campaigns followed, leading to a large collection of data sets. In this project, we focus on magnetic and petrophysical borehole data. In this section, the provided data and the processing steps will be discussed.

4.1.1. MAGNETIC DATA

Both airborne and ground magnetic data are available from the study site. Airborne data is preferred in this case, as it contains less effects from temporal variations and near-surface geologic sources (Hinze et al., 2013). Mainly the latter feature is of importance, due to the lithological and compositional variations between the ore domain and the surrounding intrusion as mentioned in section 2.2. Since the interest is about the main intrusion scale, these smaller scale variations in measured values within the UPX are considered irrelevant. Hence, for this purpose ground magnetic data contains too many details which cannot be resolved by the airborne data.

The used dataset was acquired in July 2009 with a scalar magnetometer with a sensitivity of 0.02 nT. The flight path as recorded by the acquisition program in WGS 84 latitude/longitude has been converted into the Finland uniform coordinate system (KKJ) lateron. The dataset as received was already corrected for diurnal variations by using magnetic values recorded by the ground base station. The correction was done by subtracting the observed magnetic base-station deviations. The data had also been micro-levelled in order to remove persistent low-amplitude components of flight-line noise. Lastly, the recorded survey altitude had been corrected for the acquisition configuration since the cable on which the magnetometer had been attached had had an angle with the vertical. The total magnetic field as received is shown in Figure 4.1. To obtain this image, the data is interpolated on a regularly spaced grid. This is done using a curvature-minimizing interpolation algorithm, as the potential field is considered to be smooth (Smith and Wessel, 1990).

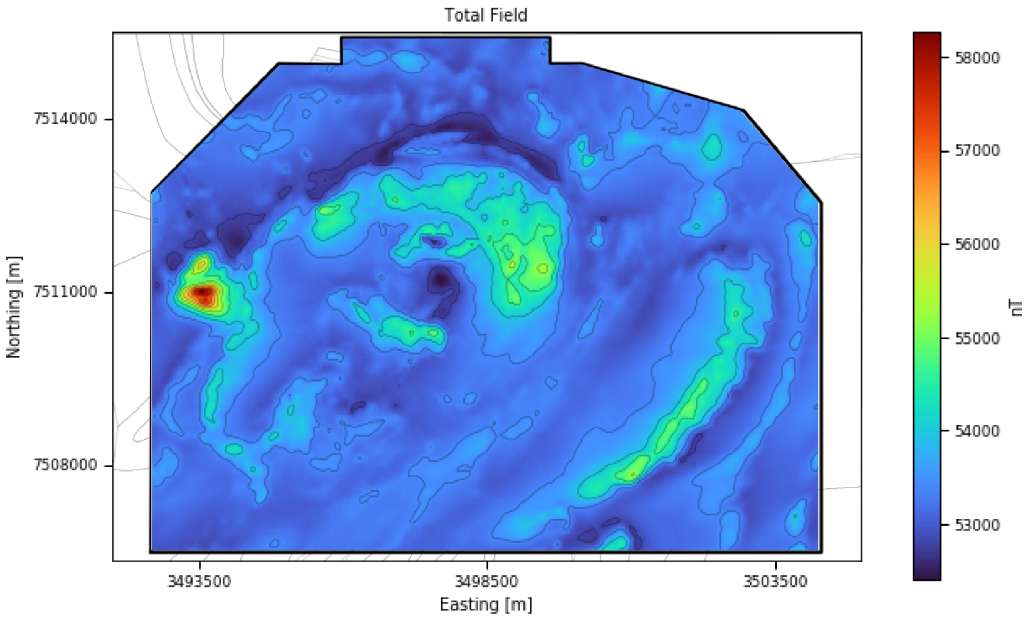

Figure 4.1: The provided airborne magnetic data.

By relating Figure 4.1 to the geological map shown in Figure 2.1, five main observation can be made:

1. A strong magnetic anomaly is visible over the main intrusion (UPX).
2. Directly North of the intrusion, much lower values are measured.
3. Responses similar to that of the Kevitsa main intrusion are observed from the elongated Saatovaara intrusion East of Kevitsa.
4. Strong magnetic responses are observed from the hydrothermal BXH unit in the West.
5. A strong magnetic anomaly is located at the center of the central dunite (UDU).

From points 1 and 2, it can be estimated that the Northern margin of the UPX unit has a shallow dip. Since the UPX unit gives a strong positive anomaly, and the geomagnetic declination in this region is known to be directing North, hence the inducing field too, the shallow dip results in a strong dipolar effect of the field caused by the intrusion. This results in a negative signal to the North of the intrusion. The Saatovaara intrusion and the BXH unit are both deemed to be too far away from the UPX intrusion to have a significant effect on the magnetic response measured over the UPX intrusion. Since the focus of the modelling will be on the UPX intrusion, these observations can thus be disregarded. The central dunite, however, is close to the intrusive body and has to be considered. Point 5 is explained by a study on cores sampled from this zone by Montonen (2012). He reported large Keonigsberger ratios, indicating strong remanent magnetisation with a direction that opposes the induced magnetisation. This kind of remanent magnetisation is expected to have formed during a reversed polarity period of the geomagnetic field. Montonen (2012) found the average inclination of remanent magnetisation to be -42.4 degrees; however, the declination remains unknown, since none of the analysed samples were directional.

Additionally, borehole data is used in this project. The available data comprises 899 boreholes

with a number of 187 different geological codes for the lithological interpretation. In section 2.2, the grouping of differently defined rocks into one unit was already briefly touched upon. For analysis of the borehole data, the grouping defined by Fournier (2019) is used. Additionally, 84 of these boreholes have downhole susceptibility measurements.

PROCESSING OF AIRBORNE MAGNETIC DATA

Before the airborne magnetic data could be used in the inversion, several processing steps had to be performed. First, the regional field had to be correctly estimated and removed from the total-field measurements, in order to obtain the anomalous field produced by the target sources. Interpretation and numerical modelling are carried out on the anomalous-field data, and reliability of the results depends partly on the success of the regional-field removal (Li and Oldenburg, 1998). Different methods exists for this, as reviewed extensively by Hinze (2012). After visual analysis of different profiles, a general regional trend could not be found throughout the survey area. Hence, a DC offset is removed from the measured data by selecting a zone where the anomalous field was expected to be zero based on geologic knowledge (Figure 4.2).

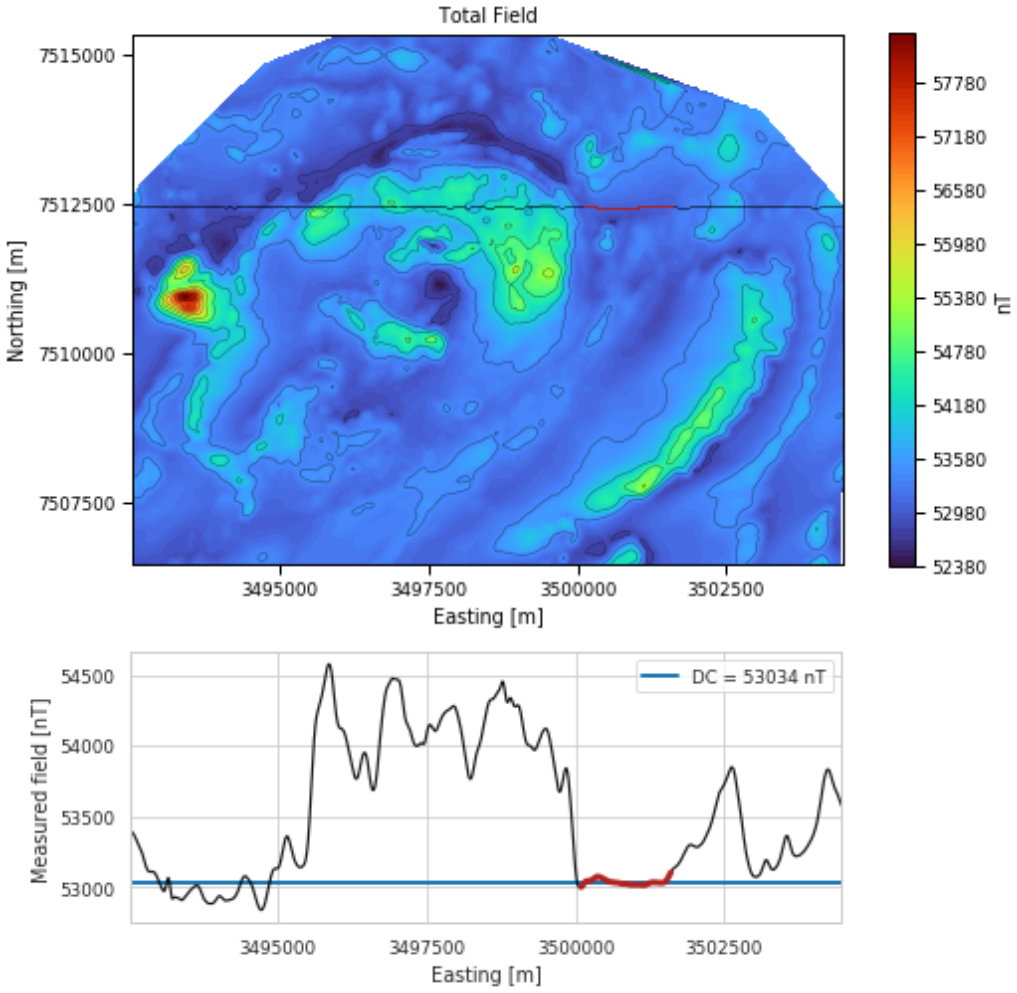

Figure 4.2: The profile corresponds to the drawn profile on the magnetic data map. The selected section, represented in red is expected to have zero magneitc response. Hence, the average value from this section is taken as DC offset in order to remove the regional field.

After obtaining the anomalous field, the data required filtering in order to obtain a smoother field over the intrusive body that shows less variation within the body itself. This is achieved by upward continuing the field data. Upward continuation transforms the potential field measured on one surface to the field that would be measured on a surface at a larger distance from the source. This transformation attenuates anomalies with respect to wavelength (Blakely, 1995): the shorter the wavelength, the greater the attenuation. Shorter wavelengths (high frequencies) oscillate many times over a given extent and hence reflect shallow, near-surface magnetic field variations. Long-wavelength components (low frequencies) oscillate only a few times over the same extent and catch deeper laying, more profound sources. These deeper laying sources can be emphasised by attenuating shorter wavelengths from the data. Upward continuation is a linear relationship in the Fourier domain, where the upward-continued data h_{uc} can be obtained by (Blakely, 1995):

$$\mathscr{F}(h_{uc}) = \mathscr{F}(h)e^{-\Delta z|k|}. \tag{4.1}$$

Here, F denotes the Fourier transform, h is the original data, $|k|$ is the wavenumber modulus and Δz is the increased elevation from the measurement level to the level we want to extrapolate the data to. Equation 4.1 is a real function. The absence of an imaginary or phase component means that no phase changes are imposed on the upward-continued field (Blakely, 1995).

To use the discrete Fourier transform, a rectangular grid with regular spacing is required. Therefore, the irregular shape of the survey had to be first reshaped into a rectangular form with the grid dimensions being a power of two - a condition imposed by simple Fast Fourier Transform (FFT) algorithms. Then, in order to minimize edge effects, the grid had to be extended. The edges on each side are padded with edge values from the original grid, in order to produce a smooth transition. The data is then transformed to Fourier domain, used Equation 4.1 to find $\mathscr{F}(h_{uc})$. By applying an inverse Fourier transform and removing the added grid points from the output file, the upward continued data is obtained. The implementation of this transformation can be found in appendix B. The results of the processing step are shown in Figure 4.3.

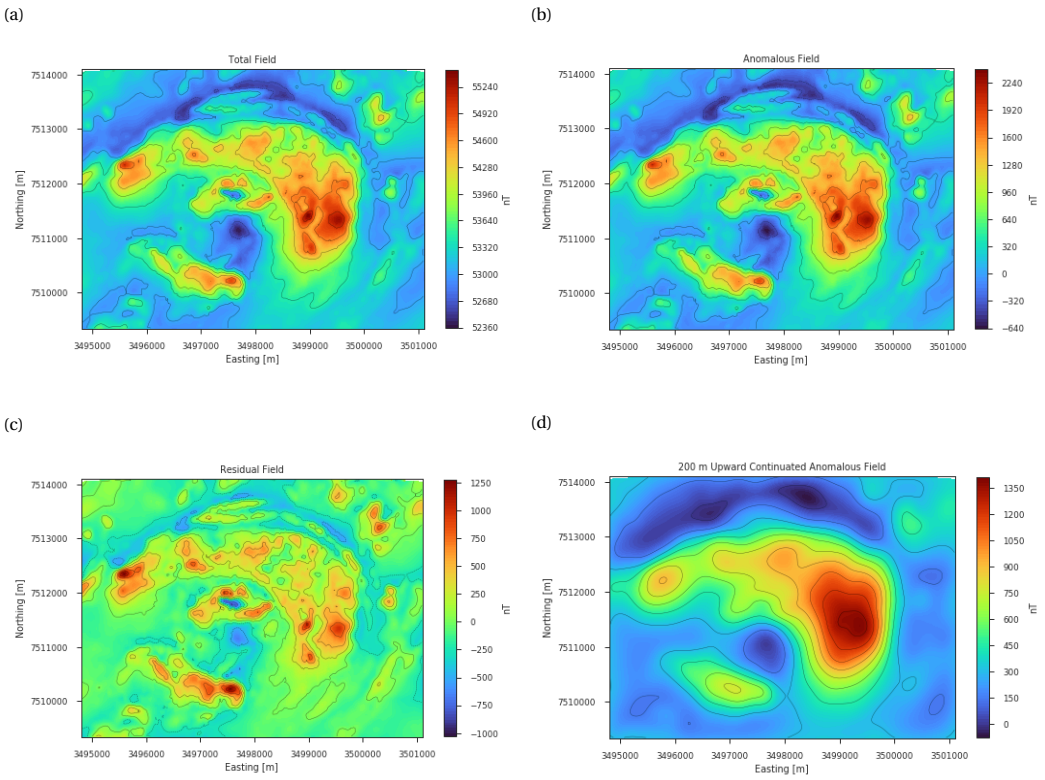

Figure 4.3: Processing results of the obtained airborne magnetic field data. (a) The provided data, cropped to the intrusion scale. (b) The obtained anomalous field after removing the regional field. (c) Data that is removed by upward continuation. (d) The smoothed data that will be used in further steps.

4.2. FORWARD MODELLING

The inversion is founded on the solution of the forward problem, which in our case is a simulation of the magnetic response of the initial subsurface model. Prior to the forward calculation, the initial geological model needs to be set up. After this, the forward calculation simulates the magnetic field this geology would produce: the forward magnetics.

4.2.1. IMPLICIT GEOLOGIC MODELLING TOOL: GEMPY

GemPy (de la Varga et al., 2019) is an open-source 3-dimensional geological modelling tool implemented in the programming language Python. It is based on an implicit potential-field interpolation approach developed by Lajaunie et al. (1997), making use of a CoKriging interpolation. The 3-dimensional continuous space in x, y, z is characterized by a dimensionless scalar field. Isosurfaces of this scalar field connect the interface points and hence represents synchronously deposition of the layer. The gradient of the scalar field is directed perpendicular to the isovalue surfaces, following the change in physical properties through the subsurface. By interpolating the whole space globally instead of each lithological unit independently, geological continuity is ensured as the location of one unit affects the location of the others in the same depositional environment (de la Varga et al., 2019). Another advantage of the global interpolator is the availability of the interpolated data between the layers of interest for further analysis. GemPy is a surface-based interpolator, meaning that all the added input data has to refer to a surface. The surfaces always mark the bottom of a unit.

GemPy accommodates an automatic modelling step in order to incorporation geological modelling in a Bayesian inference framework. The architecture is built on top of Python library Theano, which provides automatic differentation (AD) (de la Varga et al., 2019). AD allows for numerical evaluation of the derivative of a function - a necessity for algorithms that rely on gradient information. Transitions between different formations, and thus their assigned (petrophysical) properties, are modelled as sharp transitions. In order to guarantee continuity of the gradient, these transitions are smoothed out slightly. By providing non-zero gradients, geological modelling can be integrated into a Bayesian inverse framework by linking it to a probabilistic programming tool. The inversion requires calls to the forward model. Different gridding options are incorporated in GemPy, to reduce the load of these forward calculations. Relevant for this project, are the custom grid that allows for computation of the geological model at specific point in space, and the centered grid, which will be discussed in greater detail in Section 4.2.3. GemPy already included built-in functionality to compute forward gravity fields conserving the AD of the package. In this project, a similar functionality is provided to compute the forward magnetic field. The process of this implementation is described in Section 4.2.2.

4.2.2. GEOLOGICAL MODELLING

A 3-dimensional geological model represents a simplified version of the true geology, designed to give a visual summary of the geometry and distribution of major geological elements. In order to fit the scope of this project, we simplify the geological model to the intrusion scale. We aim to represent the geology by modelling the overburden, the main intrusive body and the host rock. The reasons for this choice are twofold: Firstly, it is uncertain which lithologies would have to be grouped without extensive petrophysical analysis of the units. The petrophysical analysis done by Fournier (2019) provides a good guide, but does not include all defined geological names. Secondly, it is expected that all units but the intrusive have little to no significant magnetic properties, with exception of the areas showing remanent magnetisation. However, since there is no clear consensus about the direction of the remanent magnetisation in these areas, the remanence cannot be included in the forward modelling. Hence, measurement values close to the remanent areas will not fit the forward model and these regions will have to be discarded to decrease its influence on the inversion as much as possible. Hence, for a simplified initial model, it is assumed to be sufficient to model the overburden, the intrusive body and the host rock.

GemPy constructs 3D models based on a defined extent of the model, the desired resolution and geological input data. As input data, it requires three things: Firstly, a minimum of two surface contact points containing 3D coordinates that define the bottom of each modelled lithological unit, secondly at least one orientation for each defined lithological unit, and thirdly a defined topological relationship (stratigraphic sequences). Considering the available geological information, two methods have been tested to build the geological model.

First, existing cross sections of the area (Figure A.2) are used to select interface points of the intrusive body. The overburden is not included in the cross section, thus we rely on borehole data for modelling it. It should be mentioned that these cross sections are expected to be outdated by now. We focus mostly on cross sections 11750N and 12750N as points from titan E5 and E6 lines do not show coherency in 3-dimensional space with cross sections 11750N and 12750N. Since there is no data regarding orientation measurements available, we are limited to rough estimate of dips and azimuths from the cross sections.

For the second method, available borehole data is used. After grouping the initially defined geological units, the base of the overburden and intrusive body are selected by visual inspection. We focus on boreholes that show consistency with neighboring boreholes regarding the base of the intrusion. Additionally, during selection we pay attention to the extent of the borehole after it pierces the base of the intrusion. The original borehole data shows significant layering in the intrusive body. In boreholes that do not pierce much further than the intrusion, it is not conclusive whether the last points of the UPX lithology was the end of a layering sequence or the actual base of the intrusive body. Eventually, the selected points are converted to the true vertical depth, Easting and Northing coordinates by taking the dips and azimuths of the selected boreholes into account. Using an azimuth α that is defined as the angle from North, positive towards the East, and the dip ω as negative downwards from the horizontal, the following coordinate transform is used:

$$\begin{aligned} X &= X_0 + r\cos(\omega)\sin(\alpha) \\ Y &= Y_0 + r\cos(\omega)\cos(\alpha) \\ Z &= Z_0 + r\sin(\omega), \end{aligned} \tag{4.2}$$

where X_0, Y_0, Z_0 are the coordinates of the top of the borehole, and r is the downhole depth to the selected point. For this model, we estimate the orientations by fitting a plane to the selected data points and finding a pole vector.

4.2.3. MAGNETIC FORWARD MODELLING

For the computation of the magnetic forward simulation, previous work by Talwani (1965) has been closely followed. The theory behind it and the different steps undertaken will be briefly discussed. We start off with the potential φ_i of a dipole which is given by (Blakely, 1995; Talwani, 1965):

$$\varphi_i = \frac{\mu_0}{4\pi}\frac{\vec{m}\cdot\vec{r}}{R^3}, \tag{4.3}$$

where $\vec{m}$ is again the dipole moment, $\vec{r} = x\hat{i} + y\hat{j} + z\hat{k}$ is the displacement vector from the center of the dipole to the observation point and $R = \|\vec{r}\|$. The constant $\frac{\mu_0}{4\pi}$, with μ_0 being the permeability in free space, is due to the use of the SI unit system. The magnetisation vector $\vec{M}$ of the whole body is then given by the sum of the magnetic moments per unit volume (Equation 3.5). Writing this in terms of vector $\vec{J}$ in SI units by using Equation 3.6 gives

$$\vec{J} = \lim_{\Delta V \to 0} \frac{\mu_0}{\Delta V} \sum_i \vec{m}_i. \tag{4.4}$$

The magnetic moment of element volume $\Delta x\Delta y\Delta z$ is then given by $\vec{m} = \frac{1}{\mu_0}\vec{J}\Delta x\Delta y\Delta z$, which can be substituted in Equation 4.3

$$\begin{aligned} \varphi_i &= \frac{1}{4\pi}\frac{\vec{J}\cdot\vec{r}}{R^3}\Delta x\Delta y\Delta z \\ &= \frac{1}{4\pi}\frac{\vec{J}_x\cdot x + \vec{J}_y\cdot y + \vec{J}_z\cdot z}{R^3}\Delta x\Delta y\Delta z. \end{aligned} \tag{4.5}$$

The magnetic scalar potential generated by the whole body is then the sum of these φ_i. When considering an infinitesimal volume, $\Delta x\Delta y\Delta z \to 0$, the summation transforms into an integral

$$\varphi = \frac{1}{4\pi} \iiint_V \frac{\vec{J}_x \cdot x + \vec{J}_y \cdot y + \vec{J}_z \cdot z}{R^3} dxdydz. \tag{4.6}$$

Considering that $\vec{B}$ is the negative of the gradient of the potential (Equation 3.3), the expression for field is given by $\vec{B} = -\nabla\varphi$ and the three orthogonal components of the magnetic field of an anomalous body are (Talwani, 1965):

$$\begin{aligned}
\Delta X &= -\int_{z_1}^{z_2}\int_{b_1}^{b_2}\int_{a_1}^{a_2} \frac{\partial\varphi}{\partial x} dxdydz \\
\Delta Y &= -\int_{z_1}^{z_2}\int_{b_1}^{b_2}\int_{a_1}^{a_2} \frac{\partial\varphi}{\partial y} dxdydz \\
\Delta Z &= -\int_{z_1}^{z_2}\int_{b_1}^{b_2}\int_{a_1}^{a_2} \frac{\partial\varphi}{\partial z} dxdydz.
\end{aligned} \tag{4.7}$$

The variables a_i, b_j and z_k give the distance from the corners of the voxel to the observation point p, as represented in Figure 4.4.

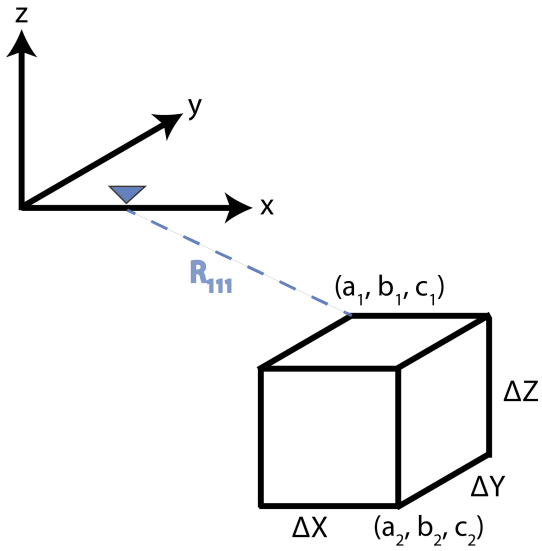

Figure 4.4: Schematic representation of the magnetic response calculation from a voxel. The observation point is represented in purple, the distance R_{111} is the distance to vertex (a_1, b_1, z_1).

Since the derivative of a sum is the summation of the derivatives, the substitution of Equation 4.6 into Equation 4.7 yields

$$\begin{aligned}
\Delta X &= \frac{1}{4\pi}(\vec{J}_x V_1 + \vec{J}_y V_2 + \vec{J}_z V_3) \\
\Delta Y &= \frac{1}{4\pi}(\vec{J}_x V_2 + \vec{J}_y V_4 + \vec{J}_z V_5) \\
\Delta Z &= \frac{1}{4\pi}(\vec{J}_x V_3 + \vec{J}_y V_5 + \vec{J}_z V_6),
\end{aligned} \tag{4.8}$$

where variables V_1 to V_6 represent the volume integrals (Talwani, 1965). The solutions of the vol-

ume integrals for the case of a prism are given by Plouff (1976). By taking one edge of the prism parallel as shown in Figure 4.4, Plouff (1976) obtained the following solutions:

$$
\begin{aligned}
V_1 &= -\sum_{i=1}^{2}\sum_{j=1}^{2}\sum_{k=1}^{2} s \tan^{-1}\frac{b_j z_k}{a_i R_{ijk}} \\
V_2 &= \sum_{i=1}^{2}\sum_{j=1}^{2}\sum_{k=1}^{2} s \ln(R_{ijk}+z_k) \\
V_3 &= \sum_{i=1}^{2}\sum_{j=1}^{2}\sum_{k=1}^{2} s \ln(R_{ijk}+b_j) \\
V_4 &= -\sum_{i=1}^{2}\sum_{j=1}^{2}\sum_{k=1}^{2} s \tan^{-1}\frac{a_i z_k}{b_j R_{ijk}} \\
V_5 &= \sum_{i=1}^{2}\sum_{j=1}^{2}\sum_{k=1}^{2} s \ln(R_{ijk}+a_i) \\
V_6 &= -\sum_{i=1}^{2}\sum_{j=1}^{2}\sum_{k=1}^{2} s \tan^{-1}\frac{a_i b_j}{z_k R_{ijk}},
\end{aligned}
\tag{4.9}
$$

where $R_{ijk} = \sqrt{(a_i^2 + b_j^2 + z_k^2)}$ is the distance from the observation point to each voxel corner. As an example, R_{111} in Figure 4.4 gives the distance from the observation point in purple, to the voxel corner annotated as (a_1, b_1, z_1). $s = s_i s_j s_k$ in Equation 4.9 gives the sign by $s_1 = -1$ and $s_2 = 1$.

At this point, several assumption have to be made in order to continue:

1. The susceptibility values k of each lithological unit in the geological model are assumed to be homogeneous and anisotropic throughout the unit and have to be known. Equation 3.11 is then used to find the magnetisation of each unit.
2. Magnetisation is only due to induction so that $\vec{J}_r = 0$ and following Equation 3.7, $\vec{J} = \vec{J}_i$.
3. The anomalous field is small compared to the undisturbed-field intensity so that the direction of the total field is said to be in the same direction as the undisturbed field, as discussed before, a general assumption in magnetic prospecting.

Assuming these conditions are met, the components of the magnetisation are given by (Talwani, 1965; Hinze et al., 2013):

$$
\begin{aligned}
\vec{J}_x &= \vec{J}\cos D\cos I \\
\vec{J}_y &= \vec{J}\sin D\cos I \\
\vec{J}_z &= \vec{J}\sin I.
\end{aligned}
\tag{4.10}
$$

Now all variables are known in order to find the components of the field as given by Equation 4.8. The intensity of the magnetic anomaly can be approximated by the sum of the projections of components $\Delta X, \Delta Y$ and ΔZ along the direction of the Earth's field B_e (Talwani, 1965; Blakely, 1995; Hinze et al., 2013):

$$
\Delta T = \Delta X\cos D\cos I + \Delta Y\sin D\cos I + \Delta Z\sin I. \tag{4.11}
$$

IMPLEMENTATION INTO GEMPY

In order to implement the described forward magnetics calculations into GemPy, the code had to be consistent with the GemPy architecture. Mainly the gridding of GemPy had to be taken into

account, in order to perform forward calculations in an efficient way.

GemPy supports different gridtypes. The already implemented gravity add-on was built on the centered grid. The gravity field decreases with $1/r^2$ where r is the distance from the source to the point of measurement (the observation point). GemPy takes this decrease of field strength into account and in this way saves unnecessary computational costs. The used centered grid is an irregular grid where the majority of voxels are centered around a defined value (or several values) which represents the observation point(s). This means that every observation point has its own grid. From the observation point, the grid spacing increases with r^2 where r is the distance to the observation point. While gravity fields are monopolar, magnetic field are dipolar, so the magnetic field strength decreases with a inverse cubed ($1/r^3$) relationship with distance. Hence, in magnetics, there is even less need to have a high resolution at these distant regions. Therefore, the forward magnetics is also built on this centered gridding structure provided by GemPy.

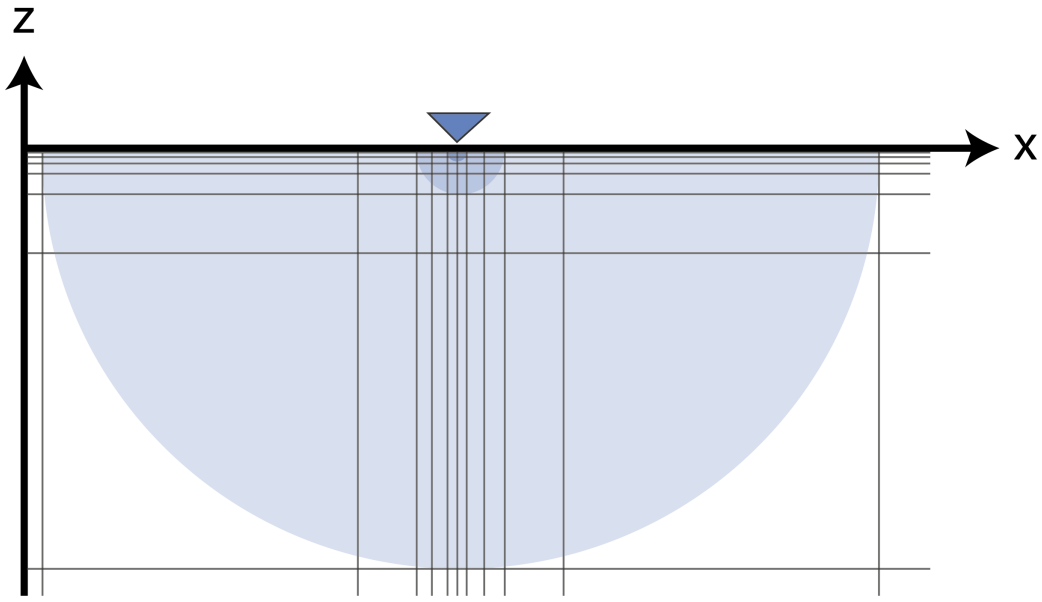

Figure 4.5: A 2D representation of the centered grid in GemPy where the forward magnetics is built on. The observation point (purple) is at the center of the grid. From here, the grid spacing increases with a distance squared relationship. The magnetic field decreases cubically with distance as shown by the blue hemispheres.

As shown in Equation 4.9, in order to compute the forward magnetics, the distances R_{ijk} from the observation point to each voxel corner need to be calculated (see Figure 4.4). By keeping the resolution of the centered grid for each observation point constant, the centered grid is constant, independent of how many observation points are added. This means that the distances R_{ijk} to the voxel corners are the same for each observation point. What changes per observation point, is the surrounding spatial distribution of susceptibility values: the susceptibility values assigned to the voxels. Hence, the forward calculation can be decomposed into a constant and variable part for each selected observation point. The solutions to the volume calculations $[V_1, .., V_6]$ from Equation 4.9 are kept constant since the input values R_{ijk} are constant. The variable parts are captured by Equations 4.7, 4.10 and 4.11, where the constant volume solutions for each observation point and the varying susceptibility values for each observation point are used to calculate the physically expected magnetic intensity at each observation point. The code is presented in Appendix B. The gridding is shown in Figure 4.5.

The computation of the forward magnetic is a required step for a coupled inversion. By embedding this step into a Bayesian inference, the initial input data for the model will be conditioned to the final magnetic response (de la Varga et al., 2019).

COMPUTING THE FORWARD MODEL

There are several factors to consider before computing the forward magnetics. First, in order to avoid boundary effects, the geological model has to be extended further than the area of interest. In this case, since the magnetic field strength decreases quickly, and no strong anomalies are expected in the forward model outside of the intrusive body, there is no need to extend the model very far outside of the intrusive body. Next, a 2D grid for the observation points where the magnetic response will be simulated have to be picked. For presenting the forward magnetics, a grid of 25×25 was used. The resolution of the centered grid was set to $[15, 15, 20]$.

In order to compute to forward magnetics, several study-specific parameters have to be set too: amplitude (intensity), declination and inclination of the inducing magnetic field, as well as a scalar susceptibility value for each modelled unit in the geological model. Applying this to the Kevitsa case study, the values for the inducing field are defined as $B_0 = [A : 53\ 349.7\ \text{nT},\ D : 10.1407°,\ I : 77.4063°]$ (NOA, nd). These are IGRF values corresponding to the month of the survey.

To simulate the magnetic response, we have to assign magnetic properties to the modelled units. We obtain susceptibility values per lithology by using downhole borehole measurements, and couple them to the defined lithologies at the depth intervals of the measurements. For this we use all available downhole measurements in order to capture all variability. Outliers are removed by visual analysis. Additionally all values smaller than 10^{-5} in SI are removed, assuming they are erroneous value.

4.2.4. SYNTHETIC STUDY ON A BURIED SPHERE

To validate the proposed methodology, a test model is used. First the forward calculator has been tested against an analytical solution. The test model is a sphere with a constant susceptibility, in a constant external field with only induced magnetisation. Due to the constant external field, the sphere will be uniformly magnetised. The magnetic potential due to an uniformly magnetised sphere is identical to the magnetic potential of a dipole located at the center of the sphere with a dipole moment equal to the magnetisation times the volume of the sphere (Blakely, 1995). Going back to the potential of a dipole, as given by Equation 4.3, and extending it to an observation location P outside of the sphere yields (Blakely, 1995; Hinze et al., 2013):

$$\begin{aligned} \varphi(P) &= \frac{\mu_0}{4\pi} \frac{\vec{m} \cdot \vec{r}}{r^3} \\ &= -\frac{\mu_0}{4\pi} \vec{m} \cdot \nabla_P \frac{1}{r}. \end{aligned} \tag{4.12}$$

Combining this with Equation 3.3 to find the magnetic induction of the dipole outside of the sphere gives (Blakely, 1995):

$$\vec{B}(P) = \frac{\mu_0}{4\pi} \frac{m}{r^3} [3(m \cdot r)r - m], \tag{4.13}$$

where $r = \frac{\vec{r}}{|r|}$ and $r \neq 0$, and $m = \frac{\vec{m}}{|m|}$ is the unit vector of the magnetic dipole moment $\vec{m}$ which is

given by:

$$\vec{m} = \frac{4}{3}\pi a^3 \vec{J}, \tag{4.14}$$

with a being the radius of the sphere. The components of $\vec{J}$ are again given by Equation 4.10.

The test model is a buried sphere, with its center at $[0,0,-300]$m, a radius of $a = 100$m and a magnetic susceptibility of $k = 1000$, located in a non-magnetic medium ($k = 0$). The inducing magnetic field is $B_0 = [A : 50000\text{ nT},\ I : 63.0°,\ D : 0°]$. The model is represented in Figure 4.6a. The result of this test is shown in Figure 4.6b. For the forward calculations, a grid resolution of $[100,100,100]$ is taken for the centered grids of the 51 observation points. It can be seen from figure 4.6b that the forward model fits the analytical solution well, with the calculated value at observation $[0,0,0]$ being only 0.14% off from the analytical value of the total field B_T.

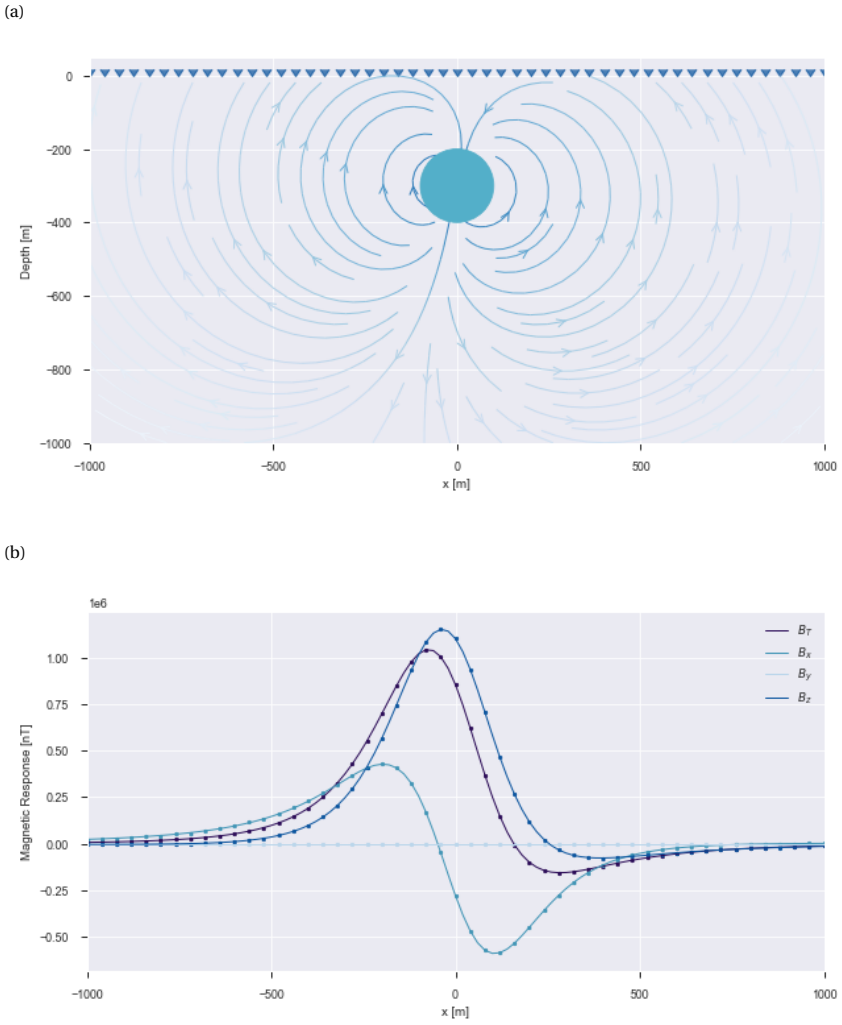

Figure 4.6: Validating the forward magnetic calculations with the analytical solution for a buried sphere. (a) Test model of the buried sphere. The triangles represent the 51 observation points along the x-profile that have been used for forward modelling. (b) Magnetic response of the test model. The lines represent the analytical solution and the dots are the calculated forward magnetics at the 51 observation points. Both the total field B_T and its components B_x, B_y, B_z are plotted.

4.3. INVERSE MODELLING

In reality, it is hard to encapsulate the complexity of the real situation by a model as there might be an infinite number of unknown, or at least not exactly known, parameters that describe the mathematical model. Each parameter that is defined as stochastic adds a dimension to the model space, and the curse of dimensionality starts to pose a problem. Effectively, this means that it is important that we choose our unknown parameters wisely and set up the probabilistic model with care. In this chapter, we present the tool and methodology for the implementation of Bayesian inference to our use-case. The process of Bayesian data analysis is divided by Gelman et al. (2013) in three steps. We will go through these steps one by one.

4.3.1. BAYESIAN ANALYSIS TOOL: PYMC3

PyMC3 is a Python library for Bayesian modelling and probabilistic machine learning, focussing on advanced MCMC algorithms (Salvatier et al., 2015). Similar to GemPy, PyMC3 also relies on Theano for automatic differentiation. This allows for the integration of both packages. The default sampling algorithm for continuous variables in PyMC3 is NUTS. All variables included in the probabilistic model have to be defined in PyMC3. The relation between variables is defined by parent-child relationships, where the parent affects the child variable and a variable can be both a parent as well as a child. PyMC allows for the inclusion of two types of variables in the probabilistic model: deterministic and stochastic variables. Deterministic variables are ones that are not random, meaning that if the hyperparameters of the variable are known, the value of the variable itself could be determined. Stochastic variables, on the other hand, would still be random if the variables' parameters were known. Stochastic variables are assigned a statistical distribution that is expected to describe the variable. PyMC3 includes a comprehensive set of pre-defined statistical distributions, which can be used as model building blocks. Additionally, the package provides default settings for both sampling algorithms and its parameters, a useful feature when the user has no algorithm fitting experience.

4.3.2. PROBABILISTIC MODEL BUILDING

Ideally, the probabilistic model should be consistent with our knowledge regarding the problem we try to solve. The elements that make up the probabilistic model have already been discussed in Chapter 3.2: unknown parameters θ, a mathematical model $\mathcal{M}$ that links the parameters with the observed data, and the observed data y. This can be any type of data, measurement or observation, that can be compared to the model outcomes. The model parameters do not have to capture all necessary knowledge that describes the data but should be rich enough to resemble the measurement process. The model parameter is defined as either deterministic or stochastic. Meaningful probability distributions have to be assigned to stochastic model parameters. In case there is no reasonable estimate for a parameter, a normal distribution can be used to capture its uncertainty (Davidson-Pilon, 2015).

As explained in Section 4.2.2, the starting geological model is completely based on geological knowledge, either cross-sections or borehole logs. These geological interpretations are highly subjective, hence the input parameters based on geological knowledge are expected to be highly uncertain. As observed data y, both airborne magnetic measurements, as well as geological interpretations from borehole cores, are used. To get a good understanding of the field data, it is analysed and processed as described in Section 4.1. The mathematical models relating the magnetic data and the geological observations to the parameters are the interpolator functions that form the basis of GemPy, and the implemented forward magnetic calculator described in Section

4.2.3.

Defining the observed and unobservable parameters results in a joint prior probability distribution. The definition of this prior distribution is a delicate issue in any Bayesian data analysis (Betancourt, 2018). The data, the parameters and the mathematical model all have to be understood well. The standard deviation should be chosen so that it contains all epistemic errors. A prior distribution encapsulating high uncertainty is preferred above a tightly defined prior. In the latter case, the prior may not contain the true parameter and will assign a probability of zero to the unknown parameter. Consequently the posterior will assign zero probability to it as well, and the MCMC will not converge.

This step aims to set our model up and define our parameters in such a way that the MCMC algorithm starts near the posterior distribution, to take little time to start sampling correctly. To analyse the joint ensemble, the prior predictive distribution can be analysed: the distribution for the observations over all possible values of parameters. The prior predictive distribution gives insights by quantifying the range of observations that are deemed to be in line with our modelling assumptions. This is done by taking random samples from the joint prior distribution, and passing these samples through the forward model, to quantify how likely it is that we can simulate the measured data given our prior parameters. If the measured data is not within the scope of the prior predictive distribution, the model should be adjusted to capture the relevant structure of the true data generating process.

4.3.3. CONDITIONING OBSERVED DATA

By conditioning of the data through a likelihood function $p(y|\theta)$ we can obtain the result of Bayesian inference: the posterior distribution $p(\theta|y)$. To embrace the Bayesian approach and update the prior knowledge in the light of observed data, well-defined likelihood functions $p(y|\theta)$ are needed. A well-chosen likelihood function concentrates in a small neighborhood of the model space and makes the structure of the prior parameter distributions less important, since the posterior distribution will be mainly dominated by the observations. In the case of a weakly- or non-identified likelihood function, however, the likelihood spans large volumes of the model space and has a small effect, the form of the posterior is then strongly influenced by the form of the prior. Without proper constraints, a poorly defined prior then propagates to a poor posterior. Hence, in case of a poor likelihood function, the prior distribution should contain just enough domain expertise to suppress extreme, unrealistic models.

In this project, likelihood functions based on both geophysical measurements and geological knowledge are used. The geophysical likelihood function is defined on basis of the measured airborne magnetic data. Since the spatial distribution of the petrophysical properties is related to the spatial distribution of the defined lithological units in the structural geological model, the observed data can be compared to the simulated response of the geological model by using the implemented forward magnetic calculator (Section 4.2.3). The susceptibilities that need to be assigned for this, can be either fixed estimated values, or could be considered to be uncertain by defining them as stochastic parameters.

It is expected that at greater depths, the magnetic field becomes too weak to provide a meaningful and informative likelihood function. To estimate the geometry at these depths, other constrains are needed. For this purpose, borehole data is used. Since GemPy computes the whole scalar field, the lithology can be defined at any point in space. GemPy assigns lithological IDs (integers) to each modelled lithological unit in sequential order. As explained, smoothing between lithology

transitions is applied to guarantee continuity of the gradient. In practice, this means that we can treat these lithology IDs as continuous variables and assign a probability distribution function to them. In this way, the probability of observing the intrusive unit at the logged location from borehole data is expressed as a likelihood function.

After including the observations in the form of likelihoods, the non-normalised posterior distribution can be approximated (Equation 3.16) by sampling using the NUTS algorithm as incorporated in PyMC3. For the necessary gradient information, Theano provides the derivative of the model parameters with respect to the likelihood functions. Since the model parameters themselves are functions of other input parameters, by using the chain rule for derivatives, the derivatives end up being summations and multiplication of all input parameters.

It is worth mentioning that both likelihood functions employ different parameters and require different levels of model construction during sampling. The geophysical likelihood requires the forward calculation of the magnetic field. All the input parameters needed for the forward calculation are combined to calculate a gradient. Once the forward modelling process is complete, the results of the gradient are collapsed back to the size of the vector of model parameters. Performing forward calculations for each sample, can quickly become a computationally expensive practice. The centered grid (Figure 4.9) used for the forward calculation eases the computation by employing high accuracy in the vicinity of the observation point, as the effect on the magnetic response is high here. Further away from the observation point, its influence decreases rapidly and the resolution can be decreased. Though this cuts the computational costs, densely covering the geological model extent with regularly gridded observation points would, if possible, still be very expensive. Hence, the observation points are chosen with care, based on the measured magnetic data and the objective of the inversion. The geological likelihood requires to know the lithology at the evaluated borehole location. For this, the construction of the geological model is necessary. Rather then computing the whole model extent, the geological model can be computed only at the given location in space by defining a custom grid at this location.

4.3.4. EVALUATION OF THE POSTERIOR MODEL

Once the model is built and the likelihood functions are defined, the sampling process can start. The chain will start moving from the prior distribution towards the typical set. PyMC3 automatically stores statistical parameters that capture the behaviour of the chain. Analysis of parameters like the moving means and the number of leapfrog steps per sample provides insights on whether the typical set in reached. Once in the typical set, moving means should show little variations, and the number of leapfrog steps taken should be low.

Analysis of the corresponding posterior estimates also provides an impression of the sampling adequacy. Similar to the construction of the prior predictive distribution, the posterior predictive distribution can be obtained from the joint posterior parameter distributions. This is called a posterior predictive check. The distribution produced in this way represents the data we would expect to measure if the proposed model was true and the sampler converged properly.

If there are indications that MCMC has converged, samples can be stored and used to characterise the posterior distribution. The analysis of the obtained posterior depends on the intended use. Here, we consider the analysis of the posterior distribution with a Gaussian kernel density estimation and an analysis of the ensemble of generated models from the posterior. The ensemble of models can be visualised in different ways. Wellmann and Regenauer-Lieb (2012) proposed the use of information entropy as an objective measure to evaluate model results. Information

entropy or Shannon entropy, after Shannon (1948), defines a scalar value at every location in the model representing its uncertainty. In analogy to entropy in thermodynamics, larger entropy means larger uncertainties. Additionally, if we want to produce a single estimate of the geological model, we can produce a model based on the maximum a posteriori (MAP) solution. This provides the model that statistically fits the observed data best. It should be mentioned that the MAP is not considered to be representative in high dimensional models, because it is usually not in the typical set (Betancourt, 2018). Additionally, it should be considered that a statistical fit does not guarantee representation of the geological structures.

Lastly, it is worth mentioning that in reality, a Bayesian workflow for practical applications is an iterative process (Betancourt, 2018). Both employed likelihood functions $(y|\theta)$ and prior distributions $p(\theta)$, are based on domain expertise. By evaluation of the posterior models, more knowledge about the interaction of the observations and priors is obtained. This creates new insights and might require re-definition of parameter distributions, or expansion of the model, without biasing our model by overfitting to the observed data. Hence, a correct response to a failing posterior predictive check would, in general, be expanding the model within the scope of our, possibly improved, understanding of the model (Betancourt, 2018). Once we have a new model we then restart the workflow and should iterate over the previous steps.

4.3.5. SYNTHETIC STUDY ON A BURIED SPHERE

To test the proposed probabilistic methodology, the buried sphere model from Section 4.2.4 is used again. We generate synthetic data by adding approximately 10% noise to the forward calculated magnetic response of the sphere (Figure 4.6). To show the iterative process of building a robust probabilistic model, several inversions are performed. First, we assume that we have no knowledge regarding the depth z (set at $z = 300$m) of the center of the sphere and we assign a uniform prior distribution $p(z)$ to it. A likelihood function based on magnetic observations at 7 points is added, using normal distributions. The effect of our likelihood $p(y_1, ..., y_7|z)$ on our posterior distribution $p(z|y_1, ..., y_7)$ is shown by comparison of two simulations. First, we define the standard deviation σ of the distribution as deterministic and assign this to all observations and take 500 samples. In the second test, we make σ stochastic, by assigning a half-normal distribution to it. For this test, we only take 200 samples. The results are plotted in Figure 4.7.

The distributions are represented using Gaussian kernel density estimation (KDE). The histogram of the posterior in Figure 4.7a is additionally plotted, to show that the sampled values are not in regions where we assigned zero prior probability, but rather result from the way the KDE is computed. KDE assigns a normal (Gaussian) curve to each sampled value, centered at that value. These curves are summed to compute the value of the density at each point and normalising the resulting curve. Since our prior distribution is non-informative, a well-defined likelihood function is needed. Defining a meaningful distribution is not trivial, and doing this for multiple observation locations even less so since the magnetic field changes rapidly with the position. This effect can be seen by looking at Figures 4.7b and 4.7c, which represent two different observation locations as highlighted in Figure 4.7d. The likelihood is well defined for observation (b) and converges to the true value already in the first test, but the second observation (c) does not do so well. Using a stochastic σ helps us define the likelihood better. The result is evident: where 500 samples for the first inversion still result in a poor posterior distribution for the depth location in the first test, 200 samples are already sufficient for the second inversion to get a good estimate.

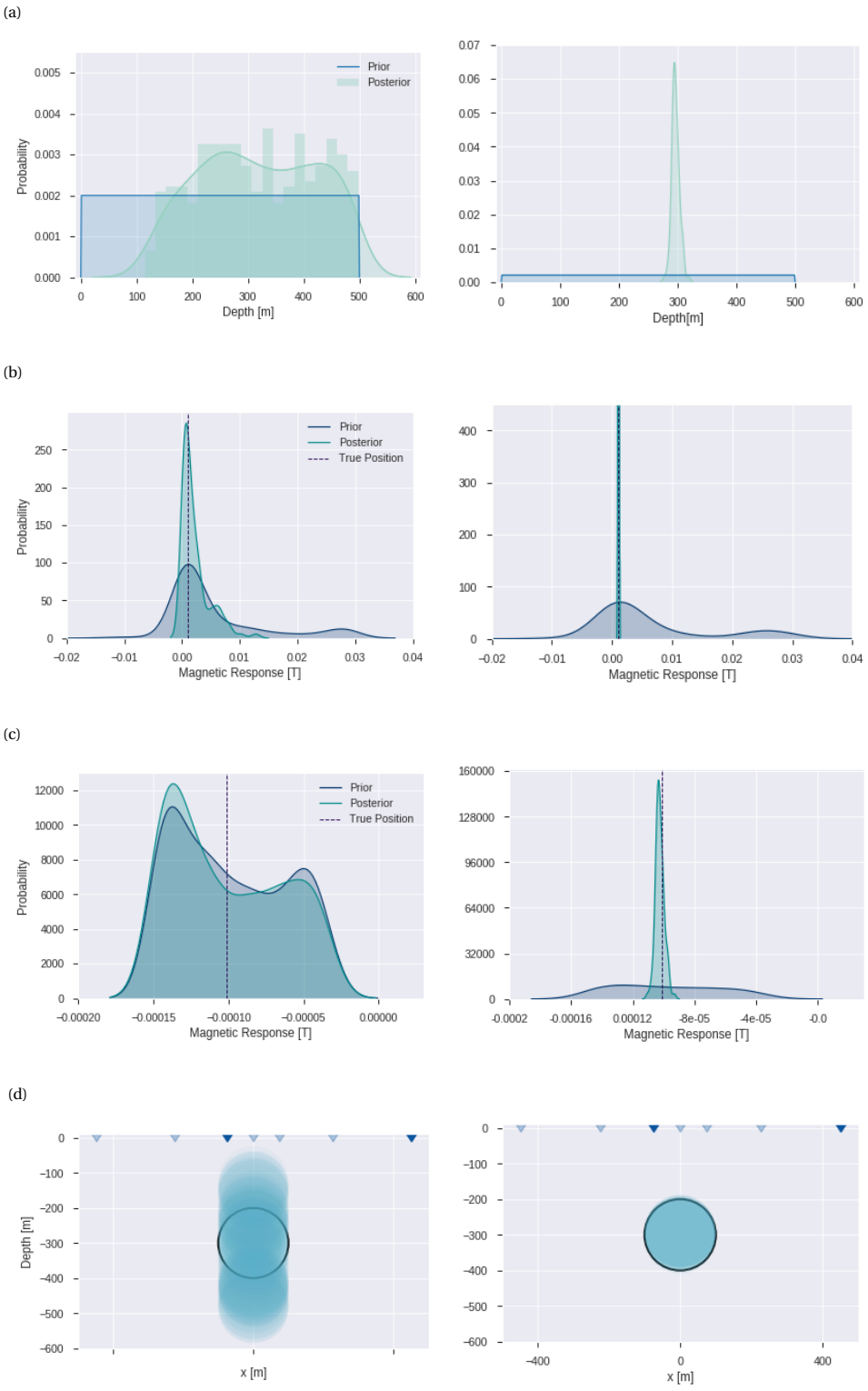

Figure 4.7: Testing the probabilistic model on a buried sphere with an uncertain depth. Two tests are conducted and presented per column. In test 1 (left) σ of the observation is deterministic, in test 2 (right) it's stochastic. (a) Prior and posterior distribution of the depth location. (b), (c) Posterior predictive checks of two different observation locations. (d) Estimates of the sphere location from the inversion (blue), and the real position of the sphere (black). The blue rectangles show the observation locations, where the highlighted two correspond to the observation points from (b) and (c).

After testing the sensitivity of the posterior to the likelihood, the complexity of the model is increased by adding the susceptibility k as a stochastic parameter. We assign a normal distribution to it, with $\mu_k = 900$ and $\sigma_k = 50$, while the real value is known to be $k = 1000$. We incorporate the newly gained knowledge about the distribution of z, by using the posterior from the first test. A normal distribution with $\mu_z = 320$m and $\sigma_z = 103$m is assigned as updated prior for z. The joint distribution is shown in Figure 4.8.

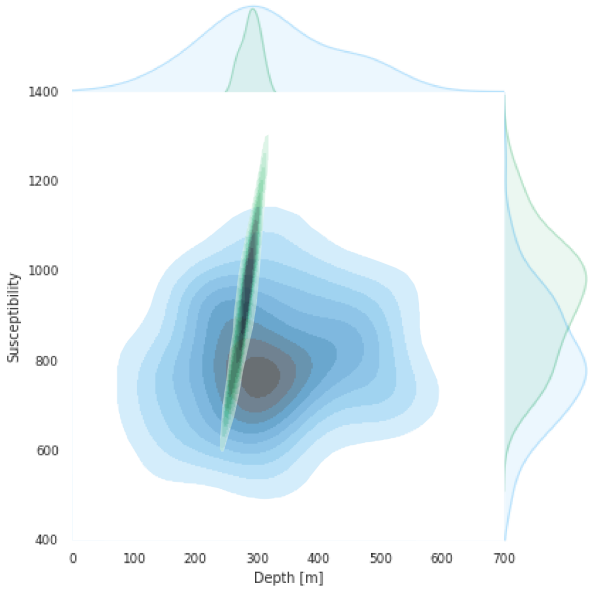

Figure 4.8: Joint plot for the prior and posterior of z and k.

The results show that a well-defined prior $p(z)$ provides a good estimate of the posterior $p(z|y_1, ..., y_7)$, whereas the poorly defined prior $p(k)$, combined with normally distributed likelihoods, results in a similarly shaped posterior. The joint posterior distribution is a thin surface, mostly due to the narrow posterior of z. Looking at the model realisations, we observe that adding a weakly informative stochastic parameter increases the total uncertainty. Lastly, it can be seen from Figure 4.9 that the MAP does not represent the posterior distribution.

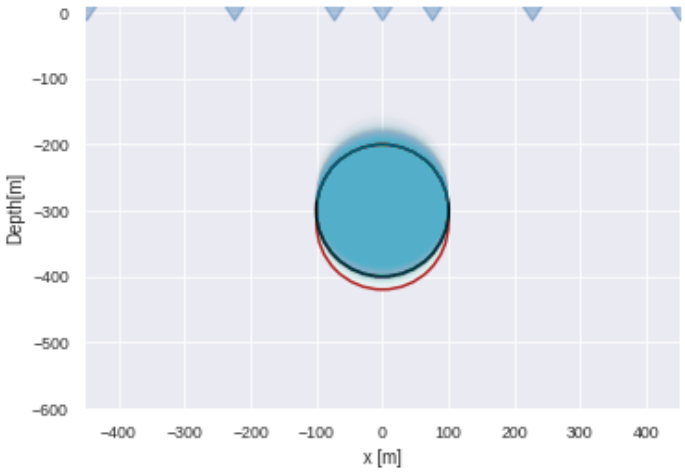

Figure 4.9: Model realisations (blue) for inversion with uncertain depth and susceptibility, with the true sphere location (black), and MAP (red).

These tests validate the set-up of our probabilistic model, while also showcasing the complexity of the probabilistic model building and the interactions of the parameters. The initial model has to be carefully chosen. It is better to start with a very simple model (few parameters and high uncertainties) and through iterations find better parameterisation, and increase the complexity

from there. Adding more likelihood functions to constrain the model, without understanding the model nor the observations that are being added, is likely to end up in unwanted interaction between the prior and the likelihood (Figure 4.7c). We can obtain precise estimates of the posterior distribution using small sample sizes when we use informative priors, but similar precision requires more sample size when we use weaker informative priors. In general, the observations can be summarised as follows:

- If the prior is non-informative, the posterior distribution will be equivalent to the likelihood functions.
- If the prior is informative, the posterior generally resembles the prior. The extent to which it resembles depends on the sampling size.
- For a given prior, large sample size will give the likelihood function more influence on the posterior.

5

RESULTS

In this Chapter, the results of this project are presented. First, the used field data is presented. This is followed by the built geological models and the results from the forward magnetic calculations. Lastly, the inversion results are presented.

5.1. FIELD DATA

The processed airborne magnetic data, cropped to the area of interest, is shown in Figure 5.1. The data is upward continued to 200 meters above the survey altitude. This upward continuation level is decided by testing different options. The result still shows the large-scale structural variations we are interested in while removing the small-scale variation related to variations in magnetic properties within the intrusive body (UPX).

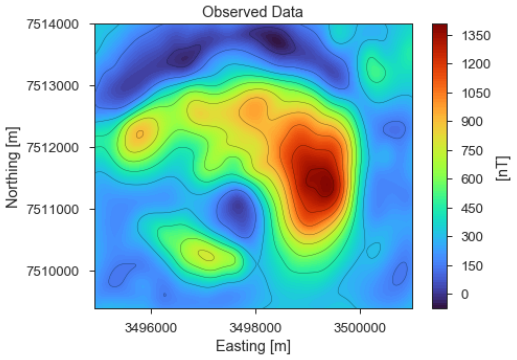

Figure 5.1: Processed airborne magnetic data showing the anomalous field.

The susceptibility k distributions of the modelled units, the intrusion (UPX) and the host rock, obtained from downhole borehole measurements are shown in Figure 5.2. Both distributions are plotted on a logarithmic x-axis to present the variations better. On the left, we see the separate k distribution of the lithologies that are grouped in the UPX unit, and the histogram representing the grouped distribution. The distribution for the host rock consists of all other lithologies, with the exception of the remanent dunite. This distribution is broader than the UPX distribution, which is expected considering the variety of lithologies that have been included here. However, the k values are at least one magnitude smaller than the k_{UPX} values, hence one would expect that the effect is not significant.

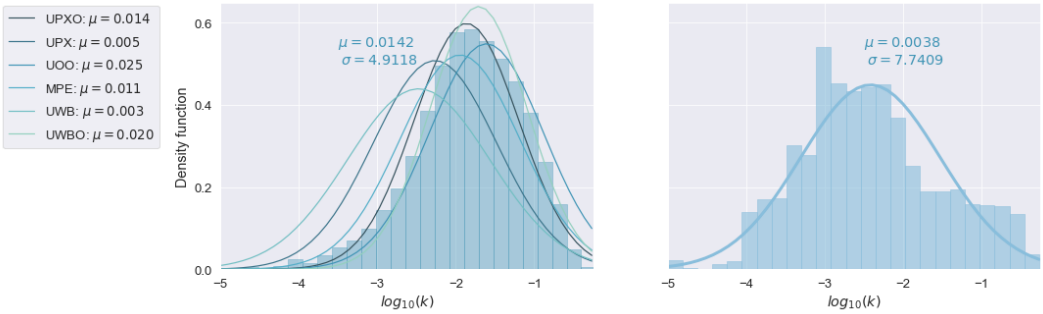

Figure 5.2: Histogram and distributions of susceptibility from downhole measurements for the intrusion (left) and the host rock (right). The histogram (left) represents the grouped intrusion (UPX unit), the individual distributions represent the units that make up the UPX unit. The other geological units, with the exception of the dunite (UDU), are grouped to obtain a distribution for the host rock.

5.2. FORWARD MODELLING

The extent of both geological models is from 3494800 to 3501100 Easting and 7509000 to 7513500 Northing in Finland KKJ coordinate system. The 3D presentation of both models is shown in Figure 5.3a and 5.3b for the cross-section based model and the borehole based model respectively. The surface representing the base of the intrusion UPX is in grey, the opaque surface represents the bottom of the overburden. The topography is not included in the 3D representation. To present the results also in a depth section, a cross-section at 7511750 Northing will be used as an example throughout this Chapter. Figure 5.3c and 5.3d show the cross-section of the initial models, where circles represent the input surface points and arrows the input orientations for the geological model construction. Figure 5.3e and 5.3f show the forward calculated magnetic response from the corresponding geological models. The forward calculations simulate the response as it would be measured at 200 meters above the survey level, to allow comparison to Figure 5.1. For both forward simulations, the same external and petrophysical parameters are used. For the external field we use IGRF values from the month of the data acquisition: $B_0 = [A = 53349.7\text{nT},\ D = 10.14°,\ I = 77.41°]$ (NOA, nd). The susceptibility values that we assign to the modelled units are the means of the presented distributions in Figure 5.8: $k_{UPX} = 0.014125$ and $k_{host} = 0.003846$ for the susceptibility of the intrusion and host rock. Additionally, we assign $k_{OVB} = 0$ for the overburden, since field geophysicists know the overburden to be non-magnetic in this region. By assigning a single susceptibility value per unit, we assume that k is homogeneous throughout the lithological unit. The forward calculations are performed on a regular grid over the extent of the geological models and interpolated using a minimum curvature interpolator.

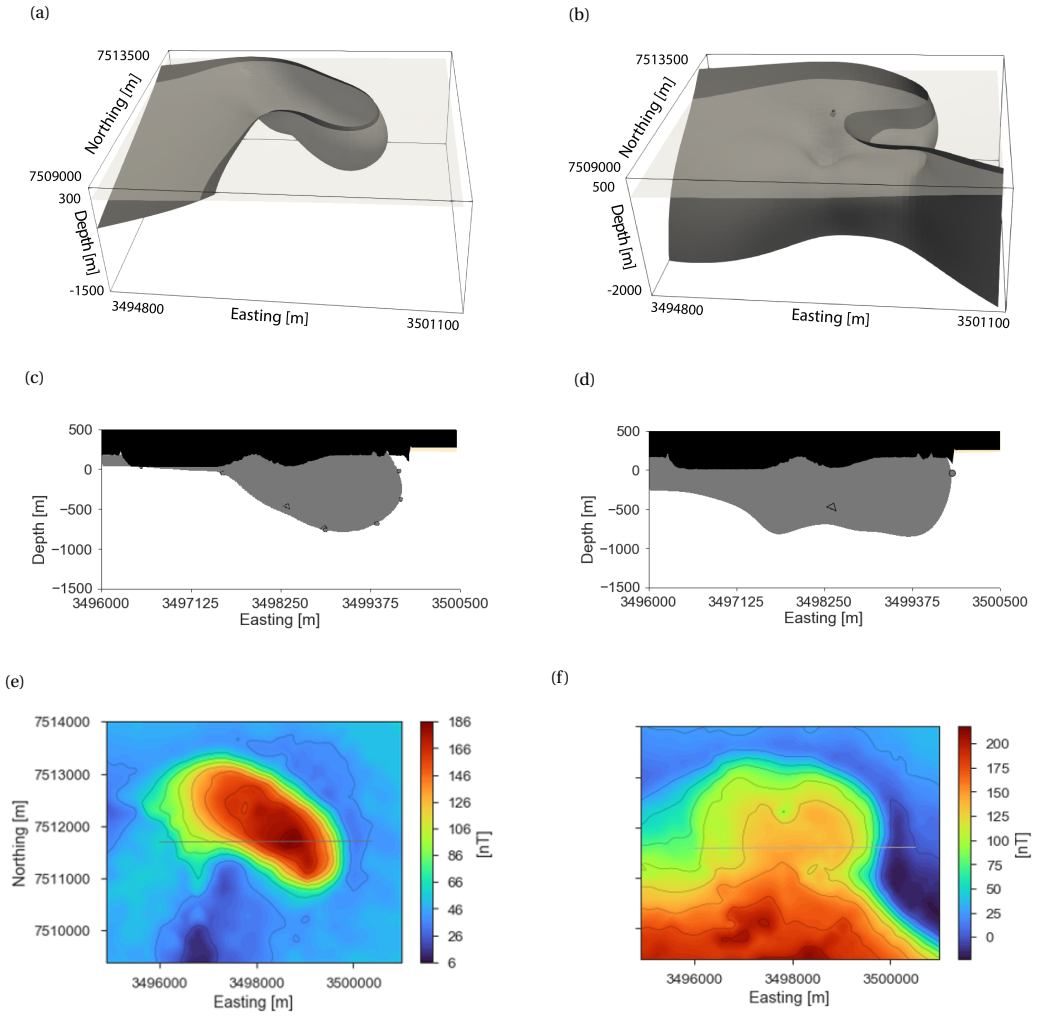

Figure 5.3: Created geological models and their forward simulated magnetic responses. On the left, we have the results from the geological model built from cross-sections, on the right based on borehole data. (a), (b) 3D representation of the models with the overburden in opaque and the intrusion in grey. (c), (d) Cross-sections at 7511750 Northing, taken as example cross-section. The circles represent the input points for the surfaces and the triangles are the orientations. (e), (f) The predictive forward magnetics, based on the models.

First, we compare the geological models. Where the cross-section based model (Figure 5.3a) estimates the geometry of the intrusive body to have a mostly bounded shape with the exception of the Southwest extent, the borehole based model (Figure 5.3b) suggests that the body extends to an unknown depth towards the South and Southwest. Both the provided cross-sections (in particular cross-section E5, Figure A.2) as well as the borehole data define the deepest point of the UPX unit at approximately 1500 meters depth. Yet, as mentioned in Section 4.2.2, cross-section E5 was not showing consistency in 3D with the selected points from the other cross-sections, hence this depth extent is not captured in the geological model based on these sections. As a result, we see that the base of the intrusive body in the cross-section based model is at a shallower depth. The base of the intrusion logged at greater depths is captured in the borehole based model, however, we can see in Figure 5.3b that this resulted in some artifacts. First, we see a small isolated point in the middle of the intrusion. Furthermore, based on geological knowledge, the steep dip towards the South is interpreted as a modelling artifact as well. This is likely due to scarce input parameters at greater depths since there were only two points that pierce the bottom of the intrusion

completely.

When we compare the resulting forward calculated magnetic responses presented in Figure 5.3e and 5.3f, they show consistency with the corresponding geological models. Comparing Figure 5.1 to the forward predictive models in Figures 5.3e and 5.3f, the most important observation are the values on the colour bar. The forward predictions have intensities that are approximately one order of magnitude lower. Both forward simulations cannot explain the measured data with the given parameters. An additional observation is that Figure 5.3f does not resemble the measured data at all. This is due to the simplicity of the geological models. It is known that in the South, a thick layer of gabbroic rock overlays the downward dipping intrusive body. Since we did not model this layer, the simulations are far off from the measured map. Therefore we expect that this geological model in the current state is too simplistic to be able to use magnetic likelihoods in the inversion. One would need to adjust the model by adding lithologies and possibly more surface points to get reasonable results. Hence, due to the scope of this project, it is decided to continue with the cross-section based geological model. Since we continue with one geological model, from here on the cross-section based model will simply be referred to as a geological model.

5.3. INVERSE MODELLING

The inversion is done iteratively, by starting with a simple probabilistic model and using newly gained knowledge in each step to improve the efficiency and results of the subsequent probabilistic model. In this Section, we will go through the different probabilistic models and the corresponding results of each inversion.

5.3.1. INVERSION USING GEOPHYSICAL LIKELIHOODS

I: DEPTH UNCERTAINY

The first inversion aims to observe the behavior of the prior distributions and the likelihood functions based on the measured magnetic data. To keep the probabilistic model simple, we only consider uncertainty at the depths z of the modelled surfaces. The geological model contains 22 surface points in total, each with a z-coordinate which is defined as stochastic, hence we end up with 22 stochastic model parameters in the probabilistic model. A normal distribution is assigned to these parameters to represent their uncertainty, with μ_z being the initial depth point that is used for building the model, and σ_z = 100m. Next, the observations for our geophysical likelihood function are defined. 12 measurement locations throughout the extent of our geological model are selected based on the map of the measured magnetic data and are shown in Figure 5.4. The used measurement values are from the 200 meters upward continued data. For the likelihood function, we use a normal distribution with μ_{mag} being the forward calculated magnetic response of the initial geological model, σ_{mag} = 100nT, and the measured magnetic intensity as observations. As mentioned before, the magnetic observations could not be simulated with the susceptibility values from downhole measurements. An attempt was made to run the inversion with the mean of the distributions presented in Figure 5.2. However, due to the large data misfit, the sampling process was extremely slow and it was concluded that either the geological or probabilistic model should be adjusted. For the next attempt, the susceptibility values have thus been scaled to simulate magnetic responses in the same order of magnitude as the measured data. Assigning deterministic k_{UPX} = 0.14125 and k_{host} = 0.03846, a total of 800 samples are taken. 300 samples are used as tuning samples and are discarded for posterior evaluations.

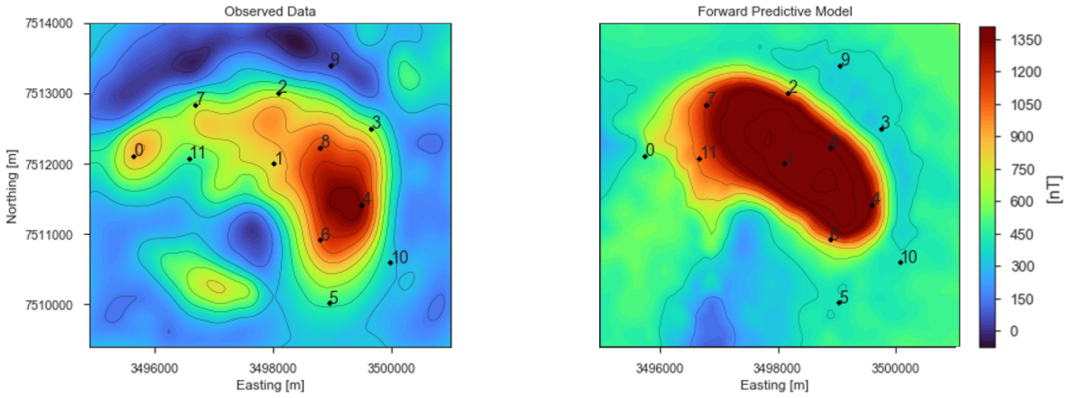

Figure 5.4: Selected observation points based on the measured data (left), with the corresponding points also shown on the forward simulated map with scaled susceptibility values (right).

Figure 5.5a shows the example cross-section with a set of the realised models and the initial model in the background and Figure 5.5b shows the uncertainty in the section based on all realised models and quantified by entropy. In Figure 5.5a we observe a decrease in volume of the UPX unit, by thickening of the overburden (OVB) and partially by decreasing depth of the base of the intrusion in some model realisations. The decrease of volume for UPX is an expected result: less volume (of UPX) is required to produce the same magnetic response that a body with lower susceptibility and larger volume would produce. Therefore the intrusive body is decreased in volume by decreasing the depth of the intrusion and thickening the overburden (OVB). Additionally, we see that the uncertainty is lower at the surface points, but is very high between the surface points. The surface points have a set range in which they can move in the z-direction, defined by the prior distribution. The regions between them, however, are interpolated automatically, hence we have less control there. Where Figure 5.5a visualises only a few (50) of the 500 considered samples, 5.5b quantifies the uncertainty by considering all 500 realised models. The entropy is calculated per cell (or voxel in 3D) by computing the probability of each formation to occur in that cell. If the probability of occurrence of one formation in a particular cell is one, then all others have zero probability and we have zero entropy. In the most uncertain situation, all formations are equally likely to occur, and their probabilities are equal: entropy is maximised. The maximum entropy is $log_2(n)$ where n is the number of modelled formations. Our geological model has 3 formations (OVB, UPX, and the host rock), hence the maximum entropy is 1.58.

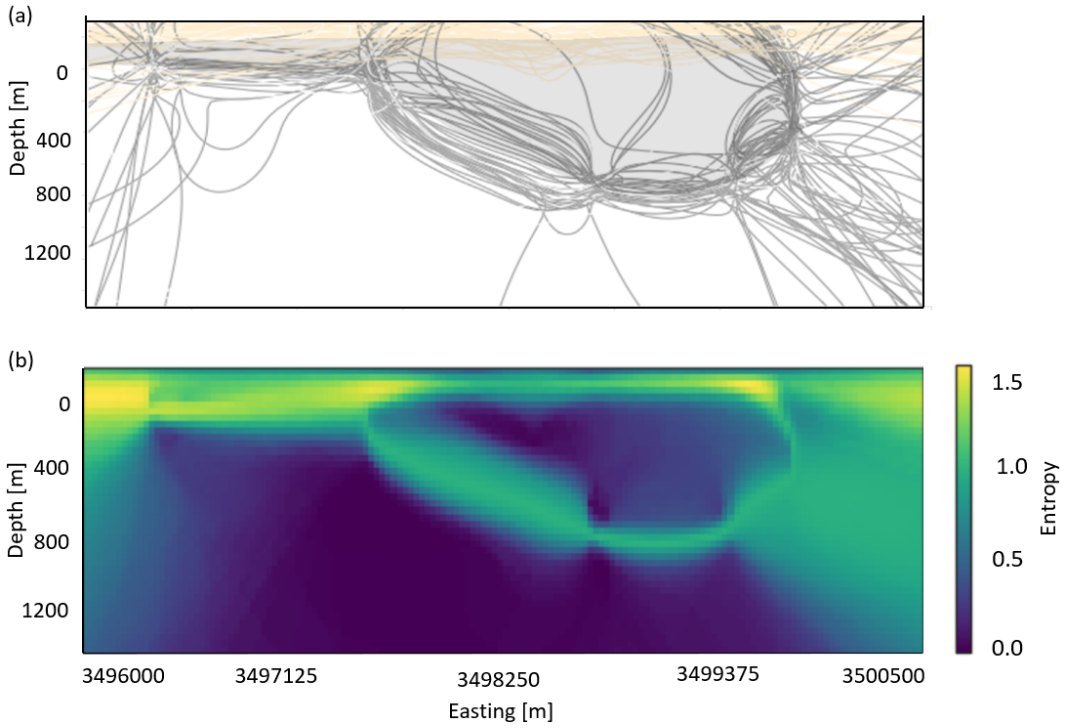

Figure 5.5: (a) Realised models of inversion, presented with the initial model on the background, shown on the example cross-section at 75117500N. (b) Representation of the uncertainty by plotting the Shannon entropy on the example cross-section. Higher entropy values mean more uncertainty or randomness, zero means that there is no uncertainty.

There are strong indications that this chain did not converge. A large number of samples reached the maximum leapfrog steps (by default 10) in the Hamiltonian trajectory, see Appendix A, Figure A.4. If the model is well defined, 10 steps would not, or at least not often, be required, as a better state would be proposed and accepted within these 10 steps. Hence, we should redefine our probabilistic model to ensure smoother exploration. Conducting posterior predictive checks gives insight on how to adjust the probabilistic set-up to improve the performance of the algorithm. The prior and posterior predictive distributions for all magnetic observations are presented in Figure 5.6, where the darker shades represent the prior and the lighter represent the posterior distributions. The dashed lines are the measured magnetic intensity values at these locations. It can be seen that all posterior distributions, except for observation 0, have moved towards the measured value (dashed line) relative to their priors. For most points, the measured value is not within the posterior distribution, which is in accordance with our belief that the model is poorly defined. It still performed unexpectedly well considering that most measured values are far in the tails of the prior predictive distribution (observations 3, 4, 7, 8, 11), hence having very little probability of being forward simulated, or are not in prior distribution at all (observations 1, 2, 9, 10), in which case there is zero probability to simulate the measured data within the current parameterisation.

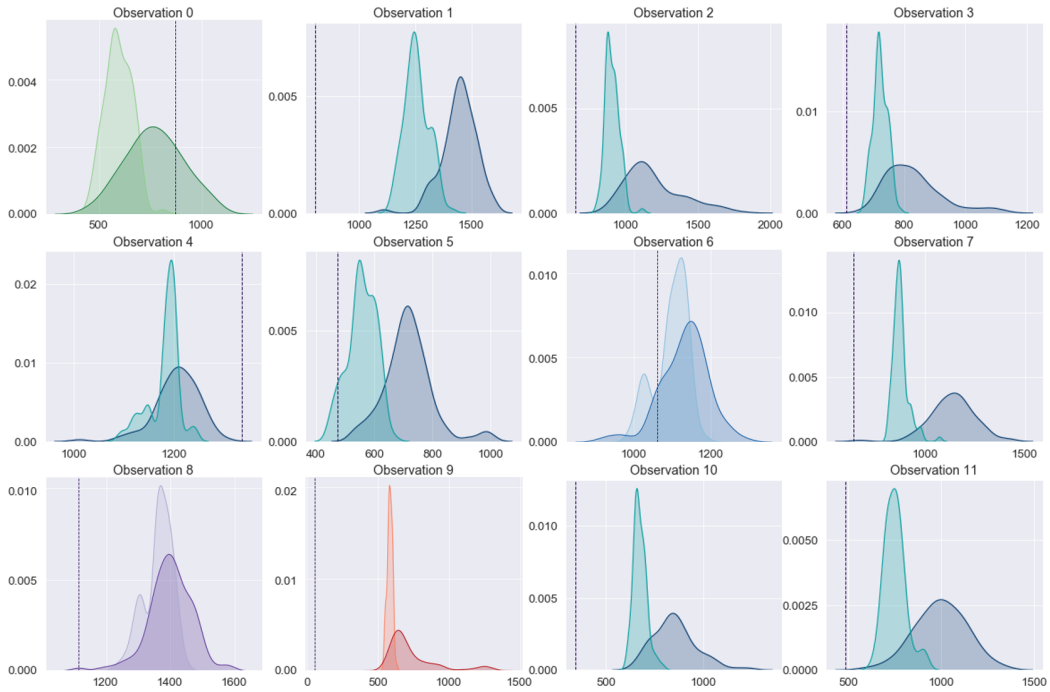

Figure 5.6: Posterior predictive checks for all observation in the geophysical likelihood function $p(z|y_0,...,y_{11})$. The dark shades represent the prior predictive, the darker shades the posterior predictive and the dashed lines the measured magnetic intensity at the location. The coloured observations (0, 6, 8, 9) will be used for comparison to future results.

Some important realisations from this inversion are:

- A justified representative susceptibility distribution has to be found for the intrusion to define it as a stochastic parameter rather than assigning it a fixed value. This is expected to highly impact the performance of NUTS.
- The model parameters need to be defined better so that the prior predictive distributions include the value of the measured data at the observation locations, and do not assign zero probability to it.
- The overburden should have a smaller distribution since core interpretations of the overburden are relatively certain compared to the more complex UPX unit. Additionally, we want to reduce its effect on the other parameters.
- The shape of the intrusion cannot be captured by only considering uncertainty in the z-direction.

II: PETROPHYSICAL UNCERTAINTY

To find susceptibilities k that explain the measured magnetic responses, we can invert for the rock property. With the current set-up of a surface-based model that assigns geophysical properties per formation, rather than on a grid, inverting for rock properties still respects the (expected) geology. The observation points are selected based on both the observed data and forward calculations since the observation points have to represent the correct modelled formation. The selected points are shown in Figure 5.7, where points 1, 8 and 12 are chosen as likelihoods for the susceptibility of the intrusion k_{UPX}, and point 9 is chosen as the likelihood for the susceptibility of the host rock k_{host}. We again assign normal distributions to represent the uncertainties, with the mean being the forward calculated values and for points 1, 8 and 12 we use $\sigma_{mag} = 100$nT. After

testing several configurations, it is decided to assign a stochastic σ with a half-normal distribution, to point 9. We assign uniform prior distributions to both susceptibilities: $U_{k_{UPX}} : [0.001, 0.1]$ and $U_{k_{host}} : [0.000001, 0.01]$. These bounds are chosen based on geophysical knowledge of the expected susceptibility values of magnetic and non-magnetic media.

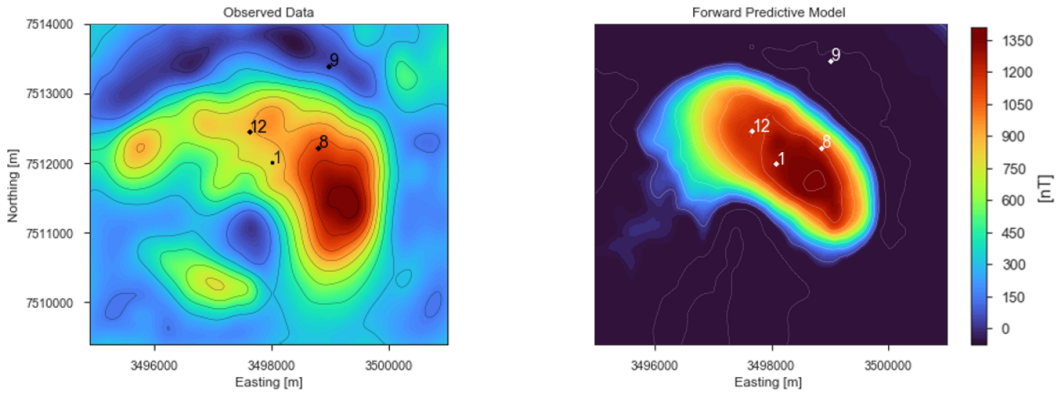

Figure 5.7: Selected observation locations for inversion II on the observed magnetic map (left) and the resulting forward calculated magnetic map (right). The magnetic response at points 1, 8 and 12 corresponds to UPX, and point 9 corresponds to the host rock. The resulting forward simulated map is obtained by using mean susceptibility values found through the inversion: $k_{UPX} = 0.12$ and $k_{host} = 0.0030$.

Figure 5.8 shows the resulting KDE plots. Figures 5.8a and 5.8b show the prior and posterior distributions for k_{UPX} and k_{host} respectively. Underneath them are the corresponding prior and posterior predictive distribution plots for observation 1 (Figure 5.8c) and observation 9 (Figure 5.8d). It can be observed that the distributions of the susceptibility and the corresponding observation location resemble each other. The uniform distribution assigned to both susceptibilities determines the shape of the prior predictive distributions: the data we would expect if the proposed model was true is also uniformly distributed. The shape of the posterior distributions is controlled by the likelihood functions: Observation 1 (Figure 5.8c) is located where UPX is modelled and thus the posterior distribution of k_{UPX} (Figure 5.8a) resembles (Figure 5.8c). The same relation holds for the host rock (Figure 5.8b) and observation 9 (Figure 5.8d).

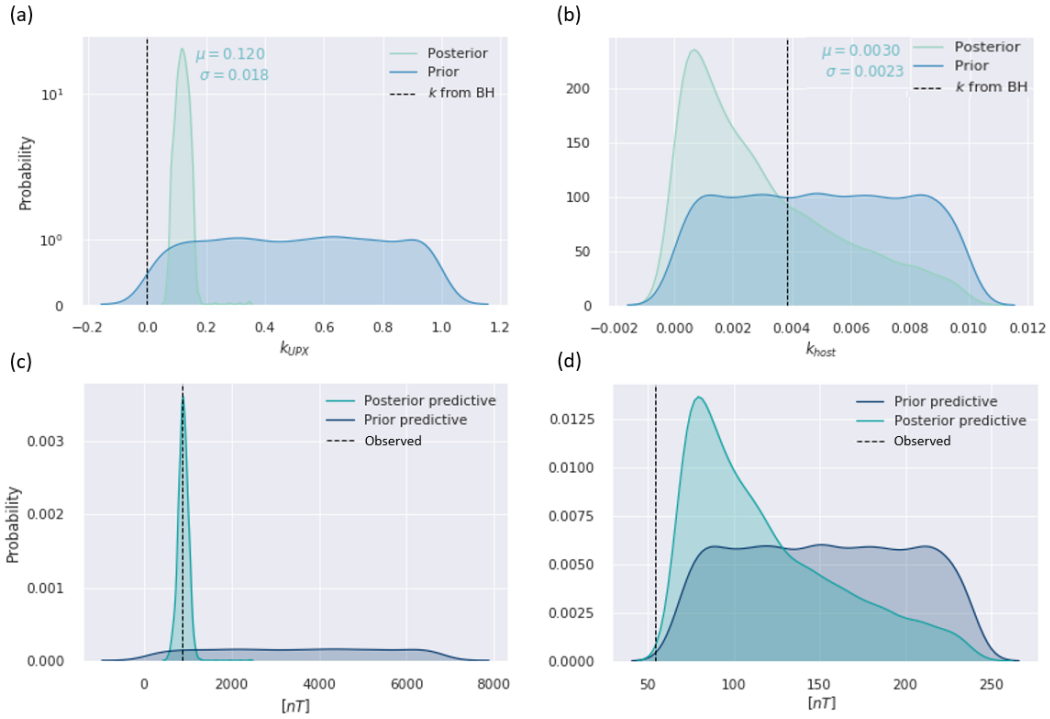

Figure 5.8: Prior and posterior distribution of (a) k_{UPX}, and (b) k_{host}. Prior and posterior predictive distribution for (c) observation 1, corresponding to the UPX unit, and (d) observation 9, corresponding to the host rock

Forward calculations with the inverted means of k_{UPX} and k_{host} are shown in Figure 5.7 (right). Comparing it to the measured data, we can see that the intensities over the intrusive body are in the same range. Therefore we can conclude that k_{UPX} represents the UPX unit better than the value that was obtained from the borehole data. The result for k_{host} is less certain, as only one observation was used and the obtained posterior distribution exactly resembles the posterior predictive at observation 9 (Figure 5.8d). This posterior predictive in its turn gets its shape from the half-normal σ that was assigned to the observation point (Figure 5.8d). Note that the other observation points (1, 8, and 12) included in the likelihood functions have a deterministic σ. The inversion was tried with a deterministic σ for point 9 too, which resulted in a uniform posterior for k_{host}. The result is plotted in Appendix A, Figure A.5. Adding additional observations in the likelihood functions to represent the host rock (e.g. towards the East of the intrusion) has been tested too, but resulted in either a non-informative uniform-like posterior distribution or even a slightly larger mean value for k_{host}. Hence, it is concluded that the inversion does not provide a trustworthy result for k_{host}. The result shown in Figure 5.8b is only obtained after adjusting the assigned distribution to the observation point in such a way that we would get a result. Hence, the resulting probabilistic model is highly biased to fit the data and the result is considered subjective. Therefore it is decided to continue with the newly found k_{UPX}, but we discard the result for k_{host} and continue using the downhole measured values. It is not expected to harm the inversion much since the borehole value is close to the inverted value and both are significantly smaller than the newly found k_{UPX}. Therefore the susceptibility of the host rock is expected to have a minor influence on the magnetic field intensities observed directly on or around the intrusion.

III: SPATIAL AND PETROPHYSICAL UNCERTAINTY

With our updated knowledge, we can extend our probabilistic model. The Kevitsa intrusion is located in a highly structurally deformed geological setting, so it can be assumed that there is,

at least to some extent, uncertainty in all spatial directions. Hence, for the next inversion, the x, y, z-coordinates of all surface points are defined as stochastic with normal distributions and the input values as the mean. The assigned σ is dependent on the unit: $\sigma_{OVB_{x,y,z}}$ is set to 2 meters, $\sigma_{UPX,x,y,z} = 300$m. Additionally, we expand the likelihood function by adding more magnetic measurement points, again with a normal distribution assigned to the observations. The large uncertainty assigned to UPX is motivated by the selected points. Most points are chosen around the magnetic anomaly, and we can observe from the shape of the measured anomaly (Figure 5.9, left) that the initially modelled intrusion (Figure 5.9, right) should be moved a few hundred meters in the horizontal plane to resemble the measured anomaly. We assign the posterior distribution of k_{UPX} from our previous inversion (Figure 5.8) as prior distribution for this inversion, and keep $k_{host} = 0.003846$ and $k_{OVB} = 0$ deterministic. The prior for the observations (prior predictive) shows that the magnetic data could, at most observation locations, be explained within the assigned parameter uncertainties. This is mainly due to the redefined susceptibility.

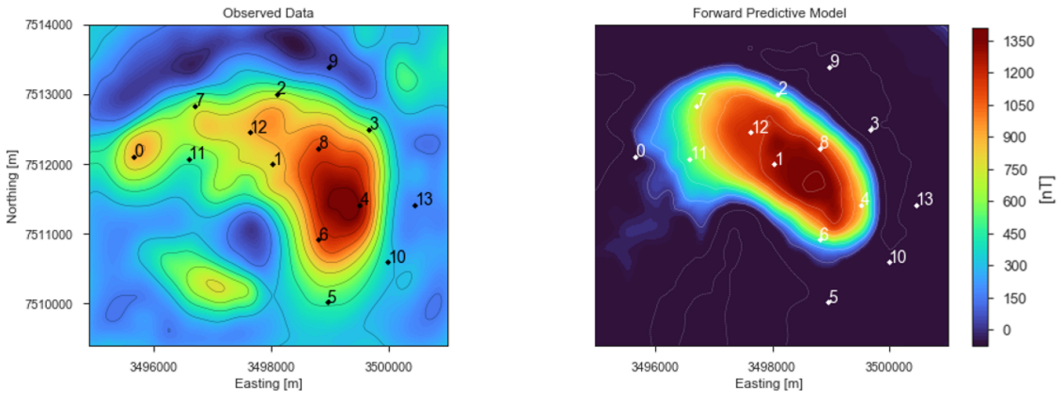

Figure 5.9: Selected observation points based on the measured data (left), with the corresponding points also shown on the forward simulated map with susceptibility values found in inversion II (right).

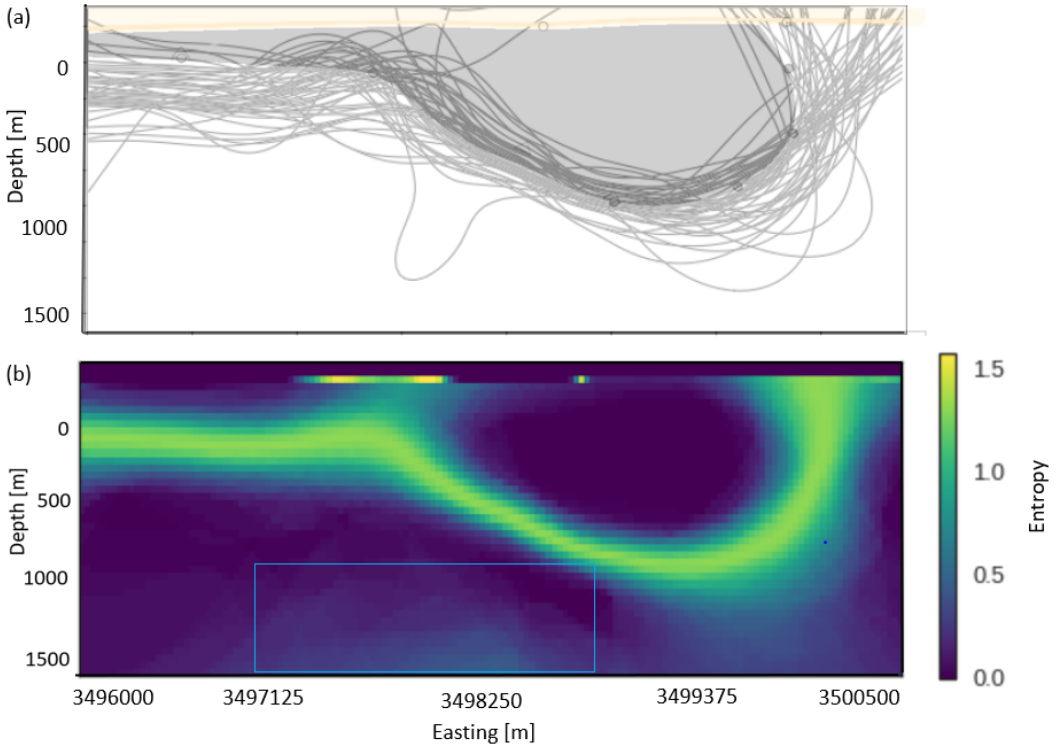

Figure 5.10: (a) Realised models of inversion III presented with the initial model in the background, shown on the example cross-section at 7511750N. Again, only 50 of the 500 realised models are plotted to maintain visual clarity. (b) Representation of the uncertainty in terms of entropy shows that overall the entropy has decreased, yet uncertainties arise at new locations, mainly at unexpected locations within the area highlighted by the blue box.

To have a fair comparison, we take the same amount of samples as in inversion I (800). The realised models are shown on the example cross-section, shown in Figure 5.10. Compared to Figure 5.5, we observe that there is no strong 'bow-tie' effect at the surface points. This is likely related to the now stochastic x and y-coordinates, which allow for variations of the surface points in all three directions, resulting in more coherent interpolations between them. From Figure 5.10b it can be seen that overall the uncertainty has decreased, but some new effects occur at the bottom of the section as highlighted by the blue box. It looks like these regions show individual bulbs, disconnected from the main intrusive body. This also occurs in the other sections (Figure A.9). Based on geological interpretation (mainly from seismic data at this depth), it is not expected that these features are representative of the subsurface structures. Therefore, these effects are interpreted as artifacts. Note that the section in Figure 5.10a does not show these artifacts. This is because, for visualisation reasons, only 50 of the 500 sampled models have been plotted. If all models would have been plotted, these artifacts would indeed also be visible in the section in Figure 5.10a. The high entropy at the interface between UPX and the overburden is interpreted as being the result of the thinness of the overburden, in combination with the resolution of the grid on which the entropy is calculated. Since the overburden is so thin (and stochastic), the occurring formation in a cell in these zones interchanges quickly per sample and hence both OVB and UPX have a probability to occur in a particular cell and the resulting entropy is high. The prior predictive check indicates that the target distribution is reached since our posterior predictive distributions are either centered at or close to the observed value. The wide, non-smoothed, distributions indicate that the typical set is not sufficiently sampled yet to fully converge. The prior and posterior predictive distributions of all magnetic observations are plotted in Figure A.6, Appendix A.

5.3.2. INVERSION USING GEOPHYSICAL AND GEOLOGICAL LIKELIHOODS

IV: SPATIAL AND PETROPHYSICAL UNCERTAINTY

In general, the results of the previous inversion are satisfying as the posterior check suggests that the model can explain the data. However, from geological knowledge, it is expected that the body extends deeper than it does in our geological model. By assigning more uncertainty to z from inversion I to III, we still did not capture this, and additionally created structures that are expected to be artificial. Hence, within the previous probabilistic model, the data could be fit, but our mathematical functions could not simulate the expected geology. To add information to the inverse model, a geological likelihood based on interpreted core logs is added at location $BH_1 = ([X : 3498946,\ Y : 7511059,\ Z : -1468.448499\text{m}])$, as shown in Figure 5.11.

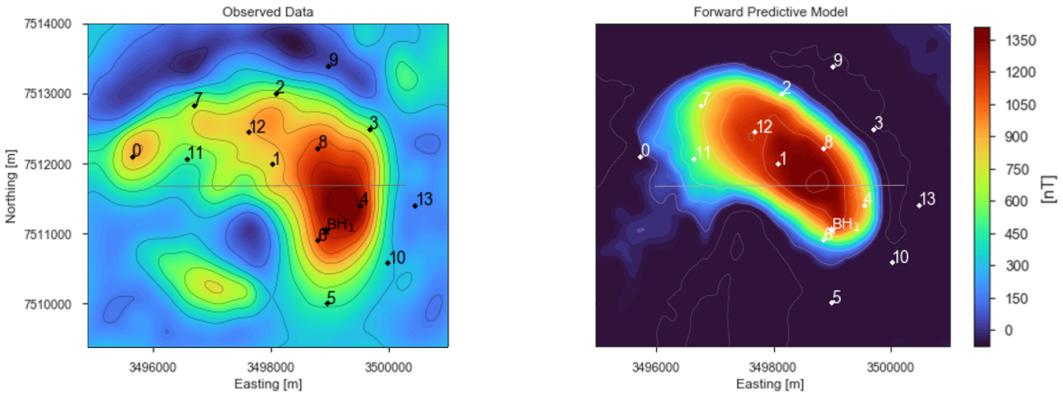

Figure 5.11: Selected observation points based on the measured data (left), with the corresponding points also shown on the forward simulated map with inverted k_{UPX} (right). The location of the cross-section is shown by the line in order to see it's relative location to the added borehole data from borehole BH_1.

As mentioned before, to guarantee a smooth gradient for the automatic differentiation, GemPy smooths between sharp formation transitions: if $k_{OVB} = 0$ and $k_{UPX} = 0.12$, there will be a very thin transition zone where the susceptibility varies between these two extremes. This goes for each property assigned to the formations. We can exploit this functionality by considering the formation ID (1 : OVB, 2 : UPX and 3 : host rock) to be a continuous variable. In practice, this means that the ID at any point in our geological model space can range between ID 1 and ID 3. By adding the x, y, z-coordinates of the borehole where the bottom of the intrusion (ID 2) is logged, and assigning a probability distribution to encapsulate the uncertainty, a geological likelihood can be added to the inference. Since this point is logged as the transition from the intrusion to surrounding rocks the formation ID value at this point will be between 2 (intrusion) and 3 (host rock). Hence, we define the likelihood by using a normal distribution, with μ being the forward computed ID at the grid point, $\sigma = 0.4$ so that the probability is zero after a unit step and the observed value is ID 3 (host rock). The posterior predictive checks for the observations are included in Appendix A, Figure A.7.

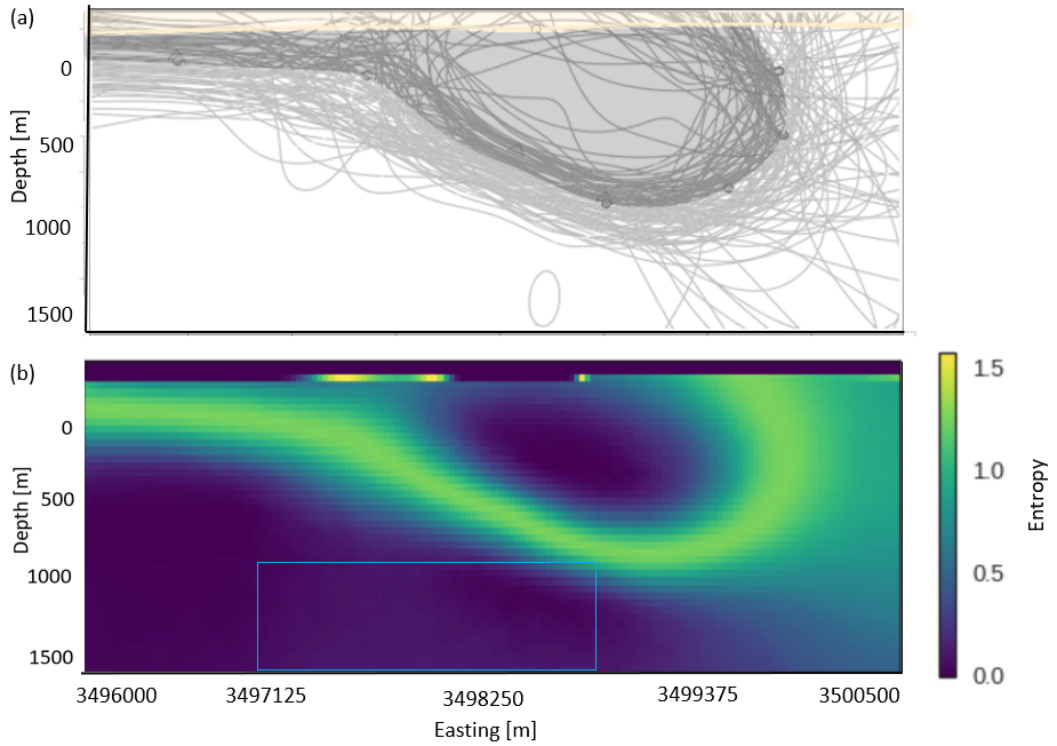

Figure 5.12: (a) Realised models from inversion IV presented with the initial model on the background, shown on the example cross-section at 7511750 Northing. (b) Representation of the uncertainty by plotting the Shannon entropy on the example cross-section. The box represents the zone where uncertainty occurred as a result of the previous inversion (Figure 5.10).

Figure 5.12b shows that the addition of the geological likelihood function removed the artifacts from the previous inversion, even though the added borehole data is approximately 700 meters South of this section. In general, the uncertainty in the section has increased, mostly on the East-side. The geological likelihood increased the number of realised models that extend deeper into the subsurface compared to the previous inversion(s), which it was exactly meant to do. To reduce uncertainty, more geological observations can be included in this way. Note that Figure 5.12a still shows a model realisation that shows some artifacts (the bulb we wanted to remove). The use of information entropy, in this case, shows its power, as it takes all realised models into account. The artifacts might still occur in a very small subset of realised models, yet the number of these model realisations has been reduced so much that they do not pose uncertainty in the model posterior anymore.

Additionally, inversion IV with the same geophysical and geological likelihoods has been performed with slightly different parameterisation. To test whether the observed data could be included in the prior predictive distribution, and hence obtaining a better probabilistic model set-up, we increased the uncertainty in σ_{kUPX} from 0.20 to 0.26 and additionally increased the uncertainty in the observations where the measured data was in the tails of the prior predictive. Additionally, 3000 samples have been taken. The results of this test are shown in Figure A.8. We observed that this set-up resulted in very different distributions. Ignoring the smoother and narrower distributions due to the higher sampling number, the difference is mainly that at some locations the observed data fit better (e.g. location 0, 1) but in general the fit was worse. The effect is likely due to increased uncertainty in k_{UPX} and its dominant influence on the likelihoods. Due to the high dimensionality of the problem, there are endless possibilities of how changing uncer-

tainty in the observations and the main controlling model parameter of these observations can reshape the model space. The chain likely got stuck in a region of model space that, due to different parameterisation, now gained a higher probability. Due to this, it did not manage to explore the rest of the distribution within the given sample size. Due to the different setup compared to inversion I, III and IV, which consistently took 800 samples, we do not further analyse the results of this test.

5.3.3. JOINT ANALYSIS

In this Section, we evaluate the progress throughout the different inversions by analysing the statistics and trying to link their interpretation to the geological realisations. 4 magnetic observations are selected to discuss in greater detail through the posterior predictive checks presented in Figure 5.13. Inversion II is excluded in this comparison since the inversion had a different focus. From I to III, it can be observed that there is a great improvement as the distributions get closer to the observed value and most of the unwanted non-smooth behavior of the distribution (observation 8), and extended curved tails (observation 9) are removed. This is a direct result of the introduction of the well-defined stochastic k_{UPX}. In general, the data is well fitted in III. The results are almost the same for inversion IV. We can conclude that, in this case, the added geological likelihood does not seem to affect the parameters that control the magnetic observations.

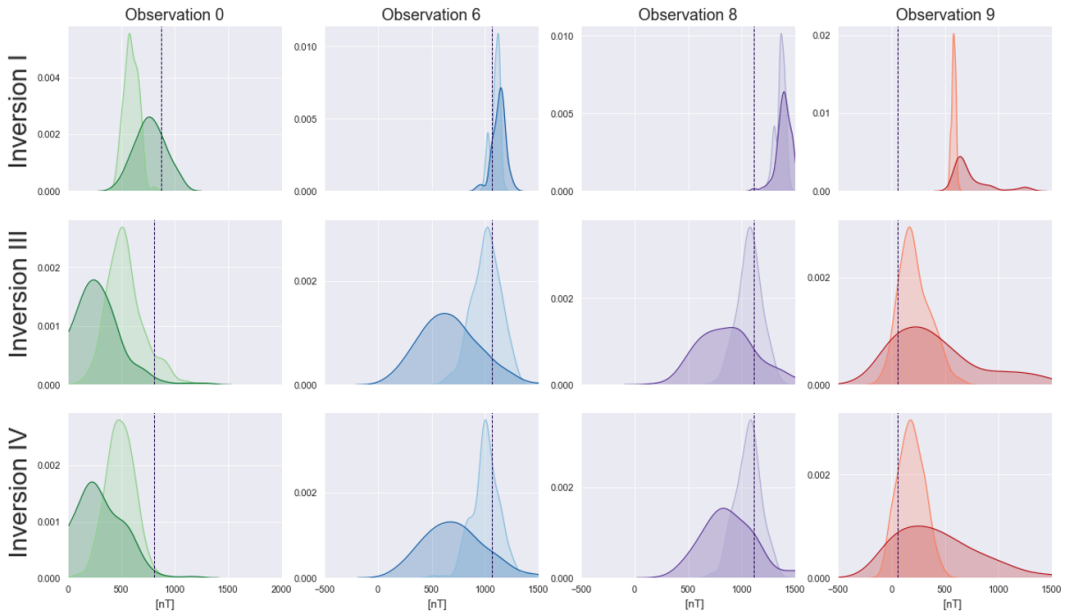

Figure 5.13: Comparison of posterior predictive checks of inversion I, III, IV, for selected magnetic observations. The darker shades represent the prior and the lighter the posterior distributions. We can see that there is little change from inversion III to IV since the parameters have not been adjusted.

A posterior predictive check for the geological likelihood (Figure 5.14) shows that the shape of the predictive distribution has hardly changed. This is due to the low number of model realisations that showed the artifact in 5.10b, a conclusion we can draw from the relatively low entropy compared to other parts of the section. Since the number of models that show these artifacts are already low, the exclusion of these models (by assigning 0 probability to them through the likelihood) does not change the posterior much. This conclusion can be directly related to the unchanged posterior predictive from inversion III to IV. Additionally, we expect that structures at these depths do not influence the magnetic data anyway. Hence, the effect of this particular

geological observation on the likelihood of the magnetic observations would be expected to be minimal in any case.

Since the smoothed transition zone between formations is just smooth enough to allow for a gradient, but still considerably sharp, this zone where the formation ID can vary between two integers occupies a very small space in the geological model. Any value between 2 and 3 would mean that we are in the narrow transition zone between UPX and the host rock. Hence, this geological likelihood has proven to be very effective.

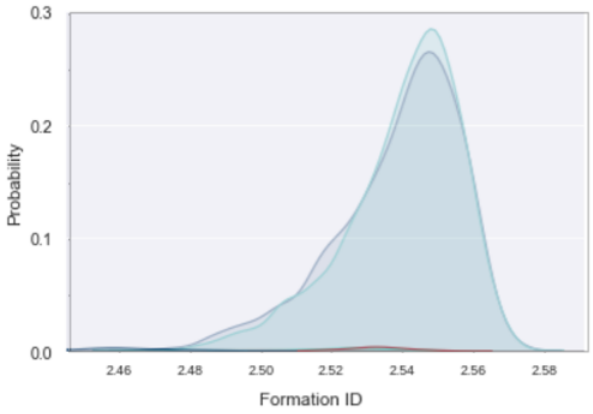

Figure 5.14: Prior and posterior predictive distribution of the borehole observation. The observation was the interface between UPX (ID:2) to host rock (ID:3), hence a normal distribution with the $\mu = 3.0, \sigma = 0.4$ is added as likelihood function to constrain the ID number between 2.0 and 3.0

To obtain one single optimised model from the final results (inversion IV), the MAP is computed. The obtained values for the unknown parameters x, y, z, and k_{UPX} through MAP are used to create a new geological model and simulate its magnetic response. The results are shown in Figure 5.15 (right) together with the initial model (left). It can be seen that our geological model has not changed. This is due to the result of MAP for our spatial x, y, z-coordinates, which only differ -10^{-8} order of magnitude from our initial input values. The magnetic response is found as $k_{UPX} = 0.11$, a slight change from the prior mean $k_{UPX} = 0.12$. The MAP is found by maximising the joint posterior distribution. Since in this case the posterior is mainly dominated by k, this effectively means that k_{UPX} is maximised. Hence, we did not gain any knowledge regarding the spatial parameters whereas, from the cross-sections presented in Figure 5.12 it is clear that these vary in the posterior.

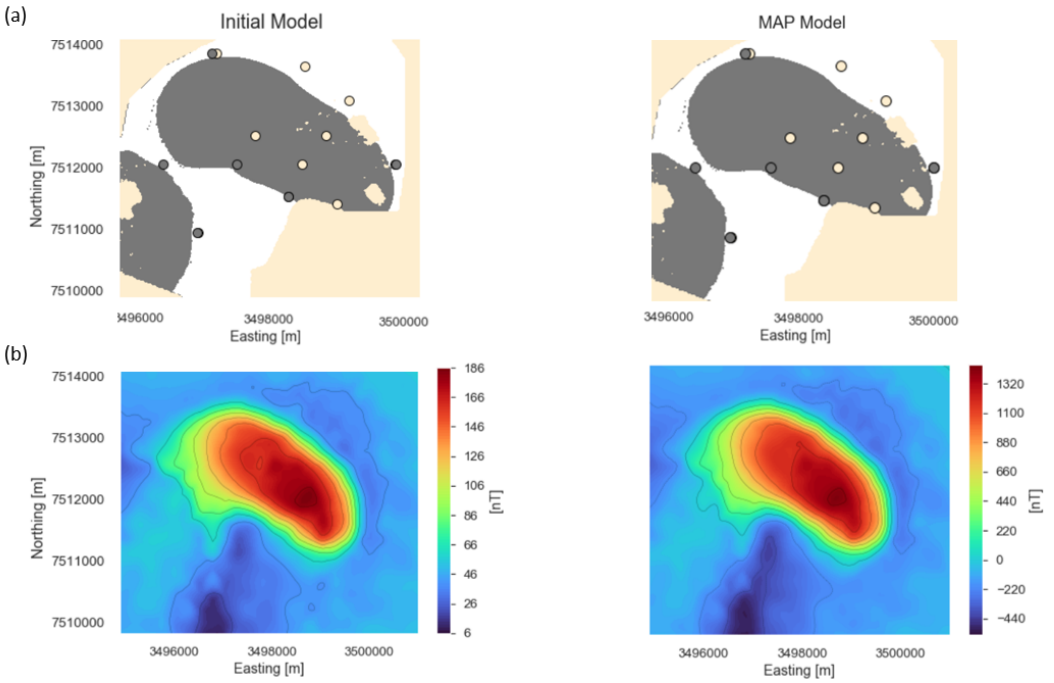

Figure 5.15: Comparison of the initial model (left) to the model constructed from the MAP output (right). (a) The geological map has not changed, since the MAP spatial variables x, y, z differed very little from the initial input parameters. (b) The magnetic response of the geological model has changed in intensity as shown in the colour bar. Note that this is similar to $\mu_{k_{UPX}}$ from inversion III and IV and hence we did not obtain any new information by computing MAP.

6

Discussion

6.1. Geological Modelling

In order to capture the geometry of the intrusive body using geophysical constraints on the inversion, it was deemed sufficient to model the intrusion (UPX), the overburden (OVB) and the host rock. This choice is justified by (1) the lack of an extensive petrophysical and geological analysis that would allow justified upscaling of the formations considering all initially logged geological units, and (2) the original magnetic data that, on intrusion scale, shows clear anomalies at only the intrusion and the central dunite. Since the central dunite would be discarded during the inversion due to its remanence, this left UPX as the only formation with strong magnetic properties. Hence, the relevance of the other formations was considered minimal and grouping them under the umbrella term "host rock" was deemed justified.

In retrospect, we can conclude that the geological model was too simplistic. It was not possible to find a representative susceptibility value for the surrounding of the intrusion and a mismatch was expected for observations outside the intrusion. To enhance the model, a minimum requirement would be the inclusion of the gabbroic unit in the geological model. Not only because the gabbroic formation is assumed to be part of the intrusive history of UPX (Section 2.2), but also because the intrusive body is overlain by a thick gabbroic layer in the Southwest. If we want to capture the structures underneath this gabbroic layer using geophysical likelihoods, the gabbroic rock has to be considered too, as it has significantly different rock properties.

Additionally, magnetite gabbro in the gabbroic unit could have added to the mismatch of observed and simulated values, since magnetite gabbro has stronger magnetic properties than the rest of the surrounding. The same holds for the host rock to the North of the intrusion, which shows alternations of volcanic rocks and black shales, which have different petrophysical properties.

Another important addition to the geological model would be differentiation within the intrusive body itself and account for the different rock properties between the ore body and the non-mineralised parts of the UPX unit. This would mean an extension to a heterogeneous inversion. This is certainly relevant when inverting for rock properties, but also of importance for retrieving structural knowledge through geophysical data since geophysical methods reflect rock property contrasts.

Apart from the upscaling in order to build the geological models, additional uncertainties are added to the model by the limited knowledge of the obtained geological data. There is no knowledge regarding the core logging, on which the borehole-based geological model was fully based. Inconsistency in logging is assumed to impose significant uncertainty on the data. Uncertainty in the cross-section based geological model was already evident when the selected points on all 4 cross-sections could not be interpolated into a 3D model that resembles the cross-sections. Whether this was due to inconsistency of the 2-dimensionally drawn cross-sections in 3-dimensional space, or whether it was an artifact of the software, remains unclear.

6.2. FORWARD MODELLING

Considering the assumptions made in the implementation of the forward magnetic calculation function (Section 4.2.3), and adapting it to our study case, we can state the following:

1. We assign homogeneous susceptibility values per lithological unit, which is not assumed to be a valid approximation of the reality in this case. By defining it later on as a stochastic variable, we try to correct for the effectively inhomogeneous spatial distribution of the magnetic properties.

2. As mentioned in Section 4.1.1, it is known that there is remanent magnetisation. However, there is no clear consensus on the orientation of the remanence. Therefore it cannot be included in the forward model. Note that, if there were orientation measurements, it could be included in the forward model using Equation 3.7.

3. As shown in Figure 4.3, the intensity of the anomalous field is indeed small compared to the regional field (the DC offset).

Assumptions (1) and (2) in the forward modelling do not hold in this case study. In order to take (1) into account by allowing for random sampling within a known susceptibility distribution, a reasonable distribution has to be known. Considering the mismatch in magnetic field intensities between our initial forward calculated fields (Figure 5.3e, d) and the observed data (Figure 5.1), we can conclude that our initial (measured) estimate of k_{UPX} could not describe the data.
An appropriate distribution could be assigned to it. Scaling the susceptibility values by fitting the forward predictive model to the data was, of course, a very rough estimate. After obtaining more knowledge about the probabilistic system, it is decided that a more accurate, less biased and hence better justifiable result would be obtained by inverting for the susceptibilities. This is done through a completely uninformative prior distribution and very informative likelihoods, rather than directly combining it within a more complex probabilistic model.
The obtained value of $k_{UPX} = 0.12$ is verified with commercial software by forward modelling, where a value of 0.11 was obtained for the intrusive anomaly. This has a mismatch of an order of magnitude with the borehole measured data. A study by Adams and Dentith (2017) provides an explanation for this. Their comparison of handheld magnetic susceptibility data and natural remanent magnetisation data, shows that rocks dominated by remanence may have magnetisation values underreported by two orders of magnitude. Hence, exclusive use of measured susceptibility data is questionable (Adams and Dentith, 2017) and using the susceptibility value found through inversion is justified.

The inversion results for k_{host} were rather inconclusive since we only obtained a changing posterior distribution after adjusting the probabilistic set-up accordingly. The original probabilistic set-up with normal distributions and a deterministic σ for the observations was very conclusive

for k_{UPX}, hence it is not expected that inversion was performed poorly. Different paramerisations have been tested and the most conclusive result gave $\mu_{kUPX} = 0.0030$ (from a wide, lognormal-like distributed posterior (Figure 5.8b)), which is close to the values obtained from borehole data $\mu_{k_{host}} = 0.0038$ (Figure 5.2). These values suggest paramagnetic properties and are likely caused by the issues addressed in the previous section.
Ideally, we would want to define k_{host} as a stochastic variable to the inference, but considering our poor understanding of its distribution it was decided not to do so. Taking additionally into account that every stochastic parameter adds computation time, it was decided to keep k_{host} as a deterministic variable. This is justified by considering (1) the small magnetic effect of the host rock relative to UPX due to the two-order-of-magnitude larger k_{UPX}, (2) the aim of our study to focus on the UPX formation, and (3) the defined likelihood functions, with the selected magnetic observation being mainly in the vicinity of in the intrusion.

Besides the discussed spatial variability of magnetic properties, the magnetic method is also sensitive to temporal variations. On a short timescale, temporal uncertainty includes diurnal variations, which should be corrected for. On a longer timescale, the magnetic history combined with the magnetic properties of a rock poses the issue of remanent magnetisation. Additionally, the regional field poses uncertainty in the forward simulations. In the Kevitsa intrusive region, the magnetic responses of the subsurface are overall strong and due to large anomalies, it is hard to recognise a regional trend. A DC offset is considered reasonable in this case, but evidently, there are better ways to approximate it. Li and Oldenburg (1998) summarised different methods and provided an elegant inversion-based method. Lastly, the inducing field during surveying has to be known in order to have a chance to generate the same data through forward calculations. In this project, the IGRF value at the month of the survey, at the survey location, is used as this was deemed to be the best option.

All in all, the magnetic method contains a lot of variables that are hard to capture with both the geological model and the probabilistic model used in this project. The sensitivity of the method results in an infinite number of parameters that control the magnetic response measured during a given survey. Using less-sensitive geophysical methods in inversion could provide a solution to some of these problems. When limited to potential fields, gravity data would already be easier to implement as it contains less small-scale variations and is less sensitive to external factors (e.g. solar storms).

6.3. INVERSE MODELLING

Bayesian inference requires a good understanding of the model parameters, the used data and the mathematical functions that link the two (Betancourt, 2018). Due to the holistic approach adopted in this project, we obtain a good understanding of these aspects:

- By building the initial geological model, both the geological setting is studied and intuition is created for the automatic geological modelling creation step.
- An understanding of the used data is gained by processing it before including the data in the inverse framework.
- By implementing the magnetic forward calculator based on a 3D voxelised space, the relation between the input parameters and the resulting forward simulations is known. This is directly related to the likelihood functions that have a crucial role in the inference.

By first testing the methodology on synthetic data with a known solution, we conclude that the

forward magnetic calculations fit the analytical solution within the desired range of accuracy. The proposed inverse methodology by means of magnetic likelihood function, as tested on the sphere, shows that the result of the inverse modelling is highly dependent on the definition of the probabilistic model. The difference between assigning informative and non-informative prior distributions is shown by the synthetic test, where the informative depth distribution $p(z)$ provided a much better estimate of the posterior distribution compared to the weakly informative $p(k)$ of the susceptibility (Figure 4.8). An additional expected, but important, observation was the strong correlation between the spatial parameter z and the susceptibility k.

These observations from the synthetic test could directly be linked to the inversion results on the real data, shown in Section 5.3. By starting with a simple probabilistic model (using a simple geological model), the complexity of the inference could be increased by expanding the probabilistic model using gained knowledge from the previous results. Working in such an iterative manner allows for easier localisation of problems or unwanted results, and eventually leads to a better set-up of the final inversion together with an increased understanding of the results.

In the iterative inversion process, inverting for the susceptibilities was a crucial step. The obtained posterior distribution for k_{UPX} served as a highly informative prior distribution for the following tests. From the synthetic data test, the importance of defining either good priors or proper likelihoods (though preferably both), was shown. Since our geological model is very simplified, the likelihood functions are not very strictly defined. Because the inference was mostly constrained by likelihoods based on magnetic measurements, which are directly controlled by the susceptibilities, a uninformative prior distribution in a joint inversion would have a significant effect on the sampling efficiency and the inversion result. Joint inversion for all x, y, z-coordinates as well as k, is a high-dimensional problem and a weakly informative prior would span large volumes. Due to the strong influence of k through the likelihood function, defining k well, already narrows down the prior space and hopefully allows for a sampling starting point close to the target distribution. This effect was already clear in the synthetic joint inversion for k and z (Figure 4.8). Though the Bayesian inference is aimed to combine everything in one probabilistic model, it has been chosen to invert for the petrophysical properties separate from the spatial uncertainties, in order to get a good estimate of k before adding it to the joint inference.

The quality of the geological model obtained through the proposed methodology is dependent on and limited to the decisions we make, such as the chosen stochastic variables and the data that we use for inverting. It is not trivial to encapsulate unidentified uncertainties by means of distributions. Considering the earlier-mentioned uncertainties in the geological data for example, without knowing the uncertainty of the data, we pose a large subjectivity to the result by estimating it.
Additionally, each type of data contains different information and has different information quality. Potential-field methods are, as mentioned before, inherently non-unique as a consequence of the underlying physics. This cannot be avoided, regardless of data volume and quality. In the general case, the majority of the inverse problems are already non-unique regardless of governing physical laws. This can result from having more model parameters than observation points, in which case the model parameters might not be fully constrained since there might not be enough equations in the mathematical model that link the parameters to the observations. This can be caused by either a lack of data or a lack of computational sources. Our last probabilistic model contained 67 stochastic model parameters and 15 observations. This set-up was not due to a lack of data, but rather due to the computational cost of computing the forward solution for each added observation through the likelihood function. With the current set-up of GemPy, geophys-

ical likelihoods are heavier to evaluate than geological likelihoods as used in this project. Therefore, adding more geological likelihoods could provide a solution to including more constraints without increasing the computational time too much.

It is shown that adding more constraints, does not necessarily decrease the uncertainty in the model (e.g. considering the overall uncertainty in Figure 5.12 compared to Figure 5.10). However, it does help to remove unrealistic realisations that our weak prior model could not suppress. The increase in uncertainty could be due to a lack of prior knowledge in combination with a poorly-defined likelihood, incompatibility between priors and likelihoods or imposing observations with poor data quality. We can overcome the latter by considering which data will add the most information to the model. This, of course, is dependent of what we want to gain from the inversion. Yet, adding non-unique potential field data to an already non-unique inverse problem is not considered to be the best option when other data is available. Certainly not when we are interested in geological structures rather than petrophysical properties since the non-uniqueness of potential fields is exactly due to the physical inability to distinguish between different geometries at different depths. More meaningful geophysical constraints could be imposed by using e.g. seismic data. This would also be better for constraining the model parameters at larger depths since acoustic waves in the subsurface generally suffer less dramatically from decreasing field strength than magnetic fields.

Lastly, a balance has to be found between geological reality and fitting the data. The computed MAP in the last inversion shows a good example of this. The MAP is the model that maximizes the joint posterior probability density. Due to the high correlation between k and the spatial parameters, combined with the dominant contribution of k through the magnetic likelihood functions, we obtain a solution that statistically fits best because the susceptibility fits the data well. The MAP, in this case, does not tell us much about the weaker spatial parameters, which were the main focus of our study. This could additionally be due to an already reasonable initial geological model. However, the result of the MAP model, in general, shows that a statistical fit does not necessarily give a result that represents the actual geology. Following Occam's razor, we should aim to keep the model as simple as possible while trying to fit the data as well as possible, rather than adjusting the model to fit the data.

7

CONCLUSION

The solution of the probabilistic inverse problem presents an ensemble of models that fit the data, enabling us to consider both model uncertainty and knowledge integration in one framework. Information entropy provides a quantitative analysis of the uncertainty in the results and has proven its advantage over regular visual analysis of the realised models by capturing uncertainties that visual analysis could not capture. Though powerful in uncertainty quantification, the tested methodology does not provide a trivial way for validation of the result by means of analysing one single optimised geological model. The result of probabilistic inversion is provided in statistical distributions, and finding one representative model in a high-dimensional problem is more complex than just taking the mode of the distribution (MAP).

However, we showcase here that the strength of Bayesian inference is mainly to combine observation from different sources and analyse uncertainties in the model. It can be concluded that through the definition of meaningful likelihood functions, uncertainties in the geological model can be reduced.

The general findings can be summarised as follows: (1) Building a probabilistic framework requires a good understanding of the problem to solve, the available data and the mathematical equations that can link the two. (2) The initial geological model should contain enough complexity to be able to describe the data. (3) the used data ideally should be robust and chosen depending on what we want to learn from the inversion. And (4) by adding different types of data through likelihoods we can combine strengths from different sources.

The general conclusions can be specified towards the Kevitsa case study by stating that: (1) The geological setting, as well as the acquisition and interpretation of the data, should be well understood. (2) The data needs to be processed to represent the scale of the geological model. (3) Magnetic data is not the desired geophysical method to invert for structural properties of the subsurface. And (4) by using geological data where magnetic data cannot provide information, we can reduce the uncertainty in our model.

The results are promising, and by implementing more likelihood functions, one could obtain a good estimate of the geological structure of the Kevitsa intrusion, while quantifying the uncertainty in this estimate.

BIBLIOGRAPHY

(n.d.). National oceanic and atmospheric administration (noaa). https://www.ngdc.noaa.gov/geomag/calculators/magcalc.shtml#igrfwmm. Accessed: 2019-12-06.

Adams, C. and Dentith, M. (2017). Magnetic measurements on diamond drill core: Are we really measuring magnetic susceptibility? *Proceedings of Exploration 17: Sixth Decennial International Conference on Mineral Exploration*, 52:725–728.

Bayes, T. (1763). An essay toward solving a problem in the doctrine of chances. *Philosophical Transactions of the Royal Society of London*, 53:370–418. Communicated by R. Price, in a letter to J. Canton.

Bellman, R. (1957). *Dynamic Programming*. Princeton University Press, Princeton, NJ, USA, 1 edition.

Betancourt, M. (2018). A Conceptual Introduction to Hamiltonian Monte Carlo. *arXiv:1701.02434 [stat]*. arXiv: 1701.02434.

Betancourt, M. J., Byrne, S., Livingstone, S., and Girolami, M. (2014). The Geometric Foundations of Hamiltonian Monte Carlo. *arXiv:1410.5110 [stat]*. arXiv: 1410.5110.

Blakely, R. J. (1995). *Potential theory in gravity and magnetic applications*. Cambridge University Press, Cambridge [England] ; New York.

Bokeh Development Team (2019). *Bokeh: Python library for interactive visualization*.

Davidson-Pilon, C. (2015). *Bayesian Methods for Hackers: Probabilistic Programming and Bayesian Inference*. Addison-Wesley Professional, 1st edition.

de la Varga, M., Schaaf, A., and Wellmann, F. (2019). GemPy 1.0: open-source stochastic geological modeling and inversion. *Geoscientific Model Development*, 12(1):1–32.

de la Varga, M. and Wellmann, J. F. (2016). Structural geologic modeling as an inference problem: A Bayesian perspective. *Interpretation*, 4(3):SM1–SM16.

Fichtner, A. (2018). Fundamentals of inverse theory.

Fournier, D. (2019). *Advanced potential field data inversion with l_p-norm regularization*. PhD thesis, University of British Columbia.

Gelman, A., Carlin, J. B., Stern, H. S., and Rubin, D. B. (2013). *Bayesian Data Analysis*. Chapman and Hall/CRC, 3rd ed. edition.

Gregory, J., N. J. G. W. and Lappalainen, M. (2016). Kevitsa nickel copper mine, lapland, finland. Technical report, First Quantum Minerals Ltd.

Hanski, E., Huhma, H., Rastas, P., and Kamenetsky, V. S. (2001). The Palaeoproterozoic Komatiite–Picrite Association of Finnish Lapland. *Journal of Petrology*, 42(5):855–876.

Hinze, W. J. (2012). The Role of Gravity and Magnetic Methods in Engineering and Environmental Studies. In *Geotechnical and Environmental Geophysics: Volume I, Review and Tutorial*, pages 75–126.

Hinze, W. J., von Frese, R. R. B., and Saad, A. H. (2013). *Gravity and Magnetic Exploration: Principles, Practices, and Applications*. Cambridge University Press.

Homan, M. D. and Gelman, A. (2014). The no-u-turn sampler: Adaptively setting path lengths in hamiltonian monte carlo. *J. Mach. Learn. Res.*, 15(1):1593–1623.

Hölttä, P., Väisänen, M., Väänänen, J., and Manninen, T. (2007). Paleoproterozoic metamorphism and deformation in central lapland, finland. page 50.

Kaufman, A. A., Hansen, R. O., and Kleinberg, R. L. K. (2008). Principles of the magnetic methods in geophysics. volume 42 of *Methods in Geochemistry and Geophysics*, page iii. Elsevier.

Kellogg, O. D. (1953). *Foundations of potential theory*. Springer.

Koivisto, E., Malehmir, A., Hellqvist, N., Voipio, T., and Wijns, C. (2015). Building a 3d model of lithological contacts and near-mine structures in the Kevitsa mining and exploration site, Northern Finland: constraints from 2d and 3d reflection seismic data: Kevitsa 3d geological model. *Geophysical Prospecting*, 63(4):754–773.

Kokko, S.-M. (2018). Boliden summary report: Resources and reserves 2018, kevitsa. Technical report, New Boliden.

Lajaunie, C., Courrioux, G., and Manuel, L. (1997). Foliation fields and 3D cartography in geology: Principles of a method based on potential interpolation. *Mathematical Geology*, 29(4):571–584.

Langel, R. A. and Hinze, W. J. (1998). *The Magnetic Field of the Earth's Lithosphere: The Satellite Perspective*. Cambridge University Press. Google-Books-ID: S3SCwnO707oC.

Le Vaillant, M., Hill, J., and Barnes, S. J. (2017). Simplifying drill-hole domains for 3D geochemical modelling: An example from the Kevitsa Ni-Cu-(PGE) deposit | Elsevier Enhanced Reader. *Ore Geology Reviews*.

Lelièvre, P. G. and Oldenburg, D. W. (2006). Magnetic forward modelling and inversion for high susceptibility. *Geophysical Journal International*, 166(1):76–90.

Li, Y. and Oldenburg, D. W. (1998). Separation of regional and residual magnetic field data. *GEOPHYSICS*, 63(2):431–439.

Lowrie, W. (2007). *Fundamentals of Geophysics*. Cambridge University Press, 2 edition.

Luolavirta, K., Hanski, E., Maier, W., and Santaguida, F. (2018). Whole-rock and mineral compositional constraints on the magmatic evolution of the Ni-Cu-(PGE) sulfide ore-bearing Kevitsa intrusion, northern Finland.

Metropolis, N. and Ulam, S. (1949). The monte carlo method. *J. Am. Stat. Assoc.*, 44:335.

Montonen, M. (2012). Induced and remanent magnetization in two boreholes of the kevitsa intrusion. Master's thesis, University of Helsinki.

Mutanen, T. (1997). *Geology and Ore Petrology of the Akanvaara and Koitelainen Mafic Layered Intrusions and the Keivitsa-Satovaara Layered Complex, Northern Finland*. Bulletin (Geologian tutkimuskeskus (Finland))). Geological Survey of Finland.

Neal, R. M. (2012). MCMC using Hamiltonian dynamics. *arXiv:1206.1901 [physics, stat]*. arXiv: 1206.1901.

Newton, I. (1687). *The Principia: mathematical principles of natural philosophy*. Translated by Cohen, B and Whitman, A. University of California Press.

Plouff, D. (1976). Gravity and magnetic fields of polygonal prisms and application to magnetic terrain corrections. *Geophysics*, 41(4):727–741.

Salvatier, J., Wiecki, T., and Fonnesbeck, C. (2015). Probabilistic Programming in Python using PyMC. *arXiv:1507.08050 [stat]*. arXiv: 1507.08050.

Sambridge, M. and Mosegaard, K. (2002). Monte carlo methods in geophysical inverse problems. *Reviews of Geophysics*, 40(3):3–1–3–29.

Shannon, C. E. (1948). A Mathematical Theory of Communication. page 55.

Smith, W. H. F. and Wessel, P. (1990). Gridding with continuous curvature splines in tension. *Geophysics*, 55(3):293–305.

Talwani, M. (1965). Computation with the help of a digital computer of magnetic anomalies caused by bodies of arbitrary shape. *Geophysics*, 30(5):797–817.

Tarantola, A. (2005). *Inverse Problem Theory and Methods for Model Parameter Estimation*. Society for Industrial and Applied Mathematics.

Telford, W. M., Telford, W., Geldart, L., Sheriff, R. E., and Sheriff, R. E. (1990). *Applied geophysics*, volume 1. Cambridge university press.

Wellmann, J. F., de la Varga, M., Murdie, R. E., Gessner, K., and Jessell, M. (2018). Uncertainty estimation for a geological model of the Sandstone greenstone belt, Western Australia – insights from integrated geological and geophysical inversion in a Bayesian inference framework. *Geological Society, London, Special Publications*, 453(1):41–56.

Wellmann, J. F. and Regenauer-Lieb, K. (2012). Uncertainties have a meaning: Information entropy as a quality measure for 3-D geological models. *Tectonophysics*, 526-529:207–216.

A

FIGURES

A.1. GEOLOGICAL DATA

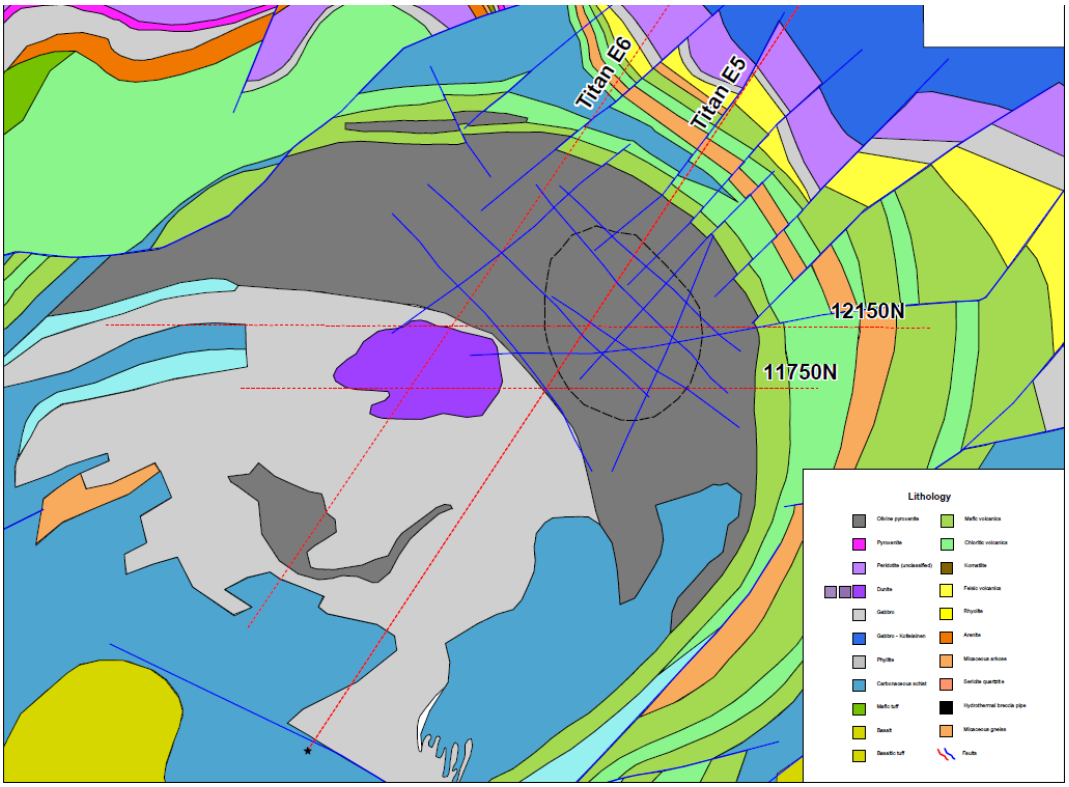

Figure A.1: Original geological model that corresponds to the cross-section on which the geological model is based.

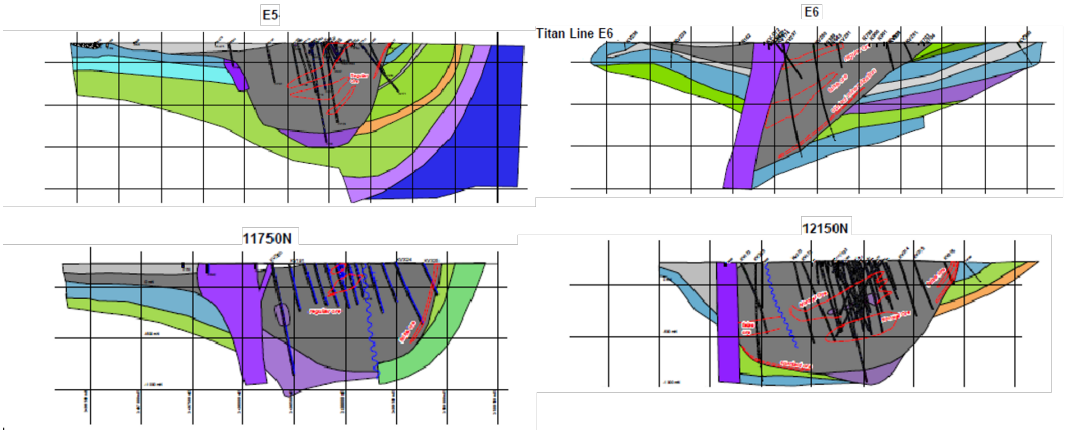

Figure A.2: Original cross-sections on which the geological model is based. Points have been selected from these sections using interactive plotting tool Bokeh Development Team (2019). The correctness of the obtained coordinates is verified by looking up the coordinates of some of the boreholes that are included in the cross-sections.

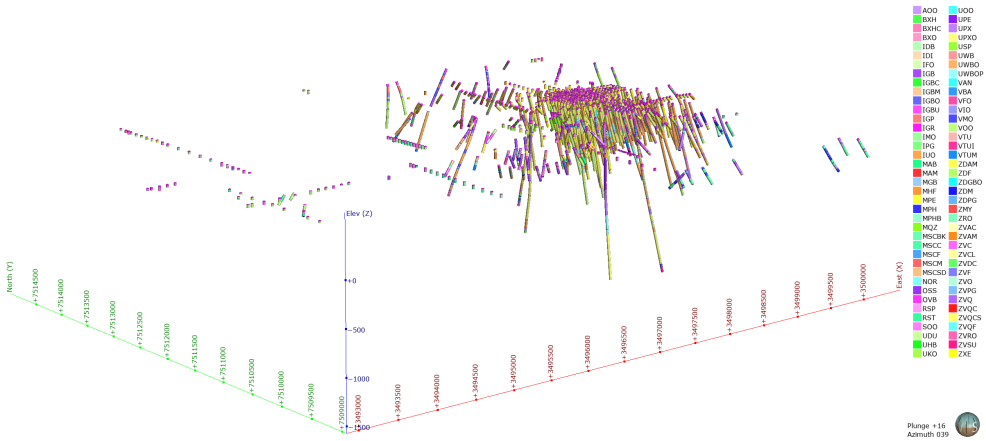

Figure A.3: All available borehole data from the Kevitsa region,

A.2. RESULTS

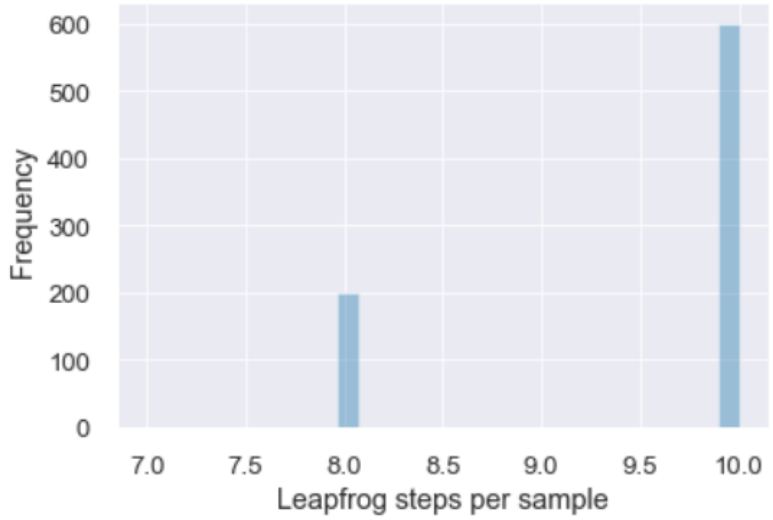

Figure A.4: The number of leapfrog steps taken sample throughout the sampling process in inversion I. In a converged chain, one would expect large numbers before convergence, lower numbers later on. In this case, the maximum number of steps (10) was obtained very often, especially later on in the chain. This can be interpreted as the chain getting stuck in a region, and hence poor exploration of the model space.

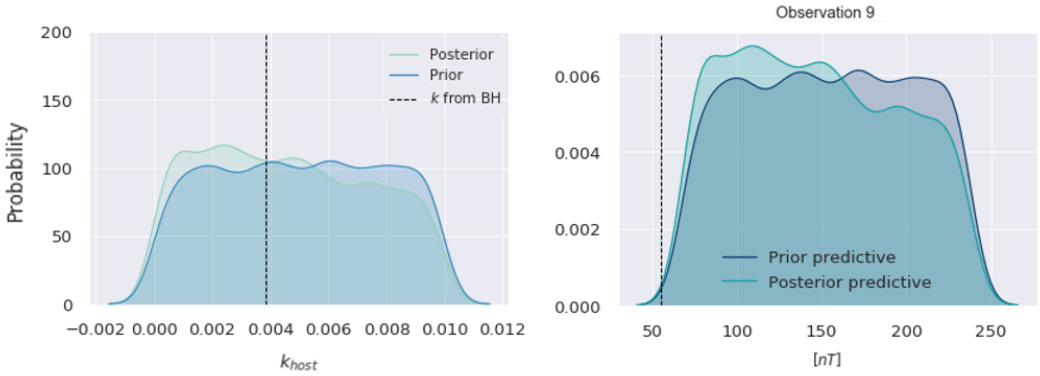

Figure A.5: Inversion II: Intermediate result for the susceptibility of the host rock k_{host}. The prior and posterior distributions for k_{host} (left) and the posterior check for the magnetic response at observation point 9 (Figure 5.9) (right) are presented. Observation 9 is used as likelihood function by assigning a normal distribution to the observed value, the the mean being the forward calculated model, and $\sigma = 100nT$. k_{host} was assigned an uniform prior distribution. It can be seen that posterior $p(k_{host}|y_9)$ is very weakly informative and strongly resembles the prior $p(k_{host})$. The predictive distributions are not strong enough to have an influence, as both the prior and posterior predictive resemble $p(k_{host})$ and $p(k_{host}|y_9)$ respectively.

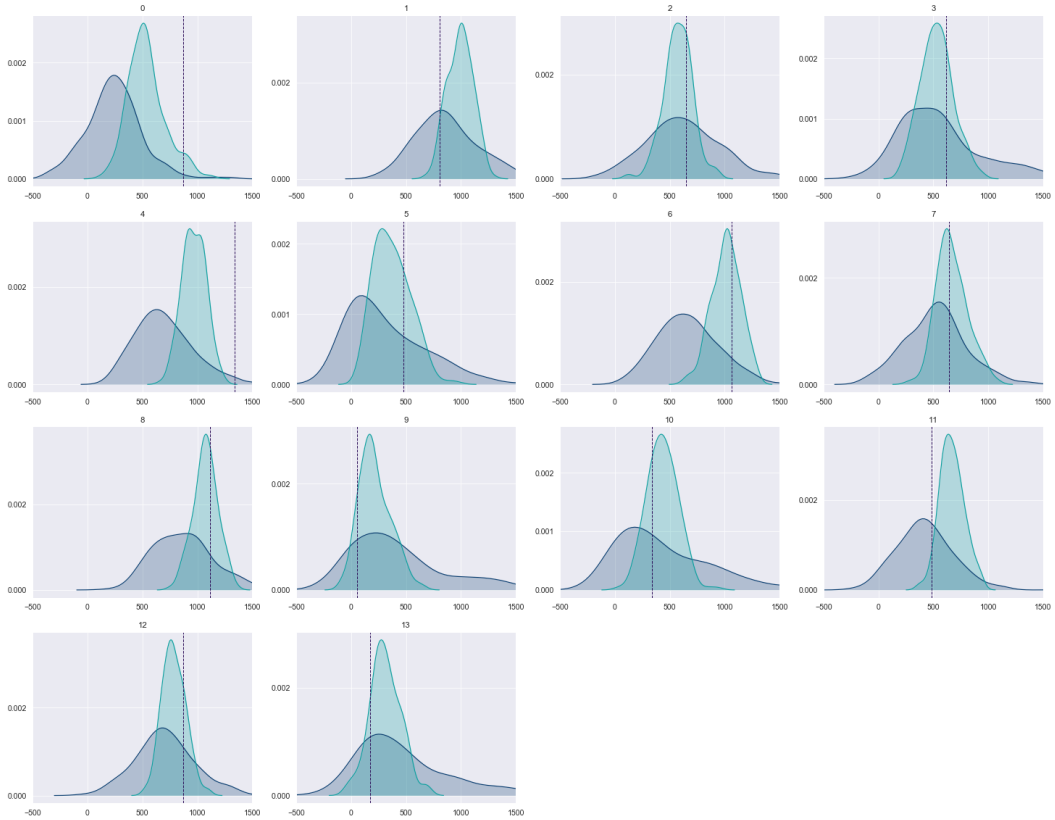

Figure A.6: Inversion III: Posterior predictive checks for all observation locations in the geophysical likelihood function $p(z|y_0,...,y_{14})$. The dark shades represent the prior predictive, the lighter shades the posterior predictive and the dashed lines the measured magnetic intensity at the location.

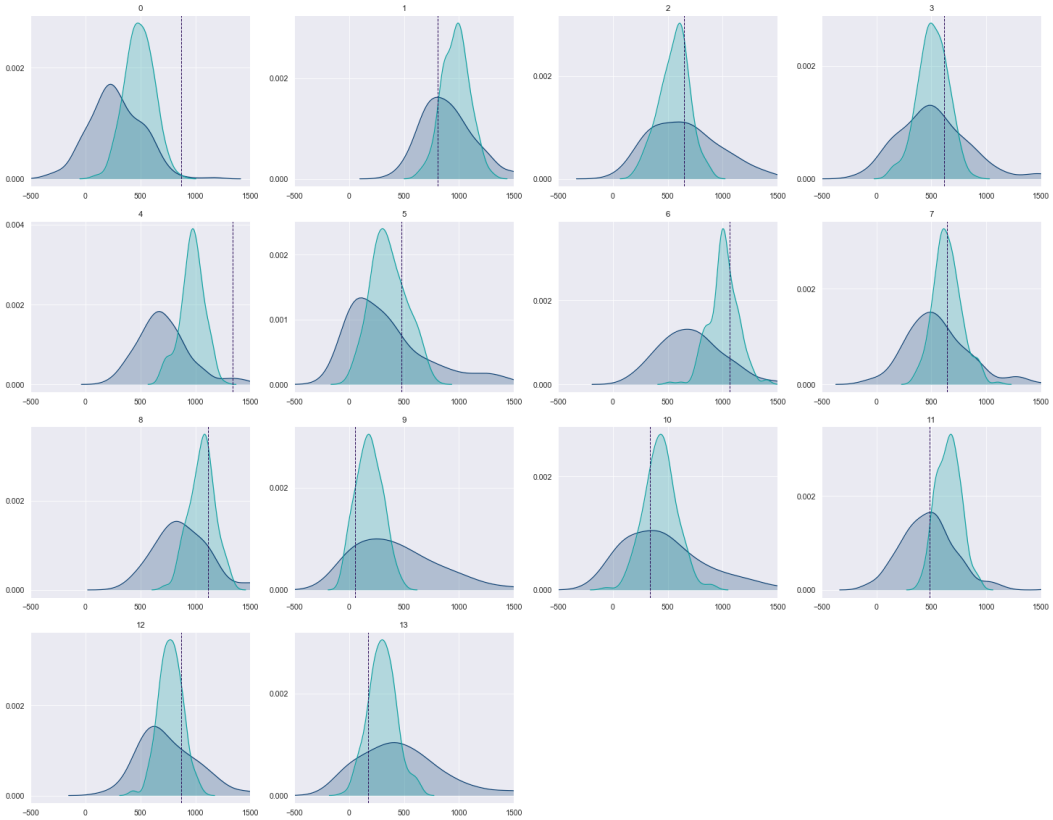

Figure A.7: Inversion IV: Posterior predictive checks for all observation locations in the geophysical likelihood function. The dark shades represent the prior predictive, the lighter shades the posterior predictive and the dashed lines the measured magnetic intensity at the location. The same parameterisation as inversion III is used. It can be seen that the same result is obtained as inversion III and that the geological likelihood had no influence on the result.

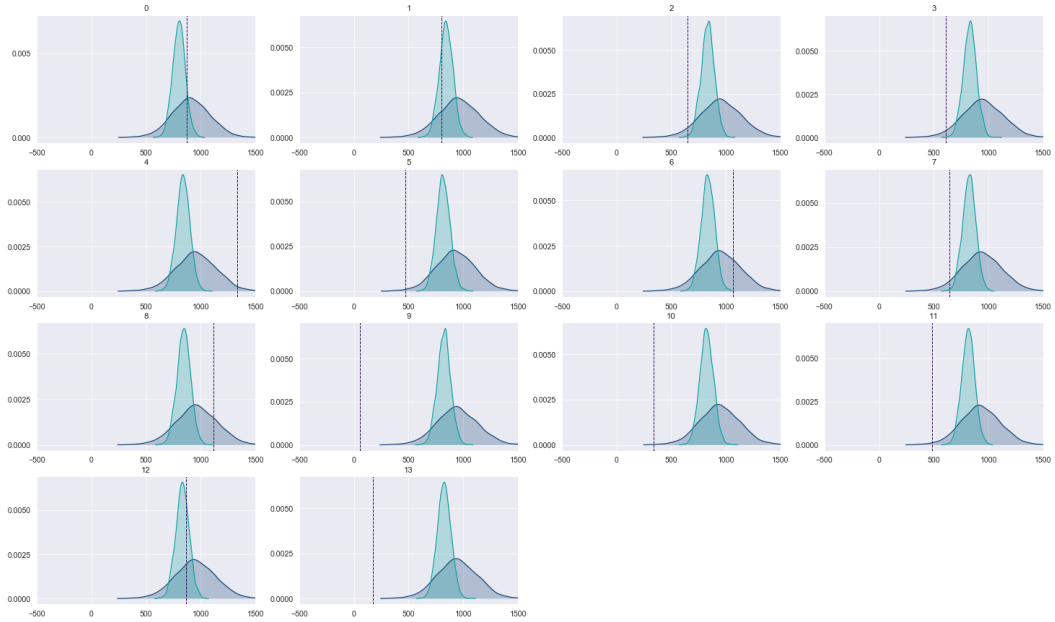

Figure A.8: Inversion IV with increased uncertainty assigned to selected observations and k_{UPX}: Posterior predictive checks for all observation locations in the geophysical likelihood function. The dark shades represent the prior predictive, the lighter shades the posterior predictive and the dashed lines the measured magnetic intensity at the location. The difference to the discussed set-up of inversion IV (and the posterior predictive check-in Figure A.7) is that this inversion was performed with an increased σ for some observation location, where in the previous results the measured values were either in the tails or outside of the prior predictive distribution. Additionally the uncertainty on k_{UXP} was slightly increased from $\sigma = 0.2$ to $\sigma = 0.26$ and 3000 samples were taken, against 800 in previous tests. The results are significantly different (besides their smoothness due to increased sampling), most likely due to changes in parameterisation of the strongly dominant k_{UPX} and its interaction with the redefined uncertainty in the observations.

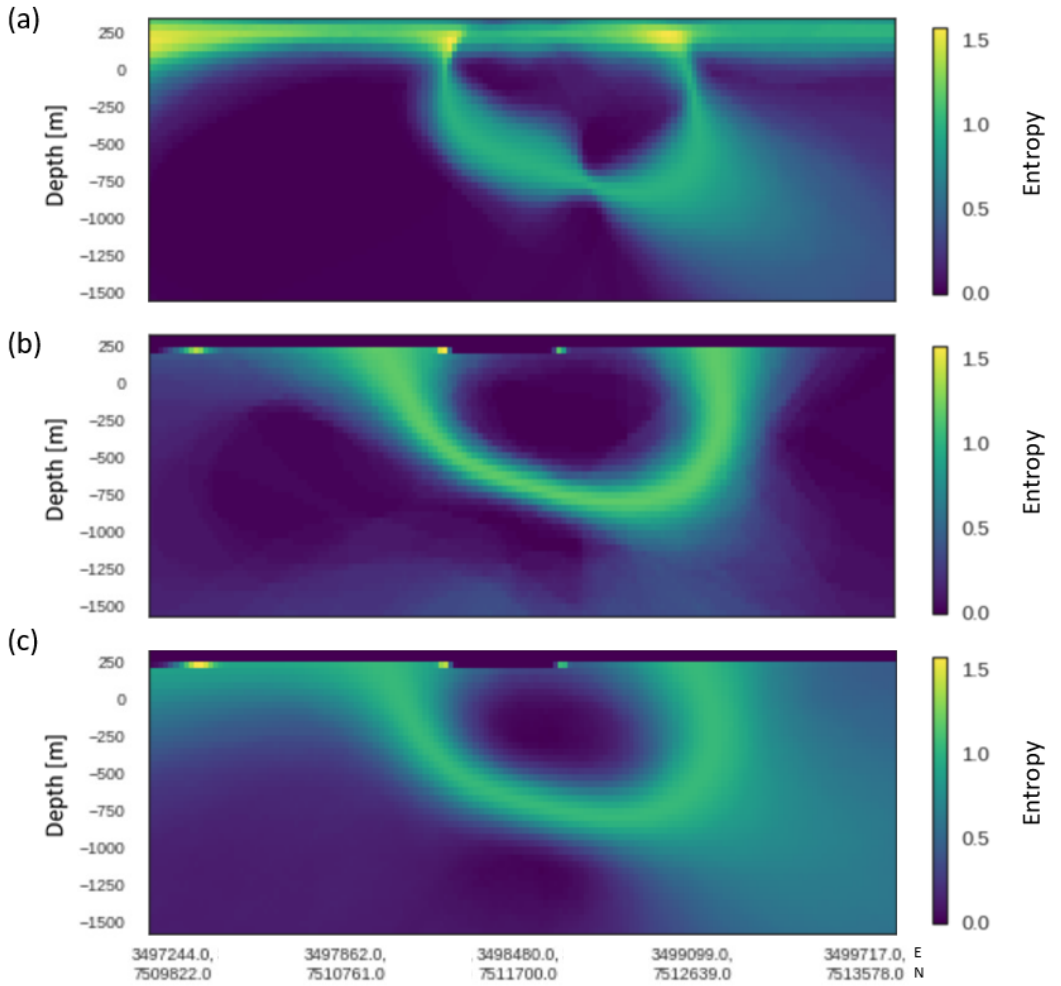

Figure A.9: Entropy plot on cross-section E5, which corresponds to seismic section 2.2. (a), (b) and (c) correspond to inversion I, III and IV respectively. It shows the same trends as the example section: artifacts at the bottom of (b) are removed after adding a geological constrain. The uncertainty in this part overall decreased considerably, compared to the rest of the section, where the overall uncertainty increased. Additionally, we see that there is high uncertainty toward the North-West (right side), where the which is likely due to the poorly defined k_{host} in combination with the shallow dip of the intrusion here.

B

CODES

Figure B.1: Function to upward continue the magnetic data as explain in Section 4.1.1. (After Blakely (1995))

```
[ ]: def uc(grid_x, grid_y, data, dz):
        """
        Args:
            grid_x, grid_y : Grid points in x and y direction of the regularly␣
    ↪gridded data
            data           : Potential field data on regular, rectangular grid
            dz             : Continuation distance in same units as x and y, i.e.␣
    ↪the level we will continue to

        Output:
            kx, ky, kz     : Wavenumbers in x, y, and z direction
        """

        grid = np.size(grid_x[:,0]), np.size(grid_y[0,:])

        # Expand grid:
        #Find next power of two to extend the grid to
        gridx = 1 << int.bit_length(int(grid[0]))
        gridy = 1 << int.bit_length(int(grid[1]))

        padx = (gridx-int(grid[0]))//2
        pady = (gridy-int(grid[1]))//2

        # Pad with edge values
        padgrid = np.pad(data.reshape(grid), ((padx,), (pady,)), mode = 'edge')

        # Fourier transform data
        dx = (grid_x[:,0].max()-grid_x[:,0].min())/(grid[0]-1)
        fx = 2*np.pi*np.fft.fftfreq(padgrid.shape[0], dx)

        dy = (grid_y[0,:].max()-grid_y[0,:].min())/(grid[1]-1)
        fy = 2*np.pi*np.fft.fftfreq(padgrid.shape[1], dy)

        # Wavenumbers kx, ky, kz
        kx, ky = np.meshgrid(fy, fx)[::-1]
        kz = np.sqrt(kx**2 + ky**2)

        # Upward continue using Equation 4.1
        uc_ft = np.fft.fft2(padgrid)*np.exp(dz*kz)
        uc = np.real(np.fft.ifft2(uc_ft))

        # Crop data back to original grid
        uc_data = uc[padx: padx + grid[0], pady : pady + grid[1]]

        return uc_data
```

The written codes for the forward magnetic calculation as explain in Section 4.2.3 are presented here. I have written the code in NumPy and decomposed it into a constant part (corresponding to Equation 4.9) and a variable part (corresponding to Equations 4.7, 4.10 and 4.11). The variable part is later included in the Theano core of GemPy, allowing faster computation and inclusion into the probabilistic framework.

Figure B.2: Function to compute the directional cosines needed for the magnetic forward calculations. (After Blakely (1995))

[11]:
```
def direction(incl, decl):
    """
    Args:
        incl: Inclination as positive from horizontal [deg]
        decl: Declination as positive to East from Geopgraphic North [deg]

    Returns:  Directional cosines
    """

    incl_rad = np.deg2rad(incl)
    decl_rad = np.deg2rad(decl)
    x = np.cos(incl_rad)*np.cos(decl_rad)
    y = np.cos(incl_rad)*np.sin(decl_rad)
    z = np.sin(incl_rad)
    return (x, y, z)
```

Figure B.3: Function to compute the volume integrals from Equation 4.9, as solved by Plouff (1976). This is the constant part of the forward magnetic calculation.

[12]:
```
def set_Vs(kernel_centers, kernel_dxyz_left, kernel_dxyz_right):
    """
    Calculates volume integrals for each voxel. This will be constant for all␣
↪devices in GemPy.

    Args: Grid properties, i.e. output from g.create_irregular_grid_kernel()

    Returns: array with all six volume integrals.
    """

    grid_values = kernel_centers
    s_gr_x = grid_values[:, 0]
    s_gr_y = grid_values[:, 1]
    s_gr_z = -1*grid_values[:, 2] # Talwani takes x-axis positive downwards, and␣
↪gempy negative downwards

    # Coordinates of each corner of a voxel
    x_cor = np.stack((s_gr_x - kernel_dxyz_left[:, 0], s_gr_x +␣
↪kernel_dxyz_right[:, 0]), axis=1)
    y_cor = np.stack((s_gr_y - kernel_dxyz_left[:, 1], s_gr_y +␣
↪kernel_dxyz_right[:, 1]), axis=1)
    z_cor = np.stack((s_gr_z + kernel_dxyz_left[:, 2], s_gr_z -␣
↪kernel_dxyz_right[:, 2]), axis=1)
    # ...and prepare them for a vectorial op
    x_matrix = np.repeat(x_cor, 4, axis=1)
    y_matrix = np.tile(np.repeat(y_cor, 2, axis=1), (1, 2))
    z_matrix = np.tile(z_cor, (1, 4))

    R = np.sqrt(x_matrix**2 + y_matrix**2 + z_matrix**2) #distance to each corner
    s = np.array([-1, 1, 1, -1, 1, -1, -1, 1]) #gives the sign of each corner:␣
↪depends on your coordinate system

    #variables V1-6 represent integrals of volume for each voxel
    V1 = np.sum(-1*s*np.arctan2((y_matrix*z_matrix), (x_matrix*R)),axis=1)
    V2 = np.sum(s*np.log(R+z_matrix), axis=1)
    V3 = np.sum(s*np.log(R+y_matrix), axis=1)
    V4 = np.sum(-1*s*np.arctan2((x_matrix*z_matrix), (y_matrix*R)), axis=1)
    V5 = np.sum(s*np.log(R+x_matrix), axis=1)
    V6 = np.sum(-1*s*np.arctan2((x_matrix*y_matrix), (z_matrix*R)), axis=1)

    #contains all the volume integrals (6 x n_kernelvalues)
    V = np.array([V1,V2,V3,V4,V5,V6])
    return V
```

Figure B.4: Function to find the calculate the anomalous magnetic field intensity. This is the variable part of the forward magnetic calculations, corresponding to Equations 4.7, 4.10 and 4.11. (After Talwani (1965)).

[13]:
```
def find_T(B_ext, incl, decl, V, k_vals):
    """
    Args:
     B_ext : External magnetic field in [T], in magnetic surveys this is the␣
↪geomagnetic field - varies temporaly
     incl  : Dip of the inducing field, positive from horizontal [deg]- varies␣
↪spatially
     decl  : Angle between magnetic and geographic North, positive towards East␣
↪[deg] - varies spatially
     V     : Solutions to volume integrals - constant per observation point
     k_vals: Susceptibility values per voxel [-] - varies per observation point

    Returns:
     dT        : Total Magnetic Anomaly in the direction of the Earth's main␣
↪field in [T]

    Assumptions:
     Magnetisation is only induced (no remnant magnetisation)
     Susceptibility is isotropic
    """

    # Induced magnetisation [T]
    J = k_vals*B_ext

    # And it's components:
    dir_x, dir_y, dir_z = direction(incl,decl)
    Jx = dir_x*J
    Jy = dir_y*J
    Jz = dir_z*J

    # Repeat volume solutions for each observation point
    ndevs = len(k_vals)//V.shape[1]
    V = np.tile(V,(1,ndevs))

    # Directional magnetic effect on one voxel
    Tx = (Jx*V[0,:] + Jy*V[1,:] + Jz*V[2,:])/(4*np.pi)
    Ty = (Jx*V[1,:] + Jy*V[3,:] + Jz*V[4,:])/(4*np.pi)
    Tz = (Jx*V[2,:] + Jy*V[4,:] + Jz*V[5,:])/(4*np.pi)

    Tx = (np.sum(Tx.reshape(ndevs,-1), axis=1))
    Ty = (np.sum(Ty.reshape(ndevs,-1), axis=1))
    Tz = (np.sum(Tz.reshape(ndevs,-1), axis=1))

    # Anomalous field in the direction of the Earths main field
    dT = Tx*dir_x + Ty*dir_y + Tz*dir_z
    return dT
```